

3D VISUALIZATION AND ANALYSIS OF PATAGONIAN GLACIERS CHANGES USING EARTH OBSERVATION DATA

MASTER'S THESIS

submitted in partial fulfillment of the requirements for the degree
of

Master of Science (MSc)

**PARIS-LODRON UNIVERSITY SALZBURG
(PLUS)**

Faculty of Digital and Analytical Sciences

Department of Geoinformatics

and

PALACKÝ UNIVERSITY OLMOUC (UPOL)

Faculty of Science

Department of Geoinformatics

PLUS supervisor: Dr. Dirk Tiede, Ph.D.

UPOL supervisor: RNDr. Jan BRUS, Ph.D.

submitted by

Felipe Camacho Hurtado

Salzburg & Olomouc, May 20, 2024.

With the support of Erasmus+ programme of the European Union. This Master's Thesis has been developed in the framework of the Erasmus Mundus Joint Master Degree (EMJMD) "Copernicus Master in Digital Earth", jointly coordinated by Paris-Lodron University Salzburg, Department of Geoinformatics, Austria together with University of South Brittany, Computer Science Department, France and Palacký University Olomouc, Department of Geoinformatics, Czech Republic.

ANOTATION

Glaciers are considered fundamental natural features as they provide services like water provision, flow regulation, flood mitigation, and biodiversity conservation. Furthermore, due to their complex nature, they provide crucial insights into the ongoing climate change dynamics as they respond to temperature and precipitation variations. Even though this has promoted the increase of glaciology research in the last few years, glacierized regions, such as the Patagonian Andes, are still barely studied due to their harsh environmental conditions and the general lack of interest from international scientific communities. Specifically, the Patagonian Andes, which is an important water supplier and economic driver in South America, is still poorly known, even though it is the largest glacierized area in the region, with more than 20000 km² distributed in the Northern and Southern Patagonian Icefields. Therefore, this research aimed to explore the potential of remote sensing data and techniques, cloud computing, and 3D visualization methods to overcome the lack of studies in the Patagonian Andes and to promote public interest in these natural ecosystems. For this purpose, a Google Earth Engine web application was developed to allow the creation, visualization, and export of remote-sensing and time series products for the Patagonian region. Moreover, with this application, a time-series analysis was performed to estimate the glacier area, Land Surface Temperature, and air temperature changes for 83 Patagonian glaciers, using Landsat 8-9, Sentinel-2, and ERA5-Land Imagery for the summer periods between 2018 and 2023. In addition, a 3D web application was developed using CesiumJS to compare and visualize the outputs from the Google Earth Engine application interactively with a full 3D perspective. As a result of the time-series analysis, with 1245 summer composites and 249 time-series charts generated, an overall retreat of the glaciers and increased temperature were observed. Furthermore, the developed web applications proved to be efficient, attractive, and user-friendly for creating and visualizing glacier remote sensing products. This study is a step toward improving the glaciology knowledge of the Patagonia region by providing insight into the current Patagonian glacier status, delivering customizable open-source web applications, and promoting glaciers' public interest through 3D experiences.

KEYWORDS

Patagonian Glaciers; Time-Series Analysis; Remote Sensing; Web Applications; Cloud Computing; Google Earth Engine; CesiumJS.

Number of pages: 77

Number of attachments: 2

DECLARATION

This thesis has been composed by *Felipe Camacho Hurtado* for the Erasmus Mundus Joint Master's Degree Program in Copernicus Master in Digital Earth for the academic years 2022/2023 and 2023/2024 at the Department of Geoinformatics, Faculty of Natural Sciences, Paris Lodron University Salzburg, and Department of Geoinformatics, Faculty of Science, Palacký University Olomouc.

Hereby, I declare that this piece of work is entirely my own, the references cited have been acknowledged and the thesis has not been previously submitted to the fulfilment of the higher degree.



20.05.2024, Olomouc

Felipe Camacho Hurtado

ACKNOWLEDGEMENT

I want to thank the Copernicus Master in Digital Earth program, Palacký University Olomouc, and Paris Lodron University Salzburg for this once-in-a-lifetime opportunity. Over the last two years, I have had the opportunity to boost my knowledge, experience new cultures, and create new experiences all around Europe.

I would also like to express my gratitude to my supervisors, RNDr. Jan BRUS.Ph.D from Palacký University Olomouc and Dr. Dirk Tiede, Ph.D. from Paris Lodron University Salzburg, who guided and advised me during the development of this thesis.

This would not have been possible without the support of the most special person in the world, my love, Maria Rodriguez, who gave me strength and motivation and with whom I shared the best moments of my life for quite a long time. This experience was unique just because of you.

Of course, my parents and my brother have always been there. All that I am is thanks to their guidance and love; this achievement is yours. I could not have asked for a better family. I need to give a special mention to Loli, whom I miss a lot.

Finally, I would like to say thanks to my friends in Colombia, who were my safe zone over the last two years and with whom I shared laughs and defeats: Nicolas, Sebastian, Prada, Pinto, and Ferno, and the friends from the school that I visited here in Europe: Vic, Peña, and Caro. Thanks to all of you.

I am not a person with defined plans, but I am sure that what is coming will be even better.

Thanks iiiij;)

Palacký University Olomouc

Faculty of Science

Academic year: 2023/2024

ASSIGNMENT OF DIPLOMA THESIS

(project, art work, art performance)

Name and surname: Felipe CAMACHO HURTADO
Personal number: R220758
Study programme: N0532A330010 Geoinformatics and Cartography
Work topic: 3D VISUALIZATION AND ANALYSIS OF PATAGONIAN GLACIERS CHANGES USING EARTH OBSERVATION DATA
Assigning department: Department of Geoinformatics

Theses guidelines

The diploma thesis aims to analyze and visualize in 3D the development of glaciers in Patagonian icefields. The student will conduct a time-series analysis to estimate changes and identify trends in the glacier area, LST, and air temperature variables. The student will design and publish an interactive, user-friendly application where users can create, visualize, and export remote sensing and time-series products for icefields and custom areas of interest (AOI). As a second result, he designs and publishes a 3D web application that allows users to dynamically visualize and compare the remote sensing and time-series products created by the Google Earth engine. The student will create a website about the thesis following the rules available on the department's website and a poster about the diploma thesis in A2 format. The student will submit the entire text (text, attachments, poster, outputs, input and output data) in digital form on a storage medium and the thesis text in two bound copies to the department's secretary.

Extent of work report: max. 50 pages
Extent of graphics content: as needed
Form processing of diploma thesis: electronic
Language of elaboration: English

Recommended resources:

1. Aniya, M., Sato, H., Naruse, R., Skvarca, P., & Casassa, G. (1997). Recent Glacier Variations in the Southern Patagonia Icefield, South America. *Arctic and Alpine Research*, 29(1), 1–12. <https://doi.org/10.2307/1551831>
2. Arif, H., Mehmood, SA, & Ahmad, HH (2021). Spatiotemporal variations in snow cover using Google Earth engine in Gilgit-Baltistan, Pakistan. *Hydro Water Res.* Available online: https://www.researchgate.net/profile/Muhammad-Zain-Bin-Riaz/publication/352441989_Laboratory_measurements_of_velocity_and_hydrodynamic_force_over_coarse_fixed_rough_bed/links/60c9f39ca6fdcc01d47-measurements-of-velocity-and-hydrodynamic-force-over-coarse-fixed_rough_bed-rough-bed.pdf#page=294
3. Gede, M. (2018). Using Cesium for 3D Thematic Visualizations on the Web. <https://doi.org/10.5194/ica-proc-1-45-2018>
4. Mete, M. O., Guler, D., & Yomralioglu, T. (2018). Development of 3D web GIS application with open source library. *Selçuk Üniversitesi Mühendislik, Bilim Ve Teknoloji Dergisi*, 6, 818-824. <https://doi.org/10.15317/Scitech.2018.171>
5. Morelli, TL, Daly, C., Dobrowski, SZ, Dulen, DM, Ebersole, JL, Jackson, ST, ... & Beissinger, SR (2016). Managing climate change refugia for climate adaptation. *PloS one*, 11(8), e0159909. <https://doi.org/10.1371/journal.pone.0159909>
6. Rivera, A., Aravena, JC, Urra, A., Reid, B. (2023). Chilean Patagonian Glaciers and Environmental Change. In: Castilla, JC, Armesto Zamudio, JJ, Martínez-Harms, MJ, Tecklin, D. (eds) *Conservation in Chilean Patagonia. Integrated Science*, vol 19. Springer, Cham. https://doi.org/10.1007/978-3-031-39408-9_15
7. Smith, W.D., Dunning, S.A., Brough, S., Ross, N., & Telling, J. (2020). GERALDINE (Google Earth Engine supraglacial Debris INput dEtector): a new tool for identifying and monitoring supraglacial landslide inputs. *Earth Surface Dynamics*, 8(4), 1053-1065. <https://doi.org/10.5194/esurf-8-1053-2020>

8. Xu, F., Li, Z., Zhang, S., Huang, N., Quan, Z., Zhang, W., ... & Prishchepov, AV (2020). Mapping winter wheat with combinations of temporally aggregated Sentinel-2 and Landsat-8 data in Shandong Province, China. Remote Sensing, 12(12), 2065. <https://doi.org/10.3390/rs12122065>
9. Zhang, J., Jia, L., Menenti, M., Zhou, J., & Ren, S. (2021). Glacier area and snow cover changes in the range system surrounding tarim from 2000 to 2020 using google earth engine. Remote Sensing, 13(24), 5117. <https://doi.org/10.3390/rs13245117>

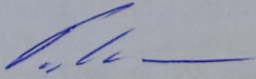
Supervisors of diploma thesis: **RNDr. Jan Brus, Ph.D.**
Department of Geoinformatics

Date of assignment of diploma thesis: **December 4, 2023**

Submission deadline of diploma thesis: **May 20, 2024**

L.S.

doc. RNDr. Martin Kubala, Ph.D.
Dean



prof. RNDr. Vilém Pechanec, Ph.D.
Head of Department

CONTENT

LIST OF ABBREVIATIONS	12
INTRODUCTION	13
1 OBJECTIVES.....	14
2 STATE OF ART.....	15
3 METHODOLOGY.....	31
3.1 Study Area	31
3.2 Data.....	32
3.2.1 Optical Satellite Data	33
3.2.2 Terrain Data	34
3.2.3 Vector Data.....	34
3.3 Software	34
3.4 Remote Sensing Indices	35
3.4.1 NDSI.....	35
3.4.2 NDWI.....	35
3.5 Statistical Errors	36
3.5.1 RMSD	36
3.5.2 RRMSD.....	36
3.6 General Procedure	36
4 TIME-SERIES ANALYSIS	38
4.1 Initial Feature and Image Collections	39
4.2 Functions.....	40
4.2.1 Image Clipping.....	40
4.2.2 Temperature Conversion	40
4.2.3 Clouds and Shadows Masking.....	41
4.2.4 Spectral Bands Renaming	41
4.2.5 Spectral Indices Calculation	42
4.2.6 Glacier Area Delineation.....	42
4.3 Workflow and Processes.....	42
4.3.1 Glacier Area Composites and Time-Series Chart.....	43
4.3.2 LST Composites and Time-Series Chart	44
4.3.3 Air Temperature Composites and Time-Series Chart	45
5 GEE WEB APPLICATION DEVELOPMENT.....	46
5.1 Main Panel	47
5.1.1 Introduction Panel	47
5.1.2 Glacier Geometry Panel	48
5.1.3 Summer Period Selection Panel	48
5.1.4 Execution Panel	48
5.1.5 Export Panel	49
5.1.6 Download Panel	49
5.2 Map Panel	49
5.2.1 Map.....	49

5.2.2	Legend Panels	50
5.3	Charts Panel.....	50
6	3D WEB APPLICATION DEVELOPMENT	51
6.1	GEE Web Application Outputs Processing	51
6.1.1	Summer Median Composites	51
6.1.2	Time-Series Charts.....	54
6.2	Cloud Hosting.....	56
6.3	CesiumJS Implementation	56
6.3.1	Cesium Viewer Setup	57
6.3.2	Data Preloading	58
6.3.3	Data Visualization.....	59
6.3.4	Data Interactivity	59
6.3.5	Complementary Widgets.....	60
7	USERS EVALUATION	61
8	RESULTS	63
8.1	Time-Series Analysis Outputs	63
8.2	Patagonian Glaciers Monitoring Application (GEE App)	65
8.3	3D Patagonian Glaciers Viewer (CesiumJS App).....	67
8.4	Survey Review	70
9	DISCUSSION	74
10	CONCLUSION	77
	REFERENCES AND INFORMATION SOURCES	
	ATTACHMENTS	
	APPENDIX	

LIST OF ABBREVIATIONS

Abbreviation	Meaning
AOI	Area of Interest
API	Application Programming Interface
ASTER	Advanced Spaceborne Thermal Emission and Reflection Radiometer
CCR	Climate Change Refugia
CSS	Cascading Style Sheets
CSV	Comma-Separated Values
DEM	Digital Elevation Model
ECMWF	European Centre for Medium-Range Weather Forecasts
EO	Earth Observation
GEE	Google Earth Engine
GIS	Geographical Information System
GLIMS	Global Land Ice Measurement from Space
GUI	Graphical User Interface
HTML	Hypertext Markup Language
JS	JavaScript
LST	Land Surface Temperature
MODIS	Terra Moderate Resolution Imaging Spectroradiometer
NASA	National Aeronautics and Space Administration
NDSI	Normalized Difference Snow Index
NDWI	Normalized Difference Water Index
NIR	Near Infrared
NPI	Northern Patagonian Icefield
PNG	Portable Network Graphics
RGI	Randolph Glacier Inventory
RMSD	Root Mean Square Deviation
RRMSD	Relative Root Mean Square Deviation
SCL	Scene Classification Layer
SPI	Southern Patagonian Icefield
SPOT	Satellite pour l'Observation de la Terre
SWIR	Short Wave Infrared
USGS	United States Geological Survey
WebGL	Web Graphics Library

INTRODUCTION

Glaciers, defined as “perennial mass of ice, and possibly firn and snow, originating on the land surface by the recrystallization of snow or other forms of solid precipitation and showing evidence of past or present flow” (Cogley et al., 2010, p. 45) are highly valuable as they provided ecosystem services which include water provision, sediment, nutrient inputs, flow regulation, flood mitigation, and biodiversity conservation (Rivera et al., 2023). As complex natural ecosystems, they are sensitive to climate change, reducing or increasing their extent in response to temperature and precipitation variation, making them crucial climate change indicators (Manquehual-Cheuque & Somos-Valenzuela, 2021). Due to these factors, glaciers are being studied more, with recent studies revealing that most glaciers worldwide are disappearing at an exponential rate due to warming temperatures, contributing to world sea level rise by 27 millimeters since 1961 (Bates, 2020).

Despite the increase in glacier analyses, glaciers in mountain regions are still poorly known due to difficult access and challenging environmental conditions (Carrasco-Escaff et al., 2023). This is the case for the Patagonian Andes, which is the largest glacierized area in South America with over 20000 km² of glaciers, concentrated mainly in the Northern Patagonian Icefield (NPI) and Southern Patagonian Icefield (SPI) (Pellicciotti et al., 2014). Studying this region is essential not only as most of the glaciers have been shrinking in recent decades, contributing a significant proportion of meltwater to the sea level rise in the 20th century (Rignot et al., 2003), but also because some of them are evidencing anomalous advancing (Rivera et al., 2012).

In this context, remote sensing technologies and Earth Observation (EO) data have been widely used since the 1990s to monitor global environmental dynamics and glacier changes in hard-to-reach areas (Yu et al., 2023). This includes EO satellite programs such as Landsat, Sentinel, and the European Centre for Medium-Range Weather Forecasts (ECMWF), with the ERA5-Land dataset for climate analyses. These technologies have introduced advantages such as global coverage, multi-spectral data, and high spatial-temporal resolution (Genzano et al., 2020). However, due to the increasing volume of EO data, known as “big data,” it is not feasible to access, collect, and analyze data using traditional methods (Di Tullio et al., 2018). Therefore, cloud computing platforms, such as Google Earth Engine (GEE), have gained popularity as efficient ways for storing, accessing, and analyzing petabytes of EO data, offering free access to fast computations via the internet (Amani et al., 2020).

Although GEE provides a solid framework for glacier analyses and visualization in 2D, having a 3D perspective is fundamental as glacier processes are highly determined by their altitude (Manquehual-Cheuque & Somos-Valenzuela, 2021). Currently, with the rise of Web Graphics Library (WebGL) and JavaScript (JS) libraries like CesiumJS, which enable the creation of 3D online environments (Schanche, 2020), 3D applications can be developed to enhance data analysis and visualization, providing deeper insights into environmental changes (Van Ackere et al., 2016).

This diploma thesis aims to develop a GEE web application for the creation, visualization, and export of remote-sensing and time-series products that allow quantitative and qualitative estimation of glacier area, Land Surface Temperature (LST), and air temperature changes in the NPI and SPI glaciers, for the summer periods between 2018 and 2023. Additionally, it aims to provide a 3D application that lets users add, visualize, interact, and compare the remote-sensing and time-series products obtained from the GEE web application.

1 OBJECTIVES

This diploma thesis aims to address the lack of studies and 3D visualizations of NPI and SPI glaciers by developing a GEE web application for the creation, visualization, and export of remote-sensing and time-series products that permit the quantitative and qualitative estimation of glacier area, LST, and air temperature changes of Patagonian glaciers, in the summer periods between 2018 and 2023, using Landsat 8-9, Sentinel-2, and ERA5-Land imagery. Moreover, it aims to provide a 3D web application that allows users to add, visualize, interact, and compare the remote-sensing and time-series products obtained from the GEE web application. The specific goals of the study are:

- i. Conduct a time-series analysis to estimate changes and identify trends in glacier area, LST, and air temperature.
- ii. Design and publish an interactive, user-friendly GEE application where users can create, visualize, and export remote sensing and time-series products for the NPI and SPI glaciers and custom Areas of Interest (AOI).
- iii. Develop and publish a 3D web application using CesiumJS that allows users to dynamically visualize and compare the remote sensing and time-series products derived from the GEE web application using widgets such as swipe, sidebar, and display controls.
- iv. Evaluate the user's reception of the GEE and 3D web applications by implementing an online questionnaire.

The results of this work will be open-source, ready-to-use applications that scientific and general communities can use and customize. These applications will allow users to visualize glaciers interactively and innovatively, and generate EO outputs that can be used in user-specific analyses. Such accessibility and customizability will significantly enhance understanding of the Patagonian glacier processes and promote interest in these natural features.

2 STATE OF ART

This chapter reviews the use of EO data and techniques in recent Patagonian Glaciers analyses, the implementation of the GEE platform in glaciological research, and the development of GEE apps. Additionally, it explores the current state of 3D web mapping and available CesiumJS apps.

Patagonian glaciers studies with EO data

The NPI and SPI are considered the most extensive ice bodies in the Andes Cordillera (Carrasco-Escaff et al., 2023), constituting the largest temperate glacier complex in the Southern Hemisphere (Meier et al., 2018). Because of their extent, they play an essential role as providers of natural and cultural services, including water provision, biodiversity conservation, flow regulation, flood mitigation, and tourism, a fundamental source of economic revenue in this region (Rivera et al., 2023). The Patagonian climate is highly influenced by climatic and weather changes, associated with temperature, precipitation, wind strength (Carrasco-Escaff et al., 2023; Coronato, 2020; Florath et al., 2021), and altitude (Manquehual-Cheuque & Somos-Valenzuela, 2021) variations. As a result, temperature increases, snow line rises, decreasing precipitation, and weak winds (Bravo Lechuga, 2020; Coronato, 2020; Rivera et al., 2023) have had a direct impact on the glaciological surface processes (Carrasco-Escaff et al., 2023) resulting in glacier area and volume loss, frontal ablation, mass loss, and glacier lakes increase (Davies et al., 2023; De Vries et al., 2023; Minowa et al., 2021; Sáez et al., 2019; Shugar et al., 2020).

Regardless of the importance of Patagonian glaciers and the impact of climatic changing factors on their processes, there is still a lack of knowledge, inadequate research, and insufficient in-situ measurements of this area. This situation is attributed to its extreme environment, harsh access conditions (Florath et al., 2021), sparse population (Carrasco-Escaff et al., 2023), and lack of interest from North American and European glaciologists (Aniya et al., 1997). EO data and techniques have been implemented to overcome these challenges as they provide more information on inaccessible glacier areas than terrestrial methods (Florath et al., 2021). Moreover, because of the high spatiotemporal variability of snow and glacier processes, remote sensing imagery, such as optical, synthetic aperture radar, and microwave, can offer insights into snow properties by taking advantage of the electromagnetic spectrum (Beltramone et al., 2020).

Regarding studies of glacier area and frontal ablation, defined as the combination of submarine melt and mechanical calving (Truffer & Roman, 2016), of Patagonian Glaciers, Rivera et al. (2004) estimated the frontal and areal changes of SPI glaciers from 1945 to 1975 by comparing existing cartography with Global Positioning System and satellite imagery data. Specifically, they used two Landsat Thematic Mapper images acquired on January 14, 1986, two Landsat ETM+ images acquired on October 27, 2000, and one Advanced Spaceborne Thermal Emission and Reflection Radiometer (ASTER) image acquired on January 12, 2003. After mosaicking and georeferencing the images, the authors performed a land classification for glacier, ice-free areas, and lake covers, using color image composites (Figure 1) with bands 1, 4, and 5 and the bands 4-5 ratio proposed by Paul et al. (2002). As a result, the study observed significant glacier thinning and retreat with a total area loss of 62.2 km², equivalent to 8% of the glacier area of the studied region in 1945. This was associated with the increasing temperature but could not fully explain the phenomena, concluding that further measurements and research would have to be done.

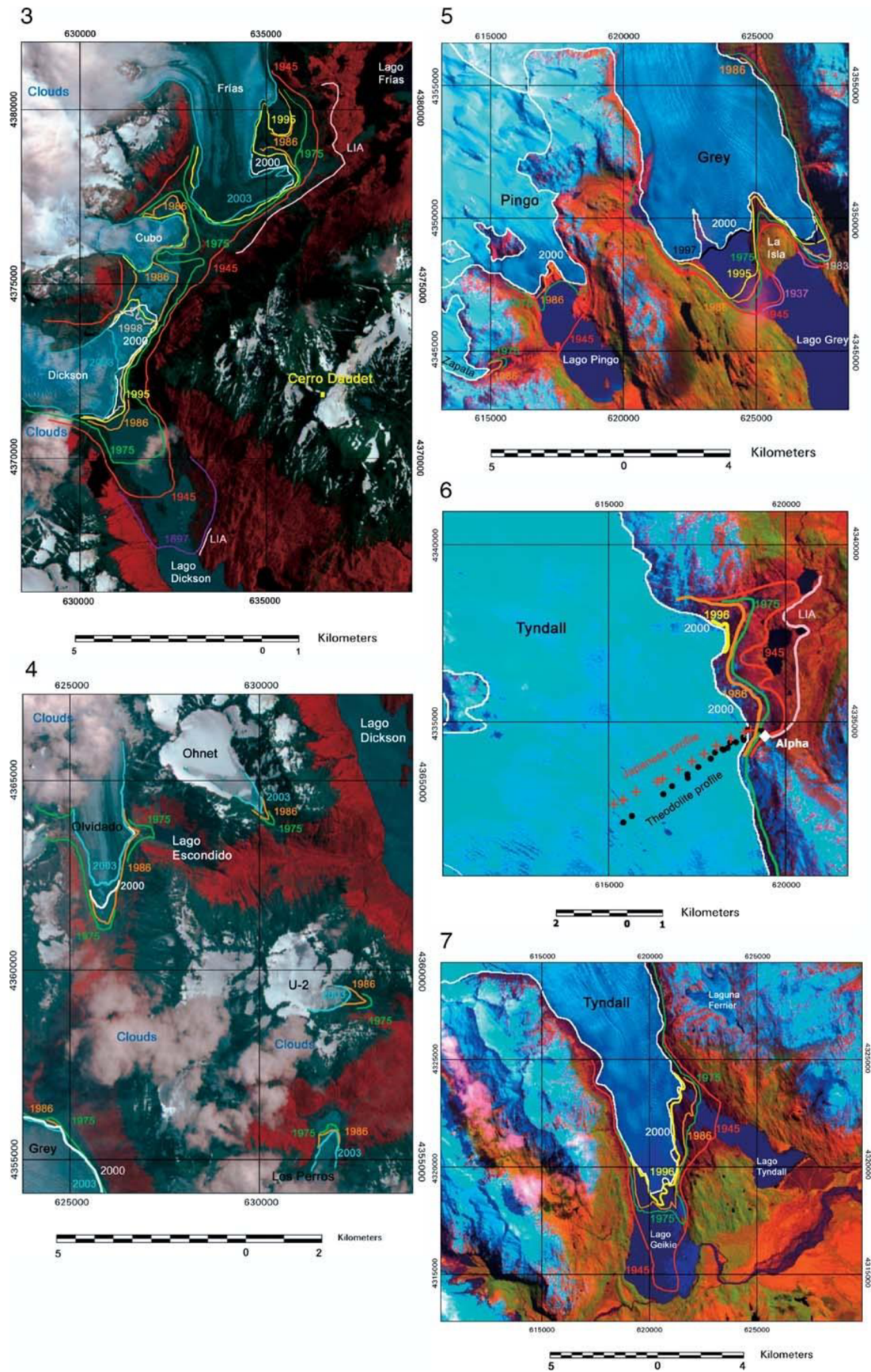


Figure 1 ASTER and Landsat ETM+ composite images showing frontal variations of selected Patagonian glaciers with UTM coordinates expressed in meters: 3) Glaciers Dickson, Frias, and Cubo 4) Glaciers Olvidado, Los Perros, Ohnet, and U-2. 5) Glaciers Grey, Pingo, and Zapata. 6) Glacier Tyndall. 7) Glacier Tyndall Calving Ice Fronts (Rivera et al., 2004).

Sáez et al. (2019) also conducted a temporal study on the area and volume changes of the Grey, Tyndall, and Dickson glaciers in the SPI and southeastern Patagonian icefield. The changes were estimated between 1998 and 2017 by combining Digital Terrain Models with Landsat 5, 7, and 8 satellite imagery from December to April, as that period is characterized by low cloud presence and critical glacier melting (Sáez et al., 2019). After performing radiometric corrections and pan-sharpening on Landsat imagery, Sáez et al. (2019) calculated the Normalized Difference Snow Index (NDSI) and applied thresholds of 0.4 and 0.42 to identify snow and ice, respectively (Copé de los Mozos, 2014; Dozier, 1989). This process resulted in the creation of delimitation polygons that identified the surface and area variations of the glaciers, which, when combined with available Digital Elevation Models (DEM), generated Triangulated Irregular Networks for volume calculation. Using this methodology, Sáez et al. (2019) estimated losses of 10.87 km² and 2.6 km³ for the Grey Glacier, 13.68 km² and 6.8 km³ for the Tyndall glacier, and 3.94 km² and 0.6 km³ for the Dickson glacier, associating these losses with decreases in average annual rainfall and temperature increases.

Focusing on glacier areas not only in the Patagonian region but worldwide, Windnagel et al. (2022) presented the first systematic answer to the question of which glaciers are the largest in the world by reviewing data from two glacier inventories: Global Land Ice Measurements from Space (GLIMS) and the Randolph Glacier Inventory (RGI) 6.0. Initially, they highlighted the impact of glacier definition and mapping on area analyses and emphasized distinguishing between individual glaciers and glacier complexes. According to Windnagel et al. (2002), glacier complexes are preferred when carrying out land-cover classifications, while individual glaciers should be used when evaluating meltwater input to individual hydrological drainage basins. Considering this, the study queried the GLIMS and RGI databases to extract the glacier area attribute, selecting the most recent measurement in case the glacier's size differed in both databases and averaging them if the measurement year was the same. Then, glacier complexes were identified by merging glaciers with shared boundaries and calculating their areas using a Python planar area function in an equal-area projection (Windnagel et al., 2002). The findings revealed that the most extensive glacier complex (Figure 2) was on the Antarctic Peninsula, with an area of 80852 km². Moreover, the biggest glacier was the Seller Glacier, with an extent of 7018 km². Additionally, the SPI evidenced an area of 13326 km², with PIO XI glacier being the largest in this icefield, with an extent of 1345 km². The study concluded that although the question is simple, ranking the glaciers by area is a big challenge as the current inventories are inconsistent, presenting different years and measurement methodologies, complicating the development of accurate analyses.

De Vries et al. (2023) studied the Patagonian icefield volume loss, as Sáez et al. (2019). In this research, the authors calculated the rate of volume loss for eleven sub-basins between 2006 and 2019 by combining runoff data, river discharge data from gauging stations, precipitation data derived from the Tropical Rainfall Measuring Mission and the Global Precipitation Measuring Mission, and evapotranspiration data from Terra Moderate Resolution Imaging Spectroradiometer (MODIS) MOD16A2. After calculating the annual relative glacier volume loss, De Vries et al. (2023) evidenced a significant increase in ice volume loss for seven glacierized sub-basins, with a total rate anomaly of 135 ± 50 km³, ranging from 7.06 ± 1.69 ma⁻¹ increase in ice loss to a 3.18 ± 1.48 ma⁻¹ decrease in ice loss, supporting the rapid volume loss of Patagonia's lake-terminating glaciers.

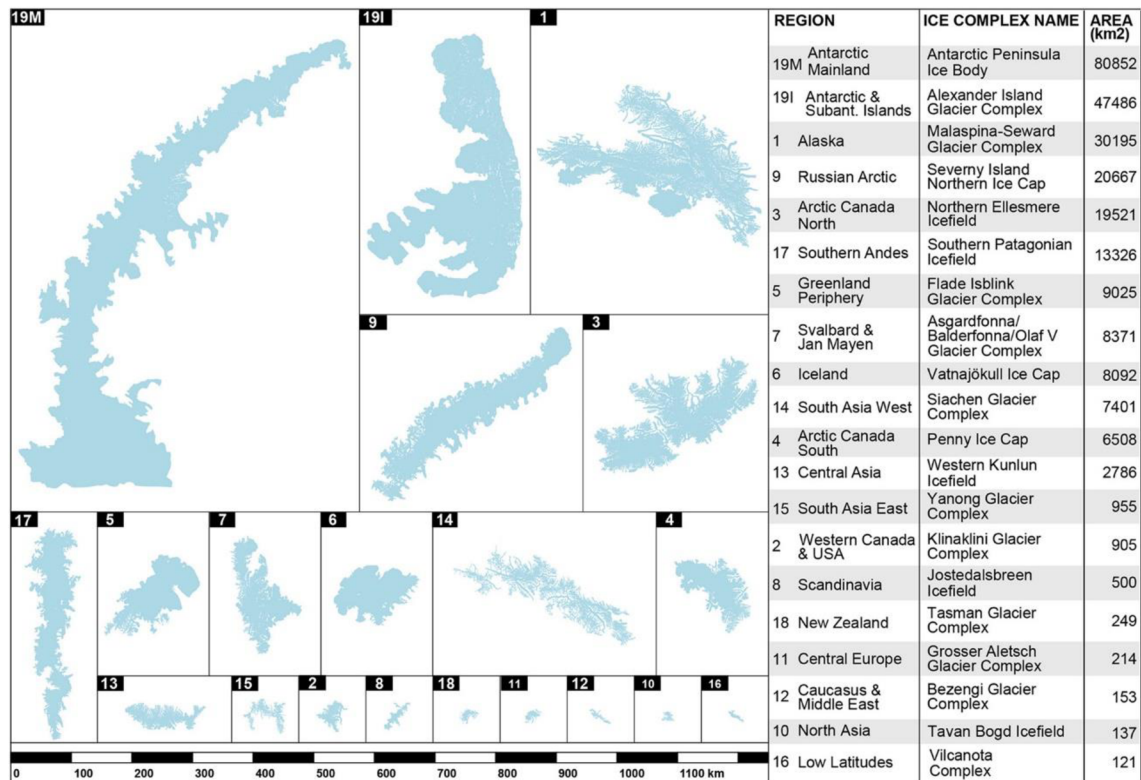


Figure 2 Largest glacier complexes for the 19 first-order regions, from highest to lowest area (Windnagel et al., 2022).

In the last few years, the mass loss of the Patagonian icefields has been researched, particularly for calving glaciers, which present a more complex reaction to climate variability than land-terminating glaciers (Minowa et al., 2021). Patagonian glaciers are experiencing rapid ice mass loss, contributing 3 mm to sea-level rise between 1961 and 2016 (Zemp et al., 2019). Consequently, addressing the mass loss of this region is critical for understanding the regional drivers, variability, and climate interactions promoting these changes (Davies et al., 2023).

Minowa et al. (2021) developed a frontal ablation and ice mass change study for 38 calving Patagonian glaciers, larger than 40 km² in the NPI and 100 km² in the SPI, respectively, from 2000 to 2019. This study was based on elevation changes, surface speeds, modeled ice thickness, and ice-front positions derived from EO data. Specifically, DEMs provided the elevation change rate necessary for calculating the ice thickness over time, and orthorectified imagery from Landsat 4,5,7 and 8, Japanese Earth Resources Satellite, and Satellite pour l'Observation de la Terre (SPOT) 1-5 were utilized to manually delineate the frontal glacier and map 3969 ice front positions. Additionally, having as reference the RGI 6.0 glacier boundaries, annual ice surface flow speeds were retrieved. As a result, Minowa et al. (2021) estimated a mean frontal ablation of both NPI and SPI of -24.1 ± 1.7 Gt a⁻¹, with the SPI experiencing a significantly larger ablation of -21.6 ± 1.7 Gt a⁻¹, compared to the NPI, which had ablation of -2.5 ± 0.5 Gt a⁻¹. Moreover, a total mass loss of 15.2 ± 3.5 Gt a⁻¹ was measured, resulting from 10.73 ± 2.7 Gt a⁻¹ for the SPI and 4.5 ± 0.8 Gt a⁻¹ for the NPI. The study concluded that frontal ablation increases were the primary contributors to mass loss in most glaciers of the SPI. In contrast, the negative surface mass balance was the main driver of mass loss in NPI glaciers.

McDonnell et al. (2022), motivated by the unknowns of the mass budgets in the NPI and SPI, along with unique characteristics and phenomena associated with this region, including glaciers that interact with lakes and fjords at their termini and small tidewater glaciers with high thinning rates, studied the mass balance, defined as the difference between total snow and ice accumulation and total snow and ice loss from a glacier (Pelto & Riedel, 2001), in NPI and SPI since 1970. Using declassified Hexagon imagery and remote sensing data such as DEMs, Landsat 8, and ASTER imagery, the authors evidenced a negative geodetic mass balance that increased by a factor of 1.2 and 2.4 for the NPI and SPI, correspondingly, possibly associated with feedback processes influenced by climate change.

Most of the studies presented until now have developed Patagonian glacier extent, volume, mass balance, and frontal ablation analyses. However, remote sensing techniques have also been used to map areas with different land cover types. Florath et al. (2021) evaluated the possibility of using multispectral and hyperspectral imagery with various classification algorithms to identify five different snow and ice types in the Torres del Paine National Park, constituted by the Grey, Tyndall, and Dickson glaciers of the SPI. For this purpose, the authors defined the following classes to be identified:

- Glacier ice: ice that is formed in glaciers' lower areas, where snow accumulation exceeds ablation
- Refreezing ice: superimposed and blue ice resulting from new snow falling over already existing glaciers
- Dirty ice: glacier ice mixed with debris such as rock materials from the glacier surroundings, affecting its spectral reflectance
- Aged snow: snow that has been melted and refrozen due to solar and temperature changes, resulting in lower reflectance
- Fresh snow: snow with lower water content and fewer impurities, showing higher reflectance.

Having these classes defined, Sentinel-2 imagery was pre-processed, and atmospheric corrections were applied using the Sen2Cor software. Afterward, hyperspectral data was transferred to these images to create synthetic labeled Sentinel-2 images as reference data for snow and ice cover types. For the classification, the NDSI, the Normalized Difference Glacier Index, and the Normalized Difference Snow Ice Index were used with thresholds based on Keshri et al. (2009). The classification algorithms implemented by the authors included two unsupervised approaches, k-means clustering and a rule-based classification, and two supervised approaches, Linear Discriminant Analysis and Random Forest. As a result, the authors provided evidence of a good classification of all the tested algorithms in the Tyndall glacier, with the Random Forests algorithm being the most accurate (Figure 3). The research carried out by Florath et al. (2021) is an excellent example of the usage of EO data and techniques for mapping ice and snow in remote areas. It highlights the importance of differentiating between different ice and snow cover types, as they influence the glaciers melting or refreezing process differently. Moreover, it evidences the complexity of defining and identifying ice and snow land covers and provides helpful information on snow wetness and water resource management, which is critical for understanding melting and water run-off events (Florath et al., 2021)

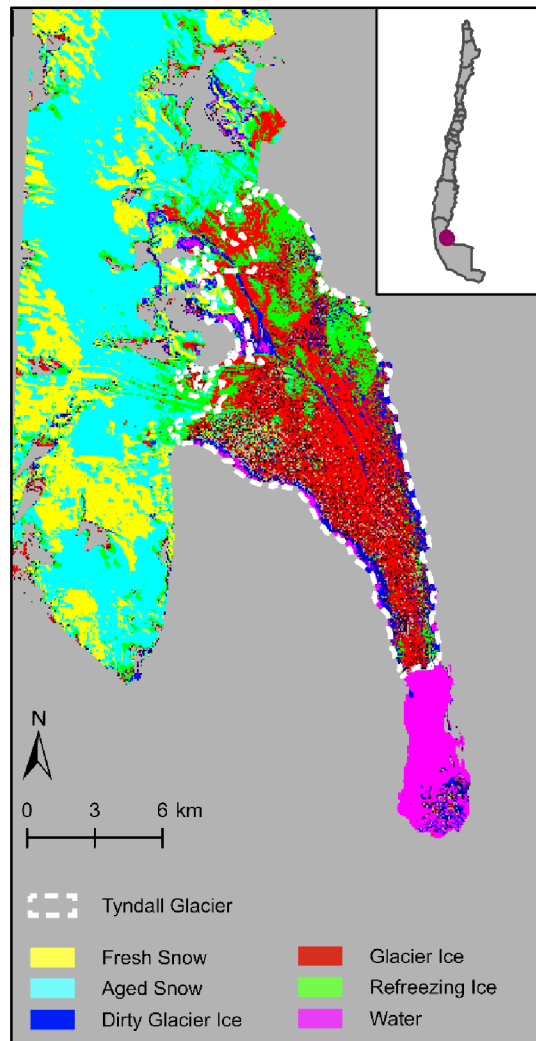


Figure 3 Ice and snow classification using the Random Forest algorithm in Torre del Paine National Park (Florath et al., 2021).

The impact of climate dynamics on glaciers has also been studied in recent years as a response to the increasing melting, frontal ablation, and loss of glacier area and volume, discussed previously in this section. Understanding the climate variability of the Patagonian region is a big challenge, as glaciers are complex natural ecosystems determined by water content, rock material, and sediments (Rivera et al., 2023). Additionally, although glaciers are highly influenced by air temperature, precipitation, wind, and regional and local climate (Bravo Lechuga, 2020), they respond differently to the same climate perturbation (Sagredo & Lowell, 2021). In the Patagonian Glaciers case, it has been observed that high precipitation dominates glacier processes on the western side. In contrast, the eastern side is more sensitive to air temperature, wind speed, and humidity changes (Cook et al., 2003). Considering the glaciers' fluctuations and environmental disturbances (Rivera et al., 2023), it is necessary to improve the meteorological and glaciological monitoring of Patagonian ice fields through the implementation of onsite measuring networks and remote sensing campaigns. This will enhance the knowledge and data availability to boost confidence in models that aim to simulate future climate in this region (Rivera et al., 2023; Bravo Lechuga, 2020).

Based on the current Patagonian climate scenario and the need to understand the climate change impact in this area, Manquehual-Cheuque & Somos-Valenzuela (2021)

performed a study to identify resilient areas against climate variability that can potentially act as Climate Change Refugia (CCR). CCRs are characterized because they provide physical, ecological, and socio-cultural services over time under changing climate conditions (Morelli et al., 2016). In this research, the authors implemented the Maxent machine learning method to estimate the probability of CCRs based on glacier delimitation and environmental variables such as temperature, precipitation, and altitude. The data were gathered from the Chilean glacier cover inventory and the ERA-Interim atmospheric reanalysis, with a resolution of 1 km² at the equator (Manquehual-Cheuque & Somos-Valenzuela, 2021). As a result, for an AOI of 189000 km² in the Patagonian region, the research observed that temperature and altitude were the most significant variables for determining CCRs. Moreover, they evidenced that most CCRs were present at high altitudes, while small glaciers at low altitudes were likely to disappear (Manquehual-Cheuque & Somos-Valenzuela, 2021). This research adequately shows the importance of considering temperature and altitude variables when analyzing the impact of climate change on glaciological processes, as they are critical drivers of ongoing and future glacier changes.

Glaciers Research using Google Earth Engine

GEE is currently the most popular free cloud computing platform for large-scale geospatial analysis due to the availability of vast amounts of EO data, image processing tools, and machine learning algorithms (Tamiminia et al., 2020). This platform has been widely used for different purposes, such as vegetation analyses, land cover classifications, natural hazards identification, and hydrology studies, resulting in a significant popularity increase, especially since 2017, based on the number of published papers (Kumar & Mutanga, 2018). After reviewing 443 GEE journal articles between January 2010 and mid-May 2020, Amani et al. (2020) observed contributions (Figure 4) of 90 papers on vegetation, 77 on agriculture, and 68 on hydrology, with only 7.5% of the total reviewed papers corresponding to South America. Moreover, Tamiminia et al. (2020) evidenced that over a total of 349 GEE articles analyzed from 2010 to 2019, 74 papers were associated with crop mapping and agricultural monitoring, followed by 62 water studies and 56 land use/land cover research, with correspondence of 8% for South America. Regarding the most used data, Kumar & Mutanga (2018) observed that over 300 GEE journal papers published between 2011 and June 2017, 159 used Landsat, 80 MODIS, 24 SPOT, and 19 Sentinel.

Within hydrology and water studies, topics such as surface water, lakes, snow, and river mapping are discussed, along with glaciological analyses (Amani et al., 2020; Tamiminia et al., 2020). Specifically, in the glaciers' context, GEE has been used for addressing and measuring glacier area and snow cover changes (Ali et al., 2023; Arif et al., 2021; Turpo Cayo et al., 2022; Zhang et al., 2021;), mapping and estimating glacier lake changes over time (Bazilova et al., 2022; Sun et al., 2022;), detecting glacier snow line altitude (Li et al., 2022) and landslides (Lindsay et al., 2022), and developing glacier surface velocity analyses (Di Tullio et al., 2018). Overall, GEE is nowadays one of the most important cloud computing platforms that allows users to perform analyses on a wide range of topics using EO data and techniques. However, even though it has already been used for glacier monitoring, the lack of studies carried out in South America, evidenced by Amani et al. (2020) and Tamiminia et al. (2020), is a gap that must be addressed.

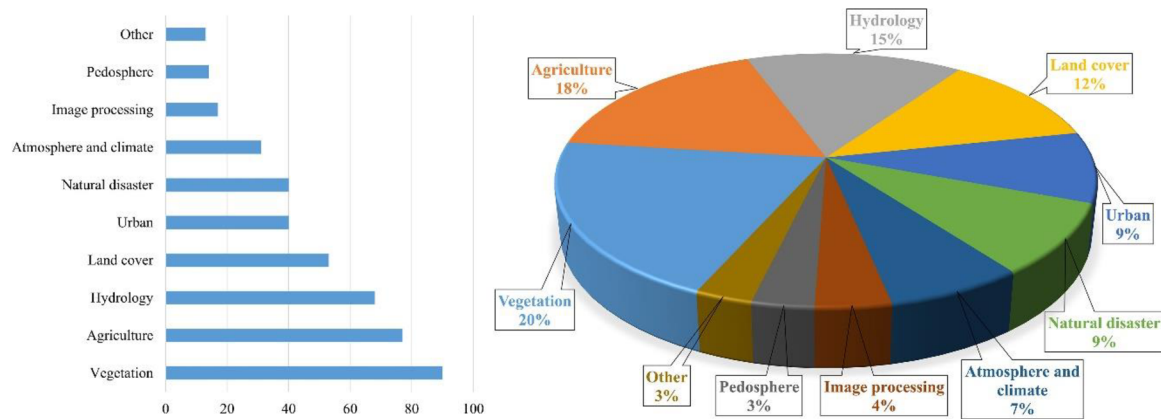


Figure 4 Distribution of GEE usage categories across 443 papers (Amani et al., 2020).

In detail, Zhang et al. (2021) carried out extensive glaciological research, which developed a methodology with GEE to understand the anomalous positive mass budgets and relative stability exhibited by the glaciers in West Kunlun and Pamir. For this purpose, the authors utilized MODIS, Landsat 5-8, DEMs, and meteorological data. They applied the NDSI and Normalized Difference Water Index (NDWI) to MODIS reflectance data between 2000 and 2021 to extract glacier areas and seasonal snow cover. Even though the NDSI accurately distinguishes between glacier/snow, clouds, and shadows, identifying glacier and snow independently is complex due to their similar spectral properties (Zhang et al., 2021). As a result, Zhang et al. (2021) implemented two parallel workflows. The first one to extract and delimit the glacier area by retrieving MODIS data for the summer period (July to September), when snow that does not contribute to glacier mass balance melts, being an optimal season for separating glaciers and snow cover (Huang et al., 2021). The second workflow focused on extracting snow cover using MODIS-8-day interval images. In detail, the glacier extraction workflow involved the following steps:

1. creating annual summer median composite images from summer MODIS data using the GEE reducer function,
2. calculating NDSI and the Near Infrared (NIR) for the annual summer median composites, identifying glacier pixels as those with values of $NDSI \geq 0.4$ and $NIR \geq 0.11$,
3. generating a water mask for the annual summer median composites using the NDWI, identifying and removing water pixels with $NDWI \geq 0.2$ and $NIR < 0.2$,
4. delimiting glacier areas based on the NDSI, NDWI, and NIR values for each pixel.

The resulting glacier areas were compared with those extracted from Landsat 5-8 satellite imagery. Zhang et al. (2021) estimated the glacier change rate by fitting a linear regression to the annual glacier area values and evaluating its accuracy with the Root Mean Square Deviation (RMSD) and Relative Root Mean Square Deviation (RRMSD) statistical errors. As a result, the authors estimated a glacier area decrease in the Tarim Basin of 7975.71 km² with an annual decrease of 0.94%/year. The workflow proposed by Zhang et al. (2021) takes advantage of GEE's processing capabilities with EO data. However, its accuracy is reduced by limitations such as the misclassification of water and glacier pixels and the impossibility of detecting glacier areas in summer periods for high-altitude glaciers with long-duration perennial snow.

Turpo Cayo et al. (2022) developed a study to retrieve the area of tropical Andean glaciers by performing a time-series analysis with Landsat 5,7,8 imagery from 1985 to 2020. The methodology is similar to the one presented by Zhang et al. (2021) but differs in some key aspects. It consists of six steps:

1. selecting all Landsat images with cloud cover equal to or less than 70% available between 1985-2020 and masking clouds and cloud shadows,
2. calculating NDSI for all the retrieved images,
3. creating annual image composites, reducing NDSI, RED, and NIR bands,
4. implementing an empirical decision tree to classify glaciers in the annual image composites,
5. applying post-classification filters,
6. conducting accuracy assessment.

Regarding clouds and cloud shadow masking, Turpo Cayo et al. (2022) used the CloudScore technique for masking clouds and the Temporal Dark Outlier Mask algorithm and Band Quality Assessment for masking cloud shadows. In step 3, the NDSI was reduced using the minimum reducer, while RED and NIR used the median reducer with the 25th NDSI percentile. Finally, after implementing the empirical decision tree based on 9800 samples, Turpo Cayo et al. (2022) applied several post-classification filters, such as gap fill, frequency filter, and temporal filter, to remove noise and gaps associated with cloud presence. With this methodology, the conducted study evidenced a reduction of tropical Andean glaciers area from 2439.38 km² to 1409.11 km² between 1990 and 2020, with the smallest areas being the most affected, experiencing more than 90% reduction in the same period (Figure 5). Turpo Cayo et al. (2022) research is another example of how glacier areas can be estimated by combining annual composites, reducers, remote sensing indices such as NDSI, and the analysis capabilities provided by GEE.

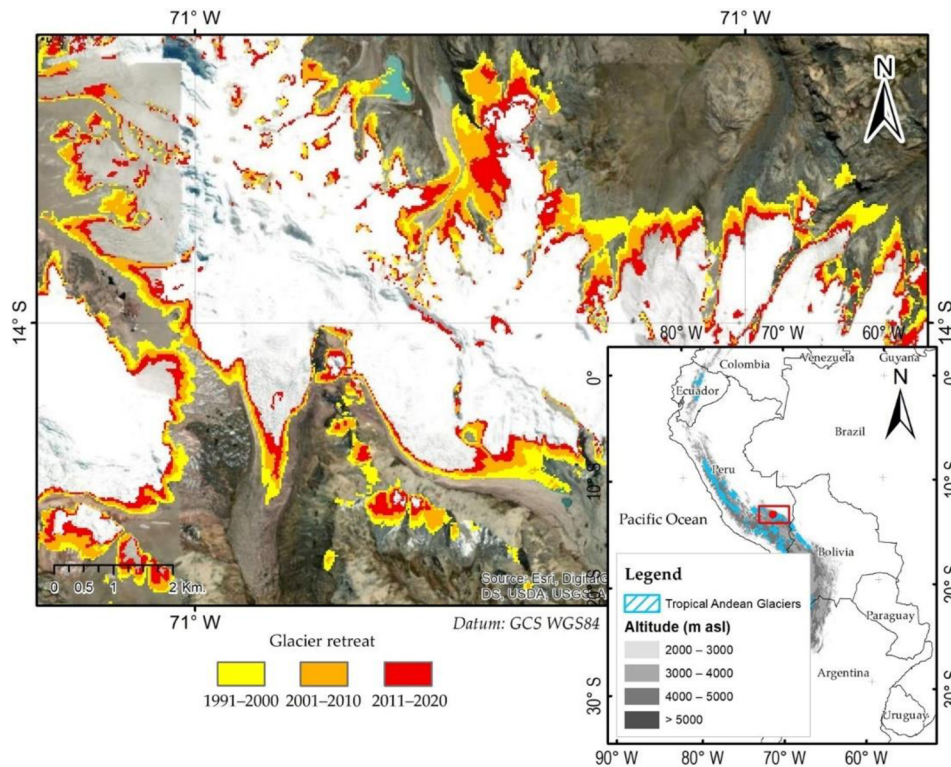


Figure 5 Glacier retreat between 1990 to 2020 in Vilcanota Cordillera (Turbo Cayo et al., 2020).

The research carried out by Zhang et al. (2021) and Turpo Cayo et al. (2022) analyzed glacier area changes from a pixel-based perspective. However, GEE also supports object-based image analyses for classifying imagery, which includes non-iterative clustering, k-means, and G-means techniques (Liu et al., 2018). The implementation of this approach increases accuracy by incorporating surrounding pixels into single objects and considering variables such as texture and shape (Blaschke, 2010). Ali et al. (2023) applied the object-based image approach to Landsat imagery to quantify glacier recession in the Novaya Zemlya region between 1986-89 and 2019-21. Specifically, they used a non-iterative clustering algorithm, which includes seeds, compactness, connectivity, and neighborhood size parameters, to segment the image. Then, with the random forest classifier and 728 samples, they detected glacier and non-glacier objects. With this methodology, Ali et al. (2023) demonstrated a total reduction of 5.8% in the glacier area between 1986-89 and 2019-21. The research proves GEE's ability to integrate machine learning algorithms and object-based image analysis techniques with EO data to retrieve glacier areas.

The studies conducted by Zhang et al. (2021), Turpo Cayo et al. (2022), and Liu et al. (2018), discussed in this section, demonstrate the ongoing and increasing usage and applicability of the GEE platform for mapping glacier areas over time through the usage of various EO data, including Landsat, ASTER, and DEMs. GEE enables users to access and manage remote sensing data faster and create annual or monthly image composites (Arif et al., 2021). This is done through image reduction operations and calculating different remote sensing indexes, such as NDSI and NDWI, with pixel and object-based perspectives. Nevertheless, GEE is mostly utilized in Asia, Europe, and North America, leading to a significant opportunity for expansion in South America, particularly in regions like Patagonia. Also, there is a chance to work with EO data that has not been extensively used, such as Sentinel Imagery.

Google Earth Engine Apps

Until now, only the GEE advantages have been mentioned and discussed. However, because of the complex nature of remote sensing analyses, specifically in terms of the required knowledge, there is a barrier that limits the usage of this platform to people without advanced training (Scheip & Wegmann, 2021). Indeed, using GEE for geospatial analyses requires familiarity with EO data and techniques and programming languages such as JS and Python, whose learning is time-consuming and a big challenge for users without a computational background (Zhang et al., 2020). To address this limitation, GEE provides a JS client library, accessed through the GEE Code Editor, that enables users to create GEE-enabled web applications and publish them through the Earth Engine Apps platform (Zhang et al., 2020). As a result, the public-facing applications created with GEE not only enhance scientists' accessibility to EO data and remote sensing analyses but also provide user-friendly experiences to the non-scientific public (Scheip & Wegmann, 2021). Among the main capabilities of GEE web applications is the possibility of creating a graphical user interface (GUI) by combining standard Hypertext Markup Language (HTML) and native widgets such as buttons, labels, and sliders. Additionally, it allows users to modify variables and visualization parameters in real-time (Scheip & Wegmann, 2021). The currently available GEE web applications cover a wide range of topics and functionalities, including natural hazards mapping (Scheip & Wegmann, 2021), agricultural modeling (Zhang et al., 2020), volcanoes analysis (Genzano et al., 2020), and supraglacial landslide monitoring (Smith et al., 2020), with the possibility to visualize data, create time-series charts, and export results.

For example, HazMapper, or Hazard Mapper, is an open-access GEE web application (Figure 6) that provides a map, Geographical Information Systems (GIS) products from Sentinel and Landsat imagery, including the relative difference NDVI, to visualize, characterize, and monitor landscape changes, in vegetated environments, caused by human activities or natural dynamics (Scheip & Wegmann, 2021). In the interface of HazMapper, users have access to examples that showcase the capabilities of the application, a parameters panel where date, cloud cover, and slope values can be modified, along with two buttons to update the visualization and download the available imagery (NDVI, pre-image, post-image, and elevation data). This GEE web application aims to democratize access to multispectral satellite imagery analyses, specifically providing researchers, emergency responders, and the non-scientific community a tool for addressing natural hazard impact (Scheip & Wegmann, 2021).

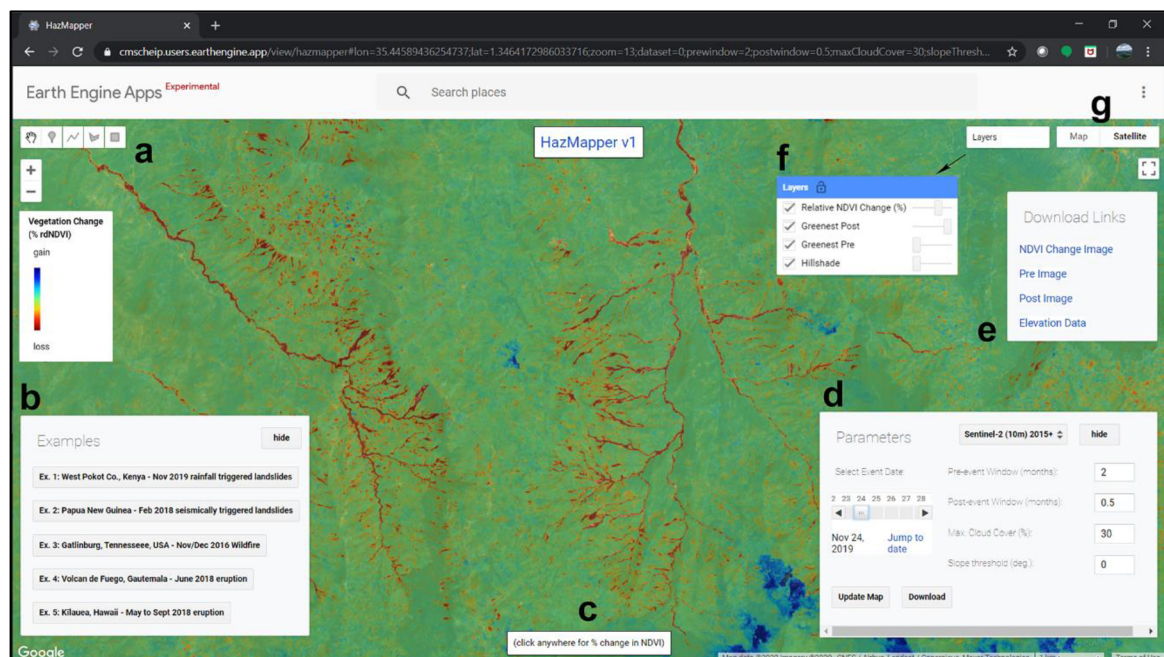


Figure 6 The user interface of the Hazmapper GEE Application (Scheip & Wegmann, 2021).

AgKit4EE is another open-source toolkit that users can work with, modify, and distribute without restriction (Zhang et al., 2020). It contains two GEE web applications and various JS functions for modeling and performing land use analysis with the Cropland Data Layer of the United States. The Cropland Explorer (Figure 7) and Crop Frequency Explorer (Figure 8) GEE web applications developed by Zhang et al. (2020) were designed to visualize, explore, and export cropland products by demand through a GUI that includes a map explorer and configuration panel with charts, labels, and buttons. Specifically, in the Cropland Explorer, users can filter the displayed data and calculate crop area statistics based on layer, year, crop types, and boundary parameters. In comparison, the Crop Frequency Explorer creates a crop frequency map based on the user's crop type and year selection (Zhang et al., 2020). These GEE web applications facilitate access to EO data and provide a custom, fully extensible structure that can be expanded by creating new JS functions (Zhang et al., 2020). Therefore, the public and scientific community benefit from the accessibility to their functionalities and the less time it takes to improve them.

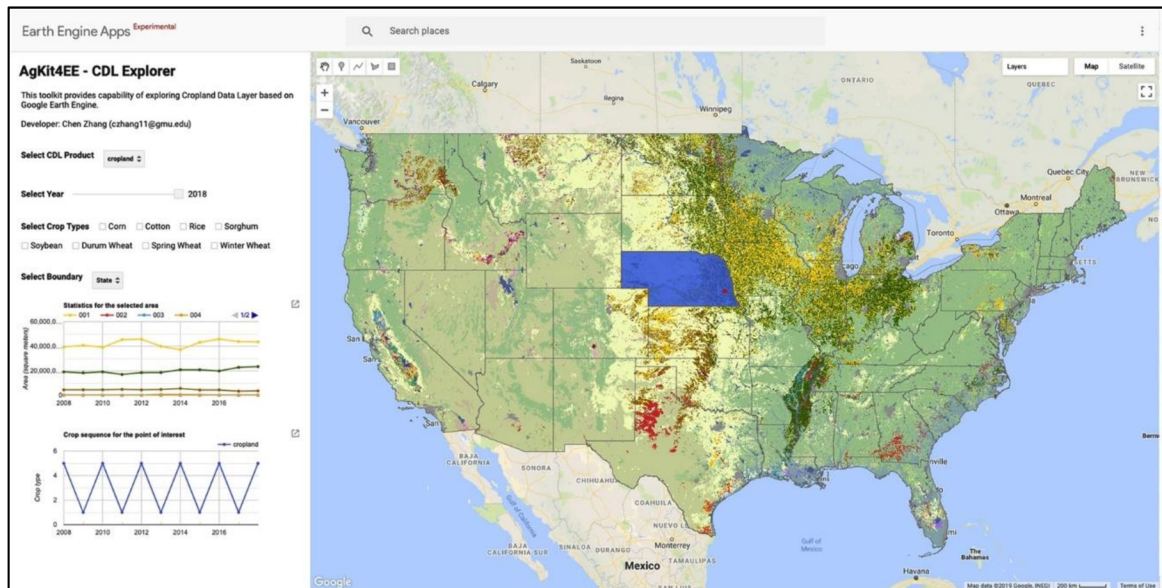


Figure 7 AgKit4EE Cropland Explorer GUI (Zhang et al., 2020).

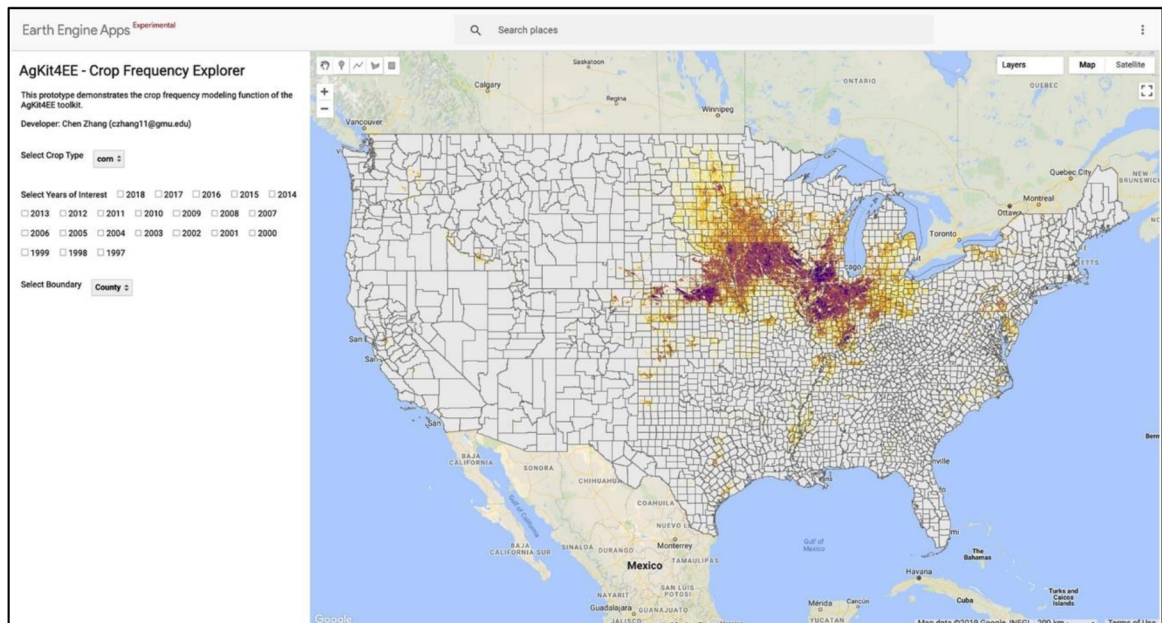


Figure 8 AgKit4EE Crop Frequency Explorer GUI (Zhang et al., 2020).

When creating a GEE web application, receiving feedback from the end-users is crucial to understand areas for improvement or find possible bugs. Genzano et al. (2020) considered this aspect. They developed the Normalized Hot Spot Indices tool (Figure 9), which combines Sentinel and Landsat imagery to map and monitor the thermal volcanic anomalies of more than 1400 volcanoes. The GUI comprises a selector for the volcanoes, a filter for the date and buffer distance selector, and a link that redirects the user to a feedback survey. The authors used the comments from the survey to improve the available information and add functionalities. The research demonstrates the scalability of GEE web applications as new data and tools can be added by modifying the existing code according to user and scientific needs. Additionally, by applying minor changes to the current code, new GEE web applications can be implemented to address similar problems (Genzano et al., 2020).

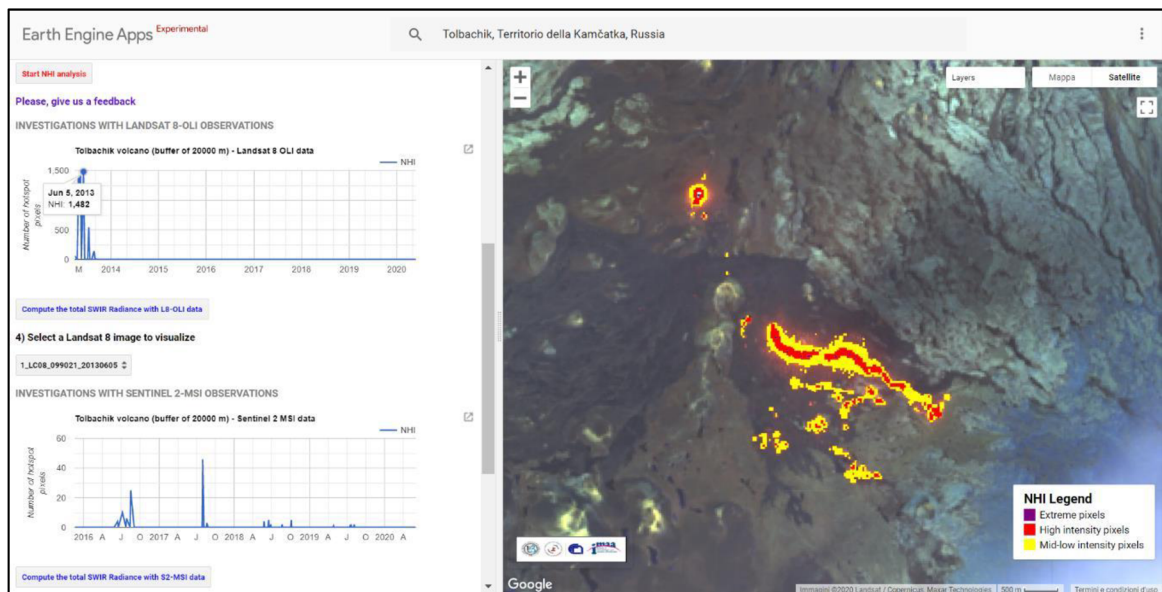


Figure 9 The thermal activity of the Tolbachik volcano in Russia, monitored by the Normalized Hot Spot Indices GEE tool (Genzano et al., 2020).

The GEE platform can be challenging to users unfamiliar with remote sensing and programming languages, limiting its reach to wider audiences, and motivating the users to continue using traditional processing and visualization methods for EO data. However, the design and development of GEE web applications with a user-friendly GUI, interactive widgets such as buttons, labels, and charts, and dynamic operations improve the accessibility to scientific analyses for specialists and the non-scientific community, converting the GEE web applications into a novel in remote sensing. There are still some limitations that restrict the scale of the analyses and applications, which include a maximum of 32 MB for external user downloads, or 400 km² using a 10 m pixel size with Sentinel-2 (Scheip & Wegmann, 2021), a maximum number of pixels of 10 million for each process (Zhang et al., 2020) and reduce numbers of simultaneous requests per user and duration of them (Genzano et al., 2020). With all of this, GEE and GEE web applications are powerful tools that will drive future analyses for hazard management, environmental resources, glacier monitoring, and more.

3D Web Mapping and CesiumJS Apps

Over the last decades, the availability and consumption of geospatial information have increased tremendously, leading to the development of GIS software to access, manage, and perform analyses (Potnis & Durbha, 2016; Scianna & La Guardia, 2018). Additionally, visualization techniques have been created to present geospatial data in a way that can be explored, a concept known as geovisualization (Schanche, 2020). Visualizing scientific information, including geospatial data, is essential as it can improve people's understanding of a complex phenomenon by communicating and presenting it more straightforwardly and attractively (Flückiger, 2022). In this context, associated with the significant improvement of computer graphics (Schanche, 2020) and the development of WebGL technologies (Mete et al., 2018), there is an ongoing discussion on the current necessity of transitioning from 2D to 3D visualization, using web applications instead of traditional desktop software (Jedlička & Hájek, 2020; Shivam & Narayan, 2023). This scenario has motivated the creation of several JS libraries, such as ThreeJS, and CesiumJS, for creating 3D visualization products.

Historically, geospatial data has been visualized and represented within GIS desktop software using a 2D map visualization in various fields, including urban planning, agriculture, and environmental management (Shivam & Narayan, 2023). However, 2D perspectives cannot accurately represent 3D characteristics such as scale and elevation due to the lack of depth perception. This limits the data analysis possibilities and the understanding of spatial relationships (Shivam & Narayan, 2023). In contrast, 3D has been demonstrated to improve data readability, visualization, and comparison by enabling access to the Z-axis (He et al., 2016), which is crucial for altitude-dependent data such as air pressure or wind speed (Potnis & Durbha, 2016). Moreover, 3D visualization has added value compared to 2D visualization as it can represent real-world locations in a more realistic and detailed way, which helps to better understand natural phenomena like floods in less time (Leskens et al., 2017). Even though the 3D perspective provides tangible advantages, it is necessary to evaluate which tasks benefit from it, as it requires the consideration of new design aspects (e.g., perspective, camera settings, graphical map load) compared with traditional 2D approaches (Hajek et al., 2016; Hajerk et al., 2018).

The capability of visualizing 3D content on a web browser started in 2012 with the launch of WebGL (Parisi, 2012). It is an open web standard JS Application Programming Interface (API) used to render 3D content within HTML that extends the traditional web pages' client-side components (Figure 10) and functionalities (Farkas, 2017; Parisi, 2012). Recently, it has gained such popularity that it is supported in most web browsers and is constantly updated (Kang et al., 2018). With WebGL, new geospatial standards to share and access data online, and the increasing capabilities of web browsers (Farkas, 2017), visualization of 3D geospatial data on the web has been possible (La Guardia et al., 2022). As a result, 3D Web GIS, which is characterized by its flexibility, expansibility, and the lack of need for installing software, has been popularized (Kang et al., 2018; Mete et al., 2018) through the development of JS libraries and 3D web applications that can be accessed at any time (Mete et al., 2018; Qu et al., 2023).

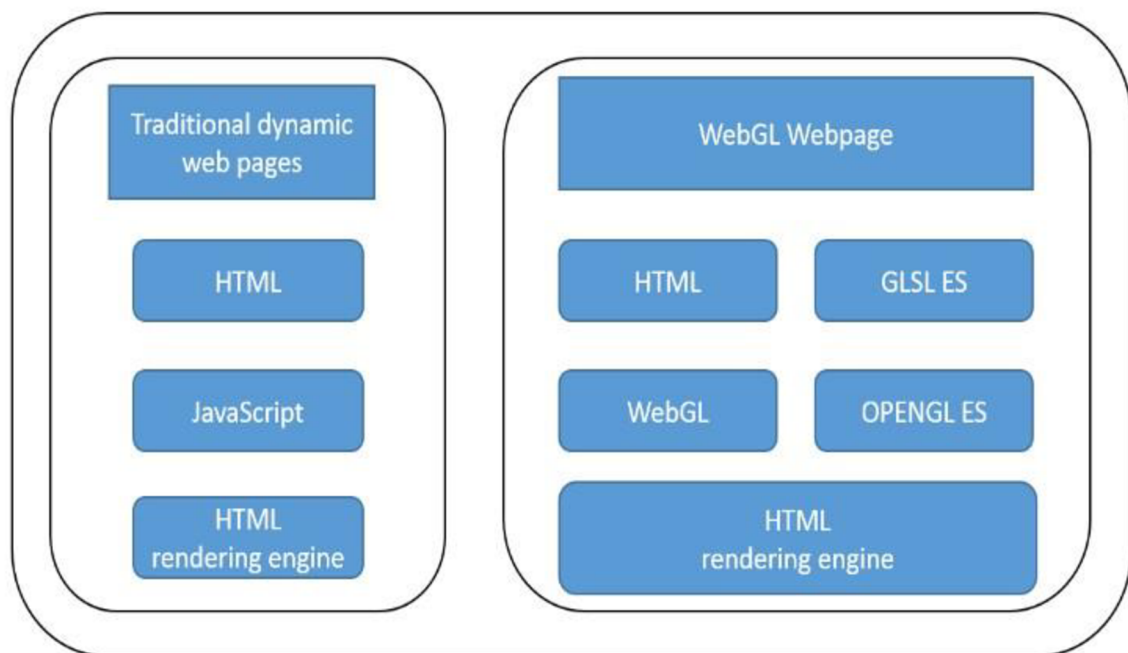


Figure 10 Comparison between components of traditional web pages with WebGL implementation (Kang et al., 2018).

Some of the current JS libraries used for rendering 3D graphics are WebGL Earth, ArcGIS API for JavaScript, Tangra, OSM Buildings GL, ThreeJS, and CesiumJS (Gede, 2018; Mete et al., 2018). Of these JS libraries, CesiumJS has become one of the most important since the deprecation and retirement of the Google Earth plugin in 2016 (Gede, 2018; Zhang et al., 2021). CesiumJS is defined as a JS open-source library that allows the creation of 2D and 3D scenes in web browsers (He et al., 2016), characterized by its lightweight, cross-platform, and extensive capabilities, along with constant support by the community and detailed documentation (Schanche, 2020; Zhang et al., 2021). The main advantages of CesiumJS over other JS libraries are its capability to interact with 3D entities with just one click, its ability to display information through popups, zoom, and pan around these, and the availability of a timeline feature to visualize real-time animations or entity changes over time (Potnis & Durbha, 2016). In consequence, even though CesiumJS has the steepest learning curve (Farkas, 2017), it is the main JS library when creating 3D web applications for visualizing data such as temperature, air pressure, or wind speed (Potnis & Durbha, 2016).

For example, Mete et al. (2018) developed a 3D CesiumJS web application to render vector data with global, country, and city-scale population and income attributes in the virtual globe (Figure 11). With this application, the authors demonstrated the capabilities of CesiumJS to retrieve, query, and visualize GeoJSON data format fluently in 3D, entirely in a web environment, without installing any plugin.



Figure 11 Turkey's population by province in 2010, visualized in 3D with CesiumJS (Mete et al., 2018)

Cho et al. (2023) also created a 3D web application (Figure 12) using CesiumJS for visualizing agricultural data and 3D models of agricultural infrastructure such as irrigation systems, culverts, and drainage facilities. This was possible by combining BIM concepts, aerial imagery collected with a drone, and the capabilities of Cesium JS to create digital twins (Cho et al., 2023). The result is an interactive web application that provides farmers with real-time information on irrigation and drainage flow rates and allows the assessment of current agricultural infrastructure in a virtual environment (Cho et al., 2023). Tools like this empower farmers and whole communities to become important decision-makers as they have access to data in a simple and user-friendly way.

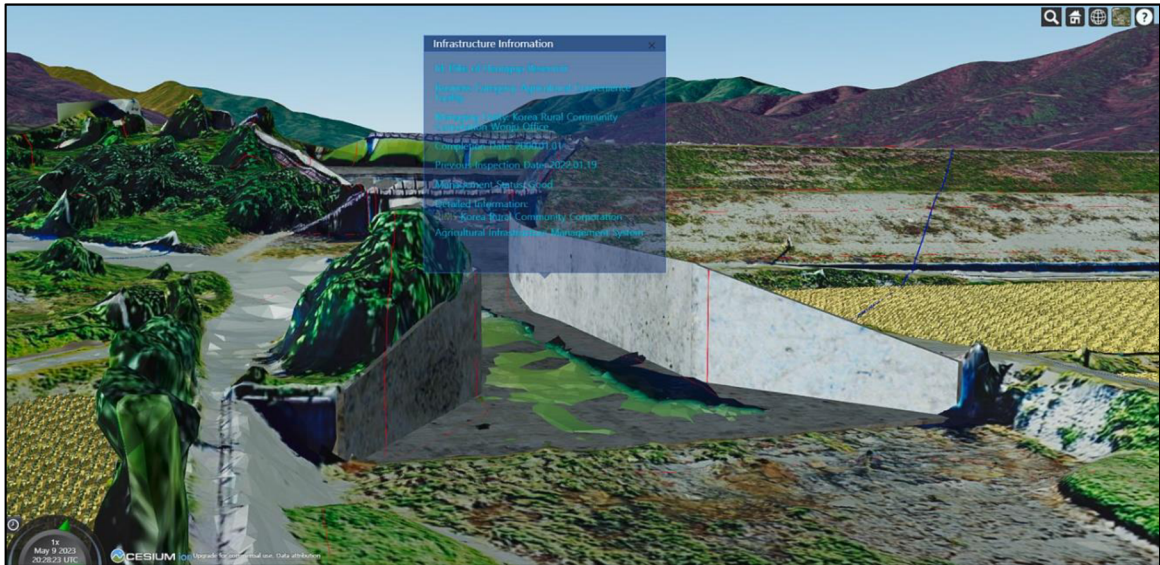


Figure 12 3D visualization of a channel and its attributes (Cho et al., 2023).

Regarding temperature data and visualization, Wang et al. (2017) developed the “PolarGlobe” web application (Figure 13) that allows the visualization in 3D of climate data such as air temperature. The application aims to reduce the learning curve of other climate simulation software by providing a GUI that allows users to filter, interact and create vertical profiles for temperature data (Wang et al., 2017).

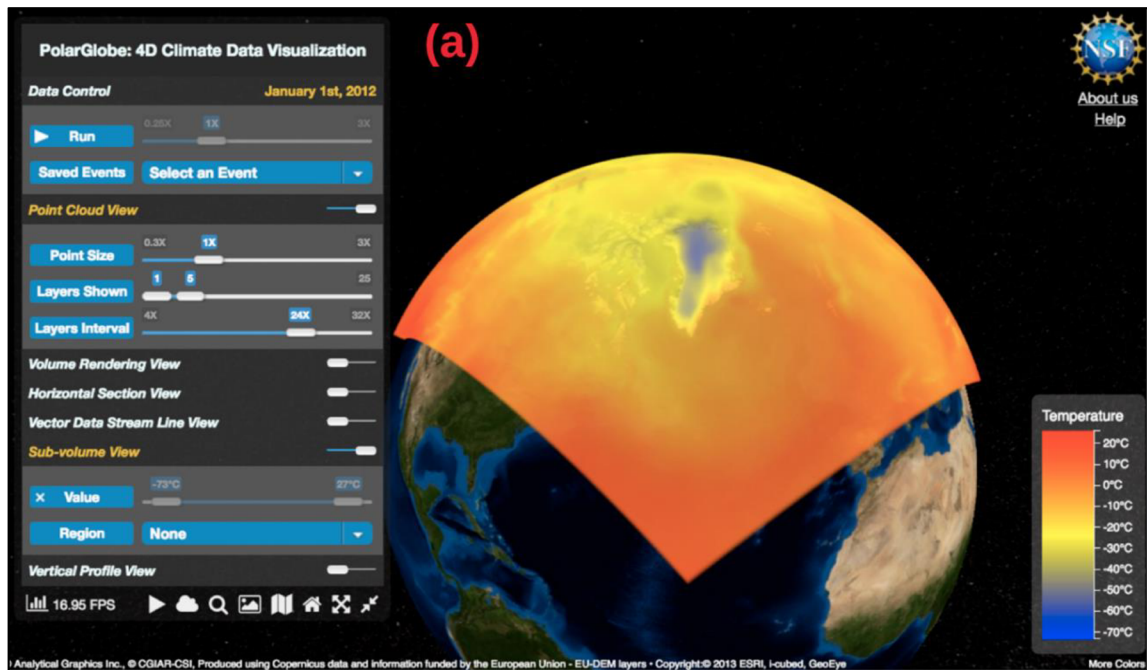


Figure 13 PolarGlobe 3D Cesium web application GUI (Wang et al., 2017).

In this chapter, it was reviewed and discussed the most recent glacier studies carried out in the Patagonian region using EO data, along with the implementation and advantages of the GEE cloud computing platform for glacier research. Moreover, the GEE Apps and CesiumJS API were introduced as trending tools for creating interactive and user-friendly 2D and 3D web products in the last few years. Finally, several examples demonstrated their capabilities and scientific applications.

3 METHODOLOGY

This chapter introduces the study area, the selection criteria, and the data used in this thesis, including satellite imagery, terrain, and vector data. Moreover, it defines the software, remote sensing indexes, and statistical validation methods employed. Finally, it briefly describes the implemented workflow, emphasizing the data acquisition, processing, analysis, and creation of web applications.

3.1 Study Area

The study area for this research is the Patagonian Andes, considered the largest glacierized area in South America, with a total glacier extent of 20000 km², spread over 46°S and 52°S latitudes (Carrasco-Escaff et al., 2023). Specifically, this research focuses on the NPI and SPI (Figure 14), where most glaciers are concentrated, with an extent of 4200 km² and 13000 km², respectively (Pelliccioti et al., 2014). For these icefields, based on the RGI 7.0 inventory, glaciers with an area greater or equal to 10 km² were filtered and selected, resulting in 27 NPI and 56 SPI glaciers.

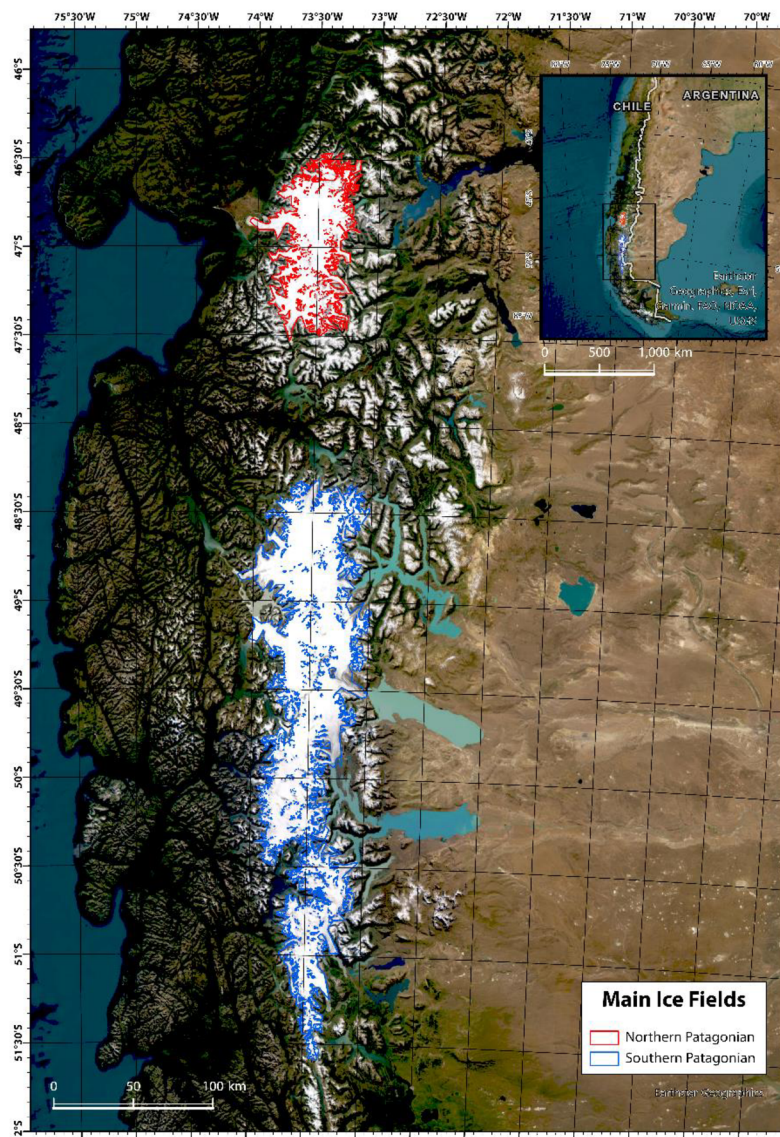


Figure 14 Map with the Location of the NPI and SPI study areas, Projection: WGS 1984 UTM Zone 18S.

For the NPI, the biggest glaciers selected were “San Quintin” (Figure 15A) and San Rafael, with areas of 815.29 km² and 684.55 km², respectively. Meanwhile, for the SPI, the largest were “PIO XI” and “Viedma” (Figure 15B), with extents of 1233.08 km² and 896.36 km². Regarding the glaciers' median height, it goes from 690 m to 2040 m. The NPI and SPI are constituted mainly by calving glaciers that terminate into fjords or lakes (Aniya et al., 1997), which are sensitive to temperature, wind speed, precipitation, and altitude variations. Consequently, climatic changes have a direct impact on their area, volume, and glaciological processes (Carrasco-Escaff et al., 2023; Florath et al., 2021; Sáez et al., 2019). In the last few years, NPI and SPI glaciers have been experiencing a dramatic glacier retreat, area, and volume loss due to climate variability (Bates, 2020), leading to increased scientific studies that aim to understand their status and ongoing climatic dynamics. However, glaciers in NPI and SPI react differently to the same climate perturbation (Rivera et al., 2012; Sagredo & Lowell, 2021), which makes it difficult to develop regional studies.

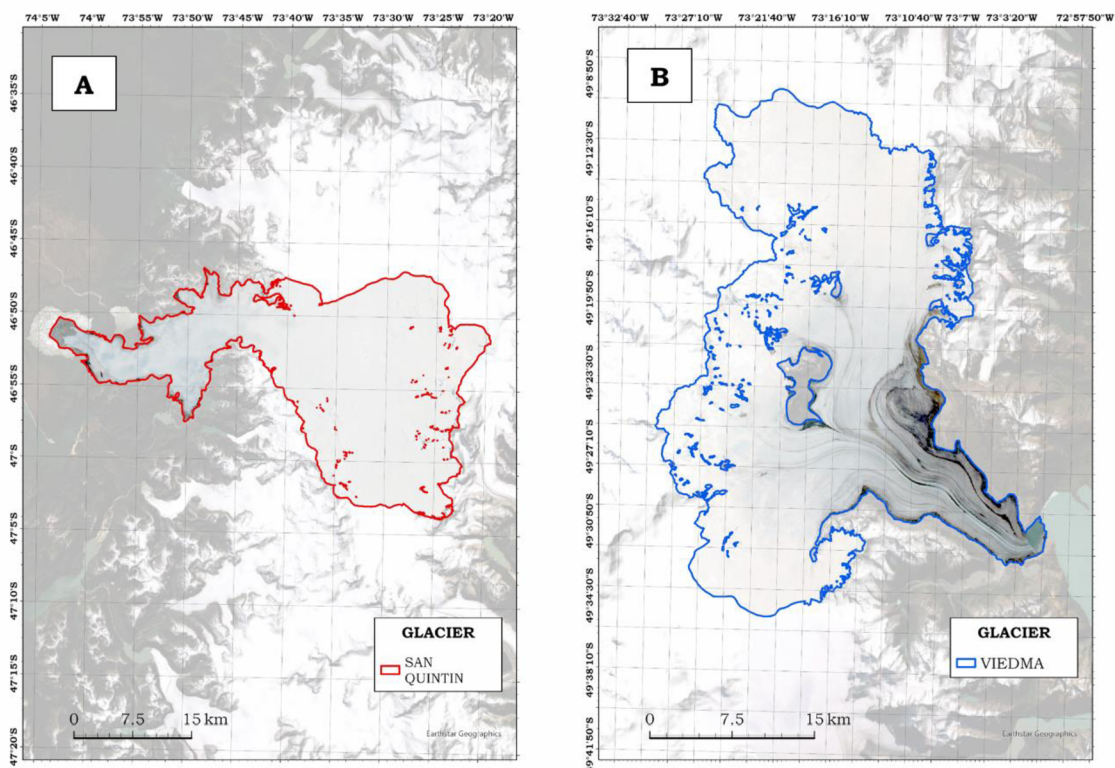


Figure 15 A) Map for San Quintin Glacier, Projection: WGS 1984 UTM Zone 18S, Scale: 1:350,000; B) Map for Viedma Glacier, Projection: WGS 1984 UTM Zone 18S, Scale: 1:250,000.

3.2 Data

This thesis used several data (types and sources) for different purposes. In GEE, Optical Satellite Data, including Sentinel-2, Landsat 8-9 imagery, and ERA5-Land Monthly Aggregated dataset, was retrieved and used to conduct a time-series analysis and generate EO outputs. Additionally, Bing imagery was implemented as a base map for the 3D web application. The Cesium World Terrain was selected for terrain data, and vector data with the NPI and SPI glaciers footprints were collected from the RGI 7.0 database.

3.2.1 Optical Satellite Data

The satellite data introduced in this section was acquired through the GEE API, except for the Bing Maps Aerial Imagery. Sentinel-2, Landsat 8-9, and ERA5-Land Monthly Aggregated imagery were collected for the period between 01. 10. 2018 and 03. 31. 2023, the Patagonian summer (Carrasco-Escaff et al., 2023). Sentinel-2 and Landsat 8-9 were used for time-series analysis and estimation of glacier area changes. Moreover, with Landsat 8-9 and ERA5-Land Monthly Aggregated imagery, temperature time-series analyses were carried out, specifically for LST and air temperature, respectively.

Sentinel-2 mission is part of the European Commission’s Copernicus programme, in charge of monitoring climate change impacts on the Earth. It started in 2015 and consists of a two-satellite constellation with a wide-swath high-resolution multispectral imager with 13 spectral bands and a combined revisit time of 5 days that provide high-resolution optical imagery for monitoring agriculture, forests, water, and land cover changes (European Space Agency, n.d). In GEE, six spectral bands (Table 1) of Sentinel-2 imagery were accessed through the Image Collection: “COPERNICUS/S2_SR_HARMONIZED”.

Table 1 Sentinel-2 selected spectral bands.

Band Name	Pixel Size (m)	Central Wavelength (nm)
B2 (blue)	10	490
B3 (green)	10	560
B4 (red)	10	665
B8 (NIR)	10	842
B11 (SWIR 1)	20	1610
Scene Classification Layer (SCL)	20	N/A

Landsat 8 is part of the historical Landsat programme developed by the National Aeronautics and Space Administration (NASA) and the United States Geological Survey (USGS). This satellite was launched on February 11, 2013, to collect multispectral images of the global land mass. It delivers imagery on a revisit time of 16 days and with resolutions from 15 m to 100 m (NASA, n.d). In GEE, Landsat 8 imagery was retrieved from the definition of a custom Image Collection with LST values based on the Ermida et al. (2020) algorithm. Table 2 present in detail the chosen bands.

Table 2 Landsat 8-9 selected spectral bands.

Band Name	Pixel Size (m)	Central Wavelength (nm)
SR_B2 (blue)	30	482
SR_B3 (green)	30	562
SR_B4 (red)	30	655
SR_B5 (NIR)	30	865
SR_B6 (SWIR 1)	30	1610
LST	30	N/A

Landsat 9 is the most recent Landsat mission, launched on September 27, 2021, as a collaboration between NASA and USGS. The spectral (Table 2) and temporal resolutions of the Landsat 9 satellite are similar to those of the Landsat 8 mission. However, it has a higher radiometric resolution, which provides more accurate surface temperature measurements and enhances atmospheric corrections (USGS, n.d). As for Landsat 8, Landsat 9 imagery with the LST custom band was retrieved in GEE based on the Ermida et al. (2020) algorithm.

ERA5-Land is a reanalysis dataset that combines the HTESSEL surface model with observations from various sources to create a global dataset with climate variables such as air temperature, precipitation, pressure, and runoff. The data is available from 1950 with a minimum spatial resolution of ~9km (ECMWF, n.d; Google, n.d). In GEE, the ERA5-Land Monthly Aggregated Dataset imagery, specifically the “temperature_2m” band, was accessed through the “ECMWF/ERA5_LAND/MONTHLY_AGGR” Image Collection. This band provides air temperature measured at 2m above the surface.

Bing Maps Aerial Imagery with pixel resolutions from 15 cm to 30 cm (Cesium, n.d), hosted in the Cesium ion’s cloud architecture, was selected as the basemap for the 3D CesiumJS web application.

3.2.2 Terrain Data

High-resolution global 3D terrain from Cesium was implemented in the 3D web application. It combines different data sources into a single terrain tileset designed for efficient 3D visualization, with a spatial resolution for the Patagonian region between 30 m and 90 m (Cesium, n.d).

3.2.3 Vector Data

The RGI is a global inventory of glacier outlines derived from the GLIMS multi-temporal database, developed in 2010 by glaciologists worldwide, that aims to provide a snapshot of the world’s glaciers as close to the year 2000. RGI is not designed to be an accurate source of measurements of glacier areas. However, the glacier outlines that it delivers can be used as AOIs or delimitation areas for scientific analyses (MauSSION et al., 2023), which is the case of this thesis. In this research, from the RGI 7.0, released on September 2023, the outlines for the total (83) NPI and SPI glaciers were extracted from the global dataset downloaded as shapefile format, with attributes such as glacier name, area, year of measurement, and median elevation. These outlines were used to filter the study glaciers, to clip the described optical satellite imagery in GEE for every selected glacier, and to filter the data to be visualized in the CesiumJS application.

3.3 Software

GEE is a cloud computing platform that gives access to a multi-petabyte catalog of satellite imagery and planetary-scale analysis capabilities. Researchers use it to map trends, detect changes, and perform time-series analyses on the Earth’s surface without downloading any data locally. This thesis used the JS API **v0.1.395** through the GEE Code Editor to perform time-series analyses for glacier area and temperature changes and create the GUI of the GEE web application.

ArcGIS Pro is a desktop GIS application developed by Esri that allows users to explore, visualize, and analyze geospatial information in 2D and 3D and create cartographic products. In this study, ArcGIS Pro **3.1.3** was used to filter and export the RGI 7.0 glacier outlines and process the GEE composites exported from the GEE

application before being uploaded into the Cesium ion cloud platform. Additionally, it was used to create the maps included in this research.

CesiumJS is an open-source JS library used by different industries to create interactive 3D globes and maps that can be shared on the web. It is characterized by outstanding performance, precision, visual quality, and ease of use. CesiumJS **1.116**, along with HTML and Cascading Style Sheets (CSS), was used to create the 3D web application.

Cesium ion is a robust cloud platform for hosting 3D geospatial data. It provides access to global 3D content and the possibility to upload custom 3D models, terrain, and imagery. It was used as the hosting and streaming platform for the EO outputs from GEE to be added to the CesiumJS 3D web application.

ArcGIS Survey123 is a form-centric solution developed by Esri to create forms that allow data collection and posterior analysis. In this research, it was utilized to gather feedback from users about the GEE and 3D web applications.

GitHub is a developer platform for sharing code and contributing to open-source projects. Furthermore, it provides hosting services for various data types and web pages. In this thesis, GitHub served as the hosting platform for both the time-series chart outputs generated by the GEE application and the web page of the 3D web application.

Visual Studio Code is a standalone source code editor that supports developer tooling, such as debugging, task running, and version control. Visual Studio Code version **1.87.2** was used to coding the 3D CesiumJS web application code.

Microsoft Excel is a spreadsheet editor for data visualization and analysis. It was used to enhance the GEE time-series charts by plotting trend lines and calculating RMSD and RRMSD.

3.4 Remote Sensing Indices

The NDSI and NDWI were calculated in GEE to identify and quantify glacier areas and mask glacier lakes.

3.4.1 NDSI

The NDSI (1) was coined by Hall et al. (1995). It is used for mapping snow cover based on the ratio of the green and Short-Wave Infrared (SWIR) channels. Additionally, considering snow is highly reflective and absorptive in the NIR and SWIR part of the spectrum, NDSI can distinguish between clouds and snow (Kääb, 2011). It is defined as:

$$NDSI = \frac{GREEN - SWIR1}{GREEN + SWIR1} \quad (1)$$

3.4.2 NDWI

The NDWI (2), developed by McFeeters (1996), takes advantage of the high reflectance of water features in the green wavelength and the low reflectance in NIR wavelength to efficiently delineate open water features, removing soil and terrestrial vegetation features (McFeeters, 1996). It is defined as:

$$NDWI = \frac{GREEN - NIR}{GREEN + NIR} \quad (2)$$

3.5 Statistical Errors

Even though for this thesis, a detailed accuracy assessment was not carried out, for estimating the rate of change of glacier area, LST, and air temperature over time, a linear relationship was fitted to the summer values, and RMSD and RRMSD were used as accuracy measurements for the observed trends.

3.5.1 RMSD

RMSD (3) is an absolute error measure used in time series analysis for model validation and fitting (Karunasingha, 2022). It is defined as:

$$RMSD = \sqrt{\frac{\sum_{i=1}^n (x_i - \bar{x}_i)^2}{N}} \quad (3)$$

where the actual value is x_i , the linear regression value is \bar{x}_i and N is the total number of measurements. The RMSD was used in this thesis as an error measurement for LST and air temperature rate of change linear relationships.

3.5.2 RRMSD

RRMSD (4) is calculated by dividing RMSD by the average value of x_i , the linear regression values (Despotovic et al., 2016). In this research, it was used particularly as a statistical measurement for the linear regression fitted to the glacier area values to provide more insight into the magnitude of the error compared to the corresponding glacier area.

$$RRMSD = \left| \frac{RMSD}{Average(\bar{x}_i)} * 100 \right| \quad (4)$$

3.6 General Procedure

The workflow developed in this thesis (Figure 16) starts with retrieving the NPI and SPI glacier outlines from RGI 7.0. The data was filtered and exported as shapefiles using ArcGIS Pro. Then, in GEE, the feature collection for the glacier outlines, and the image collections for Landsat 8,9, Sentinel-2, and ERA5-Land imagery were created. Furthermore, inspired by Zhang et al. (2021), Turpo Cayo et al. (2022), and Arif et al. (2021) methodologies, glacier area estimations, median temperature composites, and time series charts for each summer period were generated by the combination of several processing functions. After the time series analysis, a GUI was designed and launched with three principal panels (Main, Map, and Charts) and different widgets. With this GEE web application, the summer median temperature composites and glacier area delimitation images were exported in TIFF format. Then, in ArcGIS Pro, the images were processed to have comparable symbology and be uploaded to Cesium ion. The Comma-separated Values (CSV) files exported from the GEE application were used to create line charts within Microsoft Excel by fitting a linear regression to the values, estimating R^2 , RMSD, and RRMSD, and then uploading them to GitHub. With the required data hosted in the cloud, the 3D CesiumJS web application was developed using Visual Studio Code. Finally, user evaluation for both web applications was performed by collecting feedback from an online ArcGIS Survey123 form.

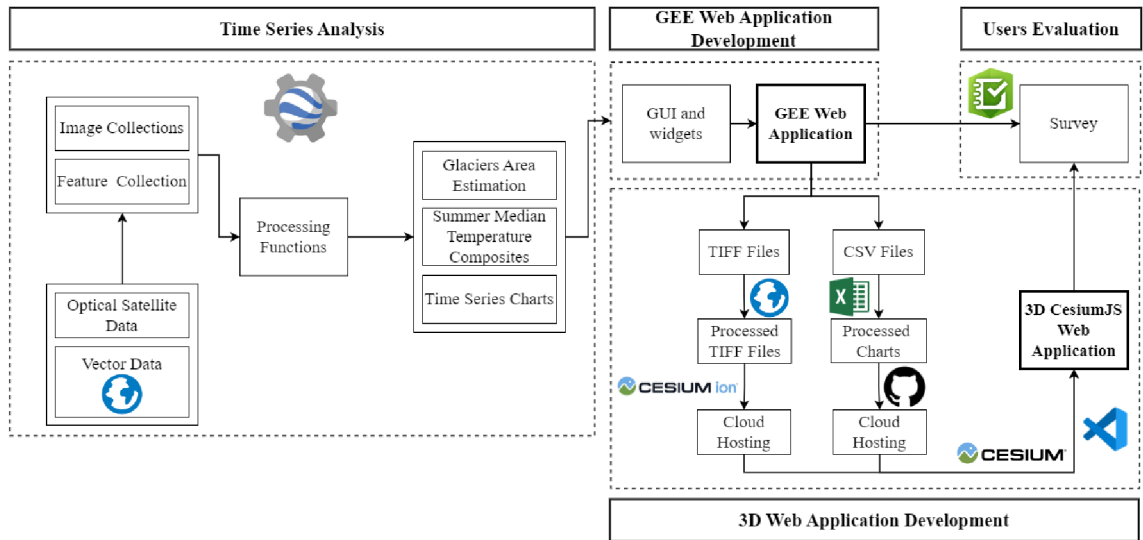


Figure 16 Thesis Workflow Overview.

4 TIME-SERIES ANALYSIS

This chapter presents the methodology, detailed steps, and code implementation for the Time-Series analysis of NPI and SPI glaciers area and temperature changes within the GEE platform. As observed in Figure 17, the workflow is constituted by the definition of required features and image collections based on the summer period and cloud cover percentages. Moreover, functions such as temperature conversion, image clipping, band renaming, spectral indices, and glacier area calculations were created and implemented. Furthermore, iterative processes were developed to create median composites and include them as images in new image collections. As a result, temperature summer median composites, glacier area delineation, and the corresponding time-series charts were generated. The complete GEE code implementation can be accessed at <https://code.earthengine.google.com/10c459a1dbd9e00b364bcc9278d43fe9>.

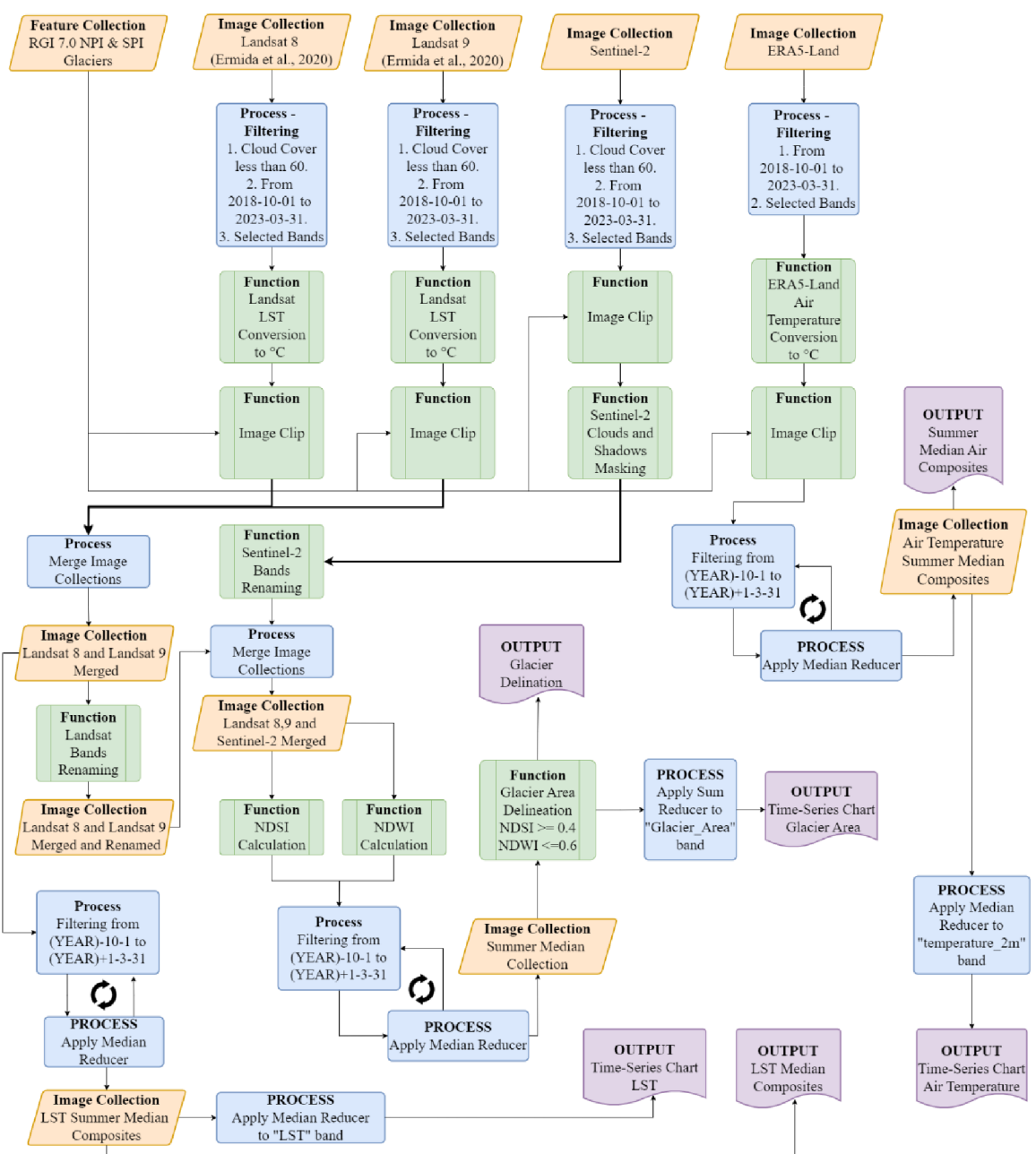


Figure 17 Time-Series Analysis workflow in GEE.

4.1 Initial Feature and Image Collections

Feature collections store related features with their geometries and attributes, while Image collections store a set of images. In GEE, it is possible to work with existing features and image collections or create new ones using custom vector and optical imagery previously uploaded.

For this time-series analysis, a **Feature Collection** containing NPI and SPI glaciers with an area greater than 10 km² was created from shapefiles exported in ArcGIS Pro based on the RGI 7.0 (Figure 18). This was used mainly as the clipping AOI for the Image Collections, functions, and processes that required the AOI as a parameter.

```
var glaciers_list = ee.FeatureCollection("users/Big_Earth_Course/RGI_NPI_SPI_GLACIERS_AOI");
```

Figure 18 GEE Code – Creation of the NPI and SPI glaciers Feature Collection.

In the case of the **Image Collections** for **Landsat 8** and **Landsat 9**, the first step was to import the LST JavaScript module developed by Ermida et al. (2020) and define the initial parameters (Figure 19), including satellite, initial, and final date. Then, both Image Collections were constructed using the *collection()* method of the LST JavaScript module. Furthermore, filtering methods were used to retrieve satellite images with a cloud cover of less than 60% within the AOI selected by the user from the Feature Collection, along with the required spectral bands (Figure 20).

```
var Landsat9_with_LST = require('users/sofiaermida/landsat_smw_lst:modules/Landsat_LST.js');
var satellite2 = 'L9';
var date_start2 = '2021-10-31';
var date_end2 = "2023-03-31";
var use_ndvi2 = true;
```

Figure 19 GEE Code – Import of the LST JavaScript Module and definition of creation parameters.

```
var landsat9_collection = Landsat9_with_LST.collection(satellite2,
  date_start, date_end, selectedGlacier, use_ndvi)
  .filterMetadata('CLOUDY_PIXEL_PERCENTAGE', 'less_than', 60)
  .filterBounds(selectedGlacier)
  .select(["SR_B2", "SR_B3", "SR_B4", "SR_B5", "SR_B6", "LST"])
```

Figure 20 GEE Code – Image Collection definition for Landsat 9.

For **Sentinel-2**, the **Image Collection** was defined similarly to the Landsat 8-9 process but without requiring the import of an external JavaScript module. Instead, it was defined from the existing “COPERNICUS/S2_SR_HARMONIZED” GEE asset with filtering methods, including bounds, date, cloud cover percentage, and spectral bands (Figure 21). It must be mentioned that the “selectedGlacier” parameter used in the *filterBounds()* GEE method, applied in the definition of all the Image Collections, corresponds to the user’s glacier selection from the Feature Collection through a select widget in the GEE web application.

```
var sentinel2_collection = ee.ImageCollection("COPERNICUS/S2_SR_HARMONIZED")
  .filterBounds(selectedGlacier)
  .filterDate("2018-10-01", "2023-03-31")
  .filterMetadata("CLOUDY_PIXEL_PERCENTAGE", "less_than", 60)
  .select(["B2", "B3", "B4", "B8", "B11", "SCL"])
```

Figure 21 GEE Code – Image Collection definition for Sentinel-2.

Finally, the definition of the **Image Collection** for the **ERA5-Land** involved the filtering of the existing GEE asset “ECMWF/ERA5_LAND/MONTHLY_AGGR” based on the study period and the selection of the “temperature_2m” spectral band (Figure 22).

```
var ERA5dataset = ee.ImageCollection('ECMWF/ERA5_LAND/MONTHLY_AGGR')
  .filterDate("2018-10-01", "2023-03-31")
  .filterBounds(selectedGlacier)
  .select("temperature_2m")
```

Figure 22 GEE Code – Image Collection definition for ERA5-Land dataset.

4.2 Functions

Since Image collections comprise multiple images from various sources, functional programming techniques are necessary to perform operations on each image within the collections. In this context, JS functions were developed and used for multiple purposes, such as masking clouds and shadows, converting temperature units, renaming bands, and calculating spectral indices. After the functions were defined, they were applied to every image of the corresponding Image Collection using the *map()* GEE method.

4.2.1 Image Clipping

The *ImageClip()* function (Figure 23) was used to clip the images within an Image Collection to the Patagonian glacier selected by the end-user. Although this function is simple, it plays a crucial role as it ensures that only the required area is considered for processing. This reduces the need for computational resources as it performs the glacier area and temperature calculations only for the selected glacier.

```
var ImageClip = function(img){
  return img.clip(selectedGlacier);
}
```

Figure 23. GEE Code – Image Clipping Function.

4.2.2 Temperature Conversion

Landsat and ERA5-Land temperature values are in Kelvin. However, to ensure consistency with the units used in South America, where Patagonia is located, and with the units commonly employed in temperature analyses, two functions were created to convert the temperature to Celsius (Figure 24 & Figure 25).

```
var Celsius = function(image) {
  var KtoC = image.select('LST').add(-273.15);
  return image.addBands(KtoC, null, true);
};
```

Figure 24 GEE Code – Function to convert LST for all the images within the Landsat Image Collections to Celsius.

```
var Celsius_ERA5 = function(image) {
  var KtoC = image.select('temperature_2m').add(-273.15);
  return image.addBands(KtoC, null, true);
};
```

Figure 25 GEE Code – Function to convert the air temperature for all the images within the ERA5-Land Image Collection to Celsius.

4.2.3 Clouds and Shadows Masking

To mitigate the influence of clouds and shadow pixels in the time-series analyses and the summer median composites, the *sentinel2_clouds_shadows_masking()* function was applied to images within the Sentinel-2 Image collection. This function identified and masked out cloud and shadow pixels using the SCL. Within this layer, pixels identified as high-probability clouds and cloud shadows were combined into a single mask. Subsequently, the *eq(0)* method was employed to assign a value of 1 (TRUE) to non-clouds or non-shadow pixels, while cloud and shadow pixels were assigned a value of 0 (FALSE). Finally, the *updateMask()* method removed pixels marked as 0, corresponding to clouds and shadows (Figure 26). Regarding clouds and shadow masking for Landsat Image Collections, it was not implemented, as the Ermida et al. (2020) algorithm masked clouds and shadows before the LST calculations.

```
var sentinel2_clouds_shadows_masking = function(img) {  
  var scl = img.select('SCL');  
  var cloud_high = scl.eq(9);  
  var cloud_shadow = scl.eq(3);  
  var cloud_mask = cloud_high.add(cloud_shadow);  
  var cloud_uni = cloud_mask.eq(0).selfMask();  
  var cloud_masked = img.updateMask(cloud_uni);  
  return cloud_masked;  
}
```

Figure 26 GEE Code – Clouds and Shadows masking function for Sentinel-2 Image Collection.

4.2.4 Spectral Bands Renaming

The *sentinel2_bands_renaming()* and *landsat_bands_renaming()* functions (Figure 27 & Figure 28) were developed to standardize the naming conventions for the optical, NIR, and SWIR1 spectral bands across Sentinel-2 and Landsat Image Collections and to remove the LST band from the Landsat Image Collections. Specifically, for Sentinel-2 images, the spectral bands B2, B3, B4, B8, and B11 were renamed as BLUE, GREEN, RED, NIR, and SWIR1, respectively. For the Landsat images, the spectral bands SR_B2, SR_B3, SR_B4, SR_B5, and SR_B6 were correspondingly renamed as BLUE, GREEN, RED, NIR, AND SWIR1. This standardization was necessary to ensure that the calculation of the NDSI and NDWI for the Landsat 8, 9, and Sentinel-2 merged Image Collection was conducted using the same spectral bands, whether for a Sentinel-2 or Landsat image. Moreover, it allowed the visualization of a true color composite using the optical bands.

```
var sentinel2_bands_renaming = function(image) {  
  return image  
    .select(['B2', 'B3', 'B4', 'B8', 'B11']).rename(['BLUE', 'GREEN', 'RED', 'NIR', 'SWIR1'])  
    .toFloat();  
}
```

Figure 27 GEE Code – Renaming function for Sentinel-2 Image Collection spectral bands.

```
var landsat_bands_renaming = function(image) {  
  return image  
    .select(['SR_B2', 'SR_B3', 'SR_B4', 'SR_B5', 'SR_B6']).rename(['BLUE', 'GREEN', 'RED', 'NIR', 'SWIR1'])  
    .toFloat();  
};
```

Figure 28 GEE Code – Renaming function for Landsat Image Collections spectral bands.

4.2.5 Spectral Indices Calculation

For calculating the NDSI and NDWI indexes, the *ndsi_index()* and *ndwi_index()* functions were created (Figure 29 & Figure 30). Both used the *normalizedDifference()* method with the respective bands to calculate the index value. Furthermore, the *addBands()* method added the indices calculations as new bands to the corresponding image.

```
var ndsi_index = function(image) {
  var ndsi = image.normalizedDifference(["GREEN", "SWIR1"]);
  return image.addBands(ndsi.rename("NDSI"));
}
```

Figure 29 GEE Code – NDSI calculation function.

```
var ndwi_index = function(image) {
  var ndwi = image.normalizedDifference(["GREEN", "NIR"]);
  return image.addBands(ndwi.rename("NDWI"));
}
```

Figure 30 GEE Code – NDWI calculation function.

4.2.6 Glacier Area Delineation

According to Zhang et al. (2021), in areas with snow presence, pixels with $NDSI \geq 0.4$ and $NDWI \geq 0.2$ can be identified as glacier and water classes, correspondingly. Based on this, after testing different thresholds, pixels with $NDSI \geq 0.4$ and $NDWI \leq 0.6$ were chosen to define the glacier class, using the NDWI threshold to exclude water bodies such as glacier lakes. Consequently, the *Glacier_Area_Delineation()* function (Figure 31) was created to identify the glacier pixels and append their individual pixel area in km^2 as a new band to each summer median composite. First, the function generated a mask for glacier pixels based on the mentioned NDSI and NDWI thresholds. Then, for each pixel, it multiplied the mask value (1 for the glacier pixels and 0 for the non-glacier pixels) by the pixel area and divided it by 1000000 to convert m^2 into km^2 . The pixel area was calculated using the *ee.Image.pixelArea()* method, which employs an equal area map projection to ensure accurate measurements. As a result, in the new “Glacier_Area” band added to the summer median composites, pixels identified as glaciers were assigned a value corresponding to the pixel area in km^2 , while non-glacier pixels were assigned a value of 0.

```
var Glacier_Area_Delineation = function(image) {
  var GlacierPixel = image.select('NDSI').gte(0.4).and(image.select('NDWI').lte(0.6));
  var GlacierPixelArea = GlacierPixel.multiply(ee.Image.pixelArea()).divide(1000000);
  return image.addBands(GlacierPixelArea.rename('Glacier_Area'))
}
```

Figure 31 GEE Code – Glacier Area Delineation function for glacier pixel identification and area calculation.

4.3 Workflow and Processes

After defining the Feature and Image Collections, the JS functions were applied. This section will explain the additional processes and the sequence of the functions that allowed the creation of glacier area and temperature time-series outputs, including summer median composites and time-series charts.

4.3.1 Glacier Area Composites and Time-Series Chart

For the delineation of glacier areas and the creation of time-series charts, Landsat 8, 9, and Sentinel-2 Image Collections were utilized. Regarding Landsat 8 and 9, after defining and filtering both collections based on cloud cover percentage, dates, and the bands described in section 4.1, the *Celsius()* and *ImageClip()* functions were applied to each Image Collection. These functions converted the LST to Celsius and clipped the images to the glacier selected by the user. Subsequently, both Image Collections were merged to create the “landsat8_9_collection”, to which the *landsat_bands_renaming()* function was applied, resulting in an Image Collection with Landsat 8, 9 imagery and with the spectral bands renamed, called “landsat8_9_collection_Renamed”.

For the Sentinel-2 Image Collection, similar filtering was applied, followed by the *ImageClip()* function. Additionally, the *sentinel2_clouds_shadows_masking()* and *sentinel2_bands_renaming()* functions were implemented to remove clouds and shadow pixels and standardize the band names.

At this point, the “landsat8_9_collection_Renamed” and “sentinel2_collection” Image Collections were prepared for merging. Combining Landsat and Sentinel Imagery can be challenging due to the geographic misregistration caused by the different global reference systems and orientation measurements used (Xu et al., 2020). However, it has been observed that combining these datasets not only increases the number of observations but also provides more accurate classification results than working with both sensors separately (Xu et al., 2020). Considering this, both Image Collections were merged to create the “landsat8_9_and_sentinel2_collection” Image Collection. Then, the NDSI and NDWI were calculated for each pixel of the images within this Image collection using the *ndsi_index()* and *ndwi_index()* functions.

The next step was to create a new Image Collection (“SummerMedianCollection”), to store the summer median composites, and an iterative function (Figure 32). This function received by parameter the previously defined “startYear” (2018) and the “endYear” (2022) variables to iterate through each summer period between these years. For each year, the function defined a summer period from October 1st of the current year to March 31st of the following year and then filtered the “Landsat8_9_and_sentinel2_collection” Image collection for that period. Then, the *median()* function was used to create a summer median composite, representing the median NDSI and NDWI conditions during the summer period for each year. Subsequently, the resulting median composite was added to the “SummerMedianCollection” Image Collection, including, as a system property, the starting and ending year of the associated summer period.

```
var SummerMedianCollection = ee.ImageCollection([]);
for (var year = startYear; year <= endYear; year++) {
  var initial_date = ee.Date.fromYMD(year, 10, 1);
  var end_date = ee.Date.fromYMD(year + 1, 3, 31);
  var yearCollection = landsat8_9_and_sentinel2_collection.filterDate(initial_date, end_date);
  var MedianComposite = yearCollection.median();
  MedianComposite = MedianComposite.set('year', ee.Date(year.toString()).format("YYYY"));
  var nextYear = year + 1;
  var lastTwoDigits = ee.Number(nextYear).mod(100);
  MedianComposite = MedianComposite.set('year2', ee.Number(year).format("%d")
    .cat('/').cat(lastTwoDigits.format("%d")));
  SummerMedianCollection = SummerMedianCollection.merge(MedianComposite
    .set('system:time_start', ee.Date.fromYMD(year, 01, 01)));
}
SummerMedianCollection = SummerMedianCollection.map(Glacier_Area_Delineation);
```

Figure 32 GEE Code – Iterative function used to create the summer median composites.

As a result, five summer median composites, each corresponding to a summer period between 2018 and 2023, were created and added to the “SummerMedianCollection” Image Collection through the mentioned iterative function. For this Image Collection, the *Glacier_Area_Delineation()* function was applied to identify glacier pixels and assign the pixel area as glacier area. This allowed the visualization of glacier and non-glacier areas predominant during each summer and the creation of a time-series chart. The chart was generated by summing the “Glacier_Area” band for each summer median composite using the *ui.Chart.image.series()* and *ee.Reducer.sum()* methods, with a pixel size of 30 m (Figure 33).

```
var graphicGlacier = ui.Chart.image.series(SummerMedianCollection.select("Glacier_Area"),
selectedGlacier, ee.Reducer.sum(), 30, 'year2')
.setSeriesNames(['Area (km2)'])
.setChartType('ScatterChart')
.setOptions(Glacier_Area_option);
```

Figure 33 GEE Code – Code implementation for creating the time-series chart for the glacier area, using a pixel size of 30 m.

It is important to consider that despite the pixel size differences between the Sentinel-2 and Landsat bands used, in GEE, the scale of the analysis is determined by the outputs rather than the inputs (Google, n.d). Consequently, for this thesis, a pixel size of 30 m was selected as the resolution to create the time-series charts and to export the median composites through the GEE web application.

4.3.2 LST Composites and Time-Series Chart

The creation of LST summer median composites and the time-series chart involved merging Landsat 8 and Landsat 9 Image Collections after being filtered, clipped, and having converted the LST to Celsius, a process already followed to create the glacier area composites. However, an iterative function was implemented directly instead of applying the *landsat_bands_renaming()* function to the “landsat8_9_collection” Image Collection. This function was the same as the one implemented in the glacier area composites, with the only difference being that the “SummerLSTComposites” Image Collection was defined to store the LST summer median composites created by applying the *median()* method to the summer selection of the “landsat8_9_collection” Image Collection (Figure 34).

```
var SummerLSTComposites = ee.ImageCollection([]);
for (var year = startYear; year <= endYear; year++) {
  var initial_date = ee.Date.fromYMD(year, 10, 1);
  var end_date = ee.Date.fromYMD(year + 1, 3, 31);
  var yearCollection = landsat8_9_collection.filterDate(initial_date, end_date);
  var LSTComposite = yearCollection.median();
  LSTComposite = LSTComposite.set('year', ee.Date(year.toString()).format("YYYY"));
  var nextYear = year + 1;
  var lastTwoDigits = ee.Number(nextYear).mod(100);
  LSTComposite = LSTComposite.set('year2', ee.Number(year).format("%d")
.cat('/').cat(lastTwoDigits.format("%d")));
  SummerLSTComposites = SummerLSTComposites.merge(LSTComposite
.set('system:time_start', ee.Date.fromYMD(year, 01, 01)));
}
```

Figure 34 GEE Code – Iterative function for the creation of LST summer median composites.

With this function, the LST summer median composites were created and later visualized in the GEE web app. Moreover, the *ui.Chart.image.series()* method was applied with a pixel size of 30 m but using the *ee.Reducer.median()* method to create a time-series chart with the median LST value of each summer median composite (Figure 35).

```
var LST_GLOBAL_GRAPHIC = ui.Chart.image.series(SummerLSTComposites.select("LST"),
selectedGlacier, ee.Reducer.median(), 30, 'year2')
  .setSeriesNames(['Temperature (°C)'])
  .setChartType('ScatterChart')
```

Figure 35 GEE Code – Creation of the time-series chart for the LST, using a pixel size of 30 m.

4.3.3 Air Temperature Composites and Time-Series Chart

Using a similar procedure to the one performed in section 4.3.2, the air temperature summer median composites were created by applying an iterative function (Figure 36) to the filtered, clipped, and Celsius converted “ERA5dataset” Image Collection. In this case, the “SummerAIRComposites” Image collection was defined to store the median summer composites created from the *median()* method. The time-series chart was generated using the *ui.Chart.image.series()* and *ee.Reducer.median()* methods to retrieve the median value of the “temperature_2m” band for the pixels of each median composite, using the native resolution of ERA5-Land, which is 11132 m (Figure 37).

```
var SummerAIRComposites = ee.ImageCollection([]);
for (var year = startYear; year <= endYear; year++) {
  var initial_date = ee.Date.fromYMD(year, 10, 1);
  var end_date = ee.Date.fromYMD(year + 1, 3, 31);
  var yearchart = year + 1;
  var yearCollection = ERA5dataset.filterDate(initial_date, end_date);
  var AIRComposite = yearCollection.median();
  AIRComposite = AIRComposite.set('year', ee.Date(year.toString()).format("YYYY"));
  var nextYear = year + 1;
  var lastTwoDigits = ee.Number(nextYear).mod(100);
  AIRComposite = AIRComposite.set('year2', ee.Number(year).format("%d")
  .cat('/').cat(lastTwoDigits.format("%d")));
  SummerAIRComposites = SummerAIRComposites.merge(AIRComposite
  .set('system:time_start', ee.Date.fromYMD(year, 01, 01)));
}
```

Figure 36 GEE Code – Iterative function for the creation of Air Temperature summer median composites.

```
var AIR_TEMPERATURE_GRAPHIC = ui.Chart.image.series(SummerAIRComposites.select("temperature_2m")
selectedGlacier, ee.Reducer.median(), 11132, 'year2')
  .setSeriesNames(['Temperature (°C)'])
  .setChartType('ScatterChart')
```

Figure 37 GEE Code – Creation of the time-series chart for the Air Temperature, using a pixel size of 11132 m.

5 GEE WEB APPLICATION DEVELOPMENT

This section will describe the components (Figure 38) of the “Patagonian Glaciers Monitoring Application” GEE Web application, including the different widgets and elements used in the GUI design.

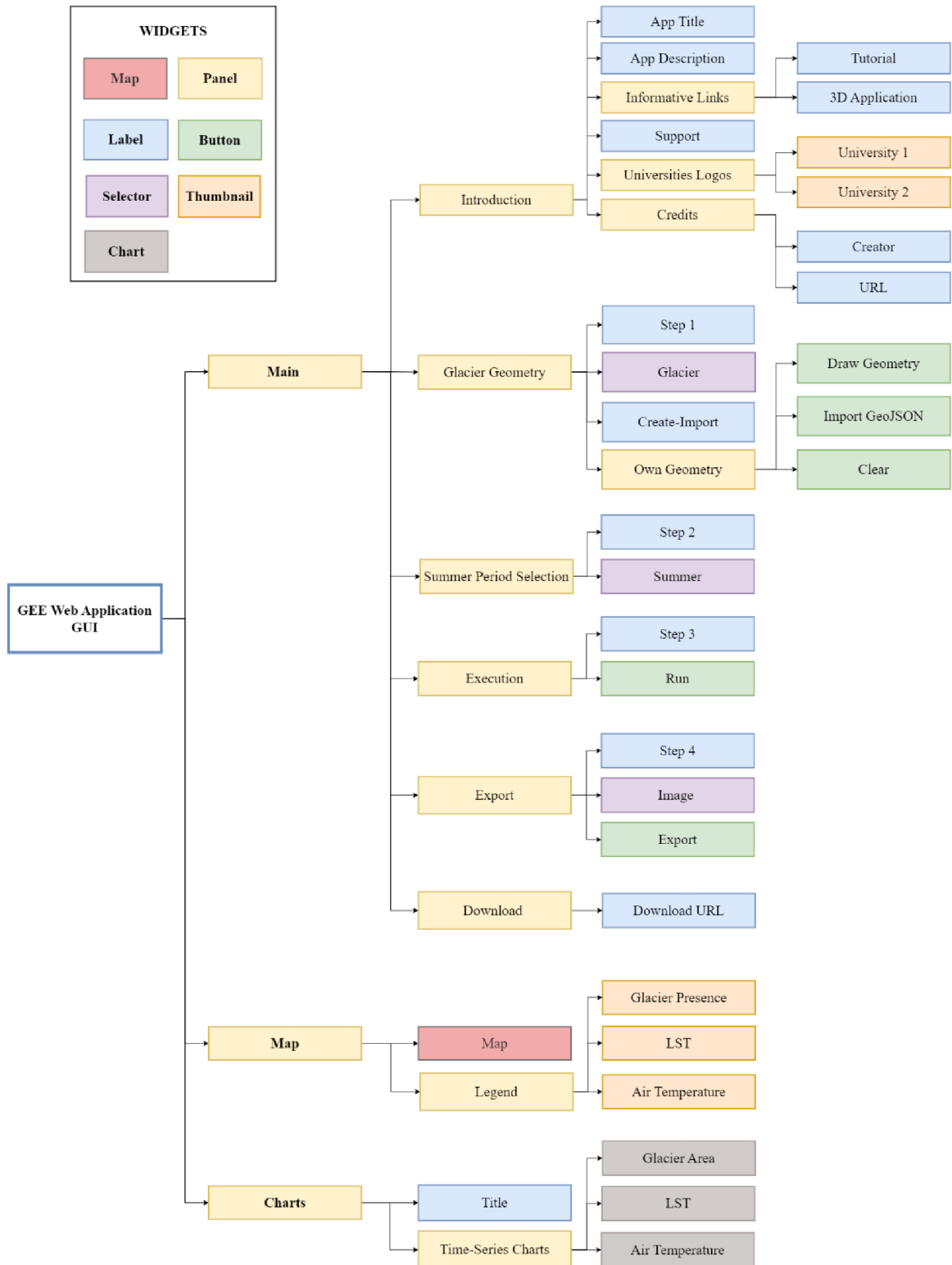


Figure 38 Schematic Representation of the GEE Web Application GUI.

GEE Web Applications are used to share interactive analyses through a powerful UI API that allows the creation of GUIs with panels and widgets such as labels, buttons, charts, and maps. Additionally, it can be combined with traditional CSS techniques to provide styling. These GUIs reduce the need for coding as users can analyze, visualize, and export EO data products directly in an interface. For this thesis, within the GEE code, three panel elements were defined using the *.ui.Panel()* constructor function as the principal containers of auxiliary UI panels and widgets (Figure 39). Each panel was designed to make the execution of the time-series code, visualization of the summer median composites, and time-series charts interactive, user-friendly, and intuitive. Moreover, the panels and corresponding widgets were distributed harmonically in the layout of the GEE web application.

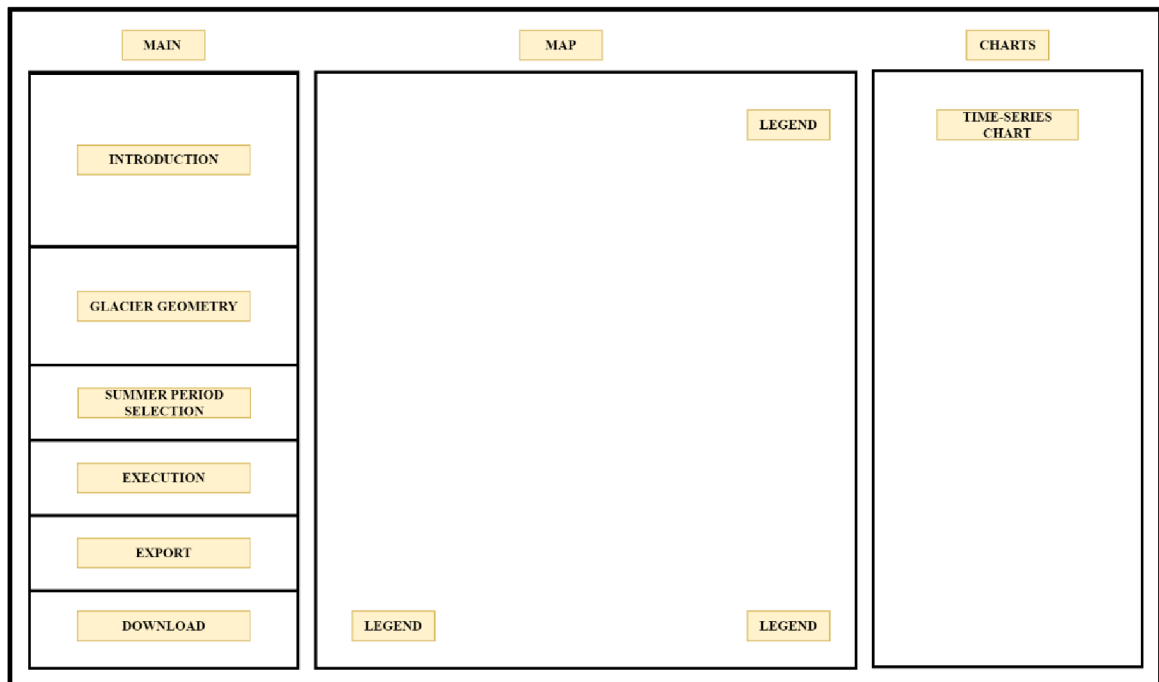


Figure 39 Layout distribution for the principal panels used in the GUI design.

5.1 Main Panel

The main panel, arranged on the left side of the page layout, was designed to introduce the application to the user and allow the selection, through widgets such as selectors and buttons, of glacier and summer periods of interest for running the time-series analysis. Moreover, it contains the download functionalities for the remote sensing outputs.

5.1.1 Introduction Panel

The introduction panel consists of three auxiliary panels and three label widgets created using the *ui.Label()* constructor function. Within the **label widgets**, there are the application name, a detailed description of the application purpose and data used, and the “Supported by” text. Regarding the auxiliary panels, the **Informative Links panel** was created to horizontally arrange the complementary links for accessing a YouTube tutorial and the 3D CesiumJS web application. Within the **Universities Logos panel**, two **thumbnail widgets**, defined using the *ui.Thumbnail()* constructor function, were used to display horizontally the logos of the supporting institutions. Finally, on the **Credits panel**, the author's name and the current GEE Web application version are displayed.

5.1.2 Glacier Geometry Panel

The Glacier Geometry panel was defined to display widgets that allow users to select a desired glacier, create custom geometries, or introduce a GeoJSON geometry. First, a **label widget** was added to this panel to inform users that selecting a glacier is the first requirement before executing the time-series code. Then, the *ui.Select()* constructor function was used to create a **select widget** with the “glacier_list” Feature Collection to filter the AOI for the time-series analysis. Moreover, the *centerObject()* function ensures that every time the selection changes, the map automatically zooms to the new selection.

Following the selection widget, an additional **label widget** was added to inform users about the options for drawing custom geometries or importing GeoJSON geometry text as an alternative AOI for the time-series analysis. Subsequently, three buttons were defined using the *ui.Button()* constructor function to enable these functionalities.

The **“Draw Geometry”** button allows the creation of custom geometries through a rectangular area using the *drawingTools()* function. The **“GEOJSON”** button triggers a dialog box where users can paste the geometry definition from a GeoJSON file (Figure 40) to create a custom geometry. Finally, the **“Clear”** button removes any created custom geometries.

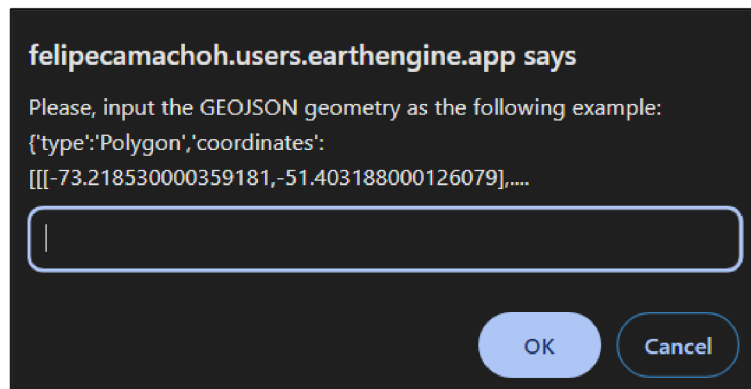


Figure 40 Dialog box created when clicking the “GEOJSON” button.

5.1.3 Summer Period Selection Panel

The main purpose of the Summer Period Selection panel was to guide the user to the second input required to execute the time-series analysis code, which was selecting the summer period of interest. As a result, this panel consists of a label widget indicating that indeed is the second step and a selector widget that the user can use to select summer periods from 2018/19 to 2022/23. The time-series code implementation will use this selection to create the summer median composites just for that summer. However, the time-series charts will not be influenced by it, as they will consider all the summers from 2018 to 2023.

5.1.4 Execution Panel

The Execution panel contains a label widget indicating a third step for the user, which is code execution. Next to it, a button widget was added that, when clicked, will run the time-series analysis code presented in Section 4 with the current glacier and summer period selection. In detail, when clicked, the resulting summer median composites and the true color image will be added to the map, along with the corresponding legend created

with thumbnail widgets. Moreover, the time-series charts will be displayed and added to the Time-Series Charts panel, and the visualization of the Export panel will be enabled.

5.1.5 Export Panel

As mentioned in section 5.1.4, the Export panel is displayed after executing the time-series analysis. This panel was designed to allow the user to download any of the resulting summer median composites directly. It is composed of a label widget that states it is the fourth step, a select widget for allowing the selection of the desired imagery, and an export button that will create a downloadable link or start the download task for exporting the imagery into Google Drive.

5.1.6 Download Panel

The Download panel is the last secondary panel within the main panel. It was created to display the resulting download URL generated using the export button.

5.2 Map Panel

Next to the main panel is the Map panel, constituted by a map instance, created with the *ui.Map()* widget, and various Legend panels used to create and display the corresponding legend for each summer median composite.

5.2.1 Map

The Map (Figure 41) provides visualization of the imagery outputs from the time-series analysis, as well as the RGI 7.0 Patagonian glaciers outlines. It allows users to draw custom geometries, zoom, pan, and control the layer's visibility.

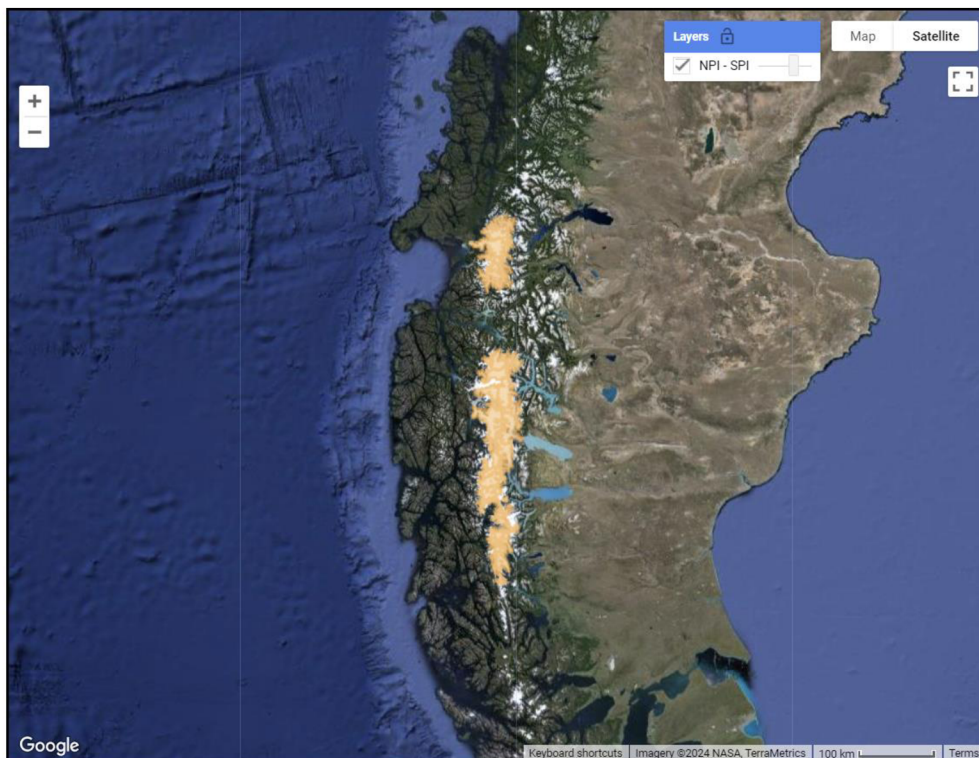


Figure 41 Interactive Map used to visualize input and output data.

5.2.2 Legend Panels

To dynamically provide the corresponding symbology (Figure 42) for the glacier area, LST temperature, and air temperature summer median composites visualized in the map area, three-panel widgets were used.

For **glacier area** outputs, a categorical symbology with two distinct colors was implemented: blue for “Presence” and red for “Absence”. This symbology was combined with label widgets to create the Glacier Area legend panel, located in the lower left area.

The outputs for **LST** and **air temperature** were represented using a graduated color symbology, which utilized a continuous color scheme. For LST, a plasma palette was utilized, with purple representing the lowest values and yellow the highest ones. The air temperature output, on the other hand, utilized a palette that ranged from dark blue to light yellow. The resulting LST panel was positioned in the right upper corner, while the air panel was positioned in the right lower corner.

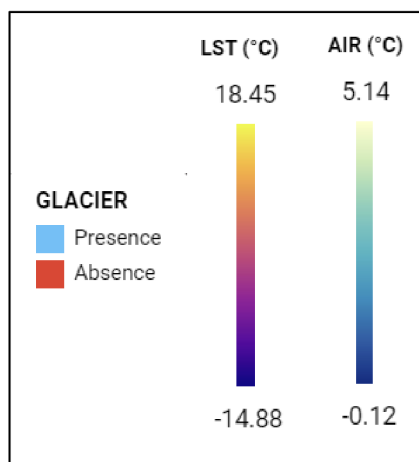


Figure 42 Example of the symbology for the Amalia glacier summer median composites for 2018/19 summer.

5.3 Charts Panel

The final panel in the GEE application layout is the **Charts panel**. It is placed vertically next to the map panel and consists of a **label widget** that acts as a title and the **Time-Series Charts panel**. This panel contains all three time-series charts, with text descriptions for the title, horizontal, and vertical axis (Figure 43), generated after executing the time-series analysis code described in section 4.3.

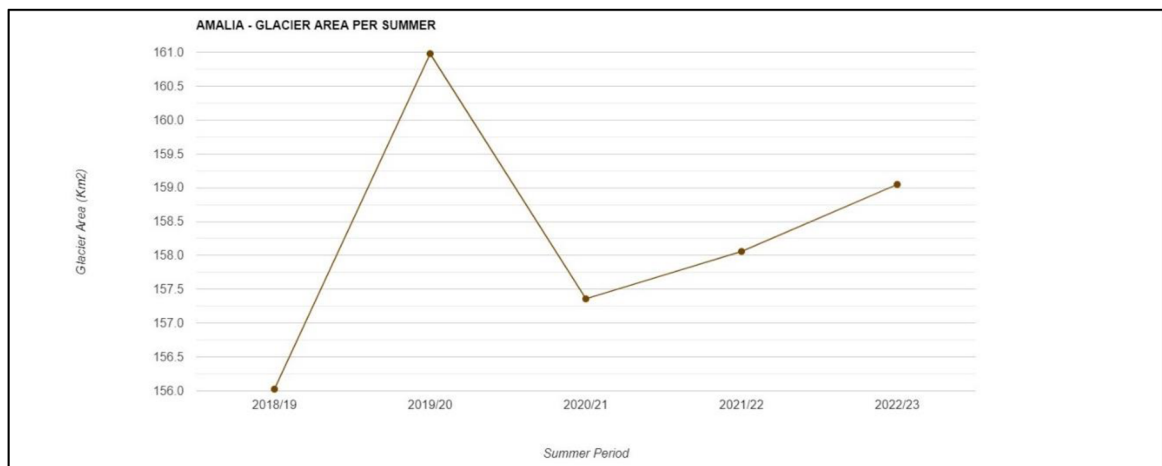


Figure 43 Example of the Glacier Area time-series chart for Amalia Glacier.

6 3D WEB APPLICATION DEVELOPMENT

After finishing the development of the “Patagonian Glaciers Monitoring Application” GEE web application, the summer median composites and time-series charts for all 83 glaciers were exported using the interactive interface. However, due to the maximum pixel number limitation when exporting, the composites were not exported using the download link but instead through a task that saved them directly in Google Drive. The composites exporting parameters included the TIFF format, a scale parameter of 30 m, and the WGS84 projection. As a result, 1245 summer median composites and 249 time-series charts, exported as CSV files, were generated.

Accordingly, this section will detail the processing workflow carried out for the GEE application outputs and the cloud hosting. Furthermore, it will outline the code implementation for the 3D CesiumJS application that enabled the retrieval and 3D visualization of the cloud-hosted summer median composites and time-series charts via an interactive interface with functionalities such as sidebar, swipe, and others.

6.1 GEE Web Application Outputs Processing

The summer median composites were processed to remove unwanted footprints, match the symbology, and ensure the best performance before being cloud-hosted. Similarly, the time-series charts exported from GEE were improved by fitting a linear regression and calculating R^2 , RMSD, and RRMSD.

6.1.1 Summer Median Composites

Glacier Area Summer Median Composites

As established in section 4.2.6, the *Glacier_Area_Delineation()* function was used to delineate glacier and non-glacier areas by applying a mask, where values of 1 corresponded to the glacier, and 0 for non-glacier. However, when exporting the glacier area summer composites and adding them to ArcGIS Pro, it was observed that the image included the complete footprint with pixel values of 0, the same pixel value assigned for non-glacier areas. Because of this, new mask values were applied in GEE before exporting the composites: -1 corresponds to non-glacier areas, 0 to the footprint, and 1 to glacier areas (Figure 44).

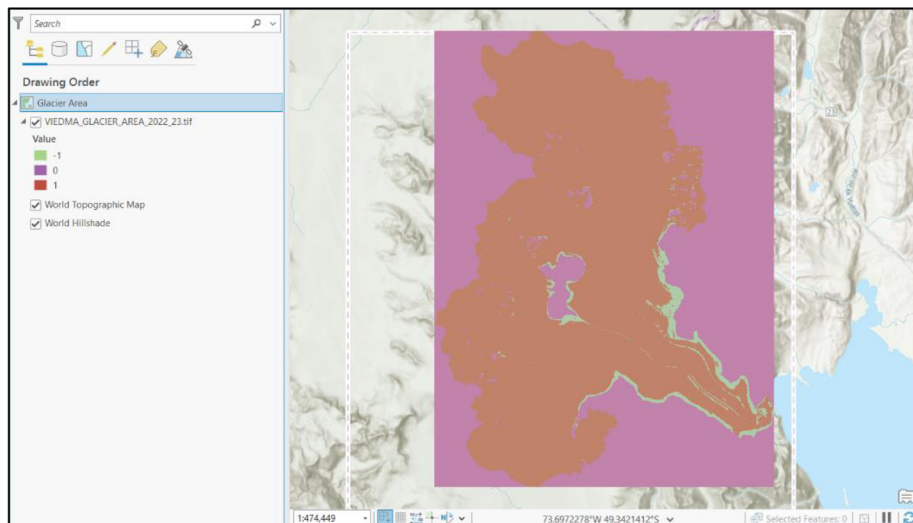


Figure 44 Glacier Area 2022/23 Summer Median Composite for Viedma glacier, exported from GEE, added to ArcGIS Pro.

With all the glacier area summer composites exported, in ArcGIS Pro, the pixels with a value of 0 were removed, and the symbology was updated to match the colors presented in section 5.2.2. The processed composites were then exported locally as TIFF files, using the “Export Raster” tool with the “Force RGB” and “Use Rendered” options checked on, to be exported as three-band rasters, maintaining the current color settings (Figure 45). Moreover, to reduce the size as much as possible, the LZW compression type was used.

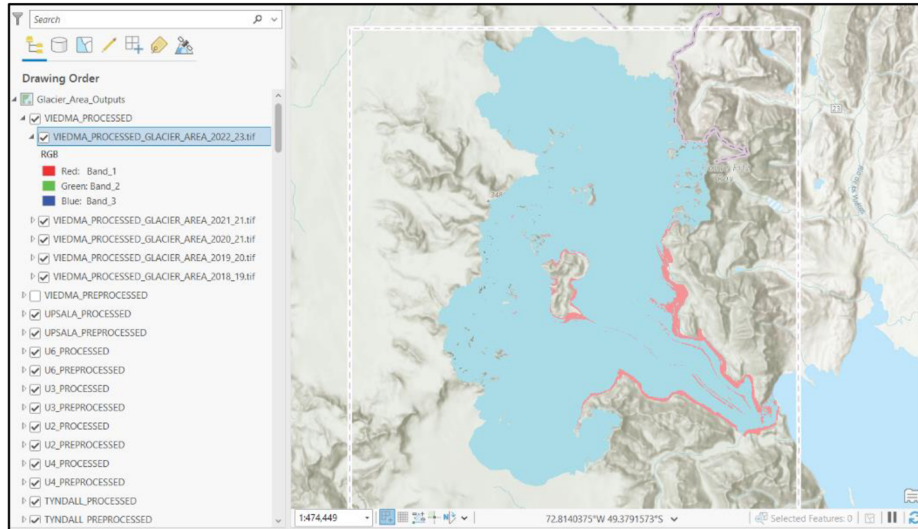


Figure 45 Processed three-band Glacier Area 2022/23 Summer Median Composit for Viedma Glacier, with permanent color settings.

LST and Air Temperature Summer Median Composites

With the LST and air temperature summer median composites exported from GEE, the main goal was to create comparable TIFF files. This means finding the minimum and maximum possible values for LST and air temperature composites to apply the same stretch values in the symbology of each image.

For this purpose, the exported composites were added to ArcGIS Pro, observing that the footprint was also included. However, instead of having pixel values of 0, they had “NoData” values. Therefore, to remove the “NoData” footprint pixels, a model (Figure 46) created with Model Builder was implemented.

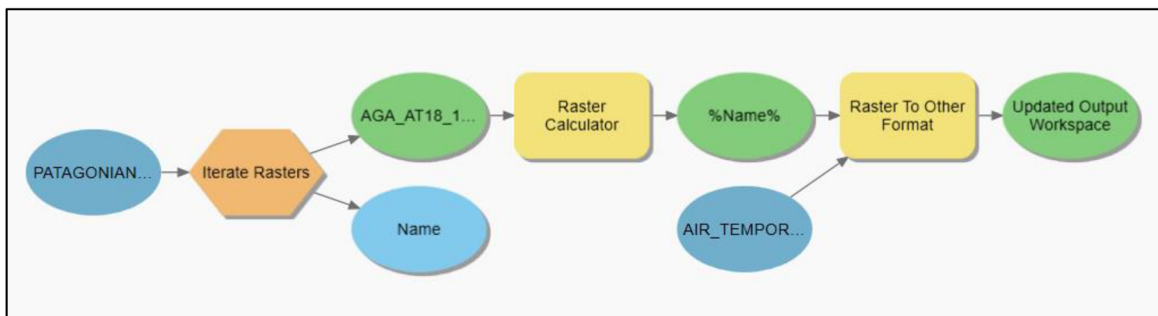


Figure 46 Model Builder workflow used to convert pixels with “NoData” values into pixels with a value of 0.

The model was applied separately to the LST and air temperature summer median composites. It consisted of iterating through each raster, converting the 'NoData' pixels to a value of 0 by multiplying the raster by 1 using the 'Raster Calculator' tool, and ultimately exporting it as a new TIFF file.

Then, the minimum and maximum pixel values were retrieved by comparing all the pixel values of the exported TIFF files using a Python script (Figure 47). As a result, the LST summer median composites had a minimum pixel value of -32.85 and a maximum pixel value of 34.45. On the other hand, the minimum and maximum pixel values for the air temperature summer median composites were -2.64 and 11.05, respectively.

```

aprx = arcpy.mp.ArcGISProject("CURRENT")
map = aprx.listMaps()[3]
global_max = None
global_min = None
for layer in map.listLayers():
    if layer.isRasterLayer:
        raster = arcpy.Raster(layer.dataSource)
        min_val = raster.minimum
        max_val = raster.maximum
        if global_max is None or max_val > global_max:
            global_max = max_val
        if global_min is None or min_val < global_min:
            global_min = min_val
        print(f"Raster: {layer.name}, Min: {min_val}, Max: {max_val}")
print(f"Global Minimum: {global_min}, Global Maximum: {global_max}")

```

Figure 47 Python Code – Retrieval of the minimum and maximum pixel values for the LST and air temperature summer median composites.

With these values, the symbology type for all the rasters was defined as “Stretch”, using the corresponding minimum and maximum pixel values (Figure 48A & Figure 48B)

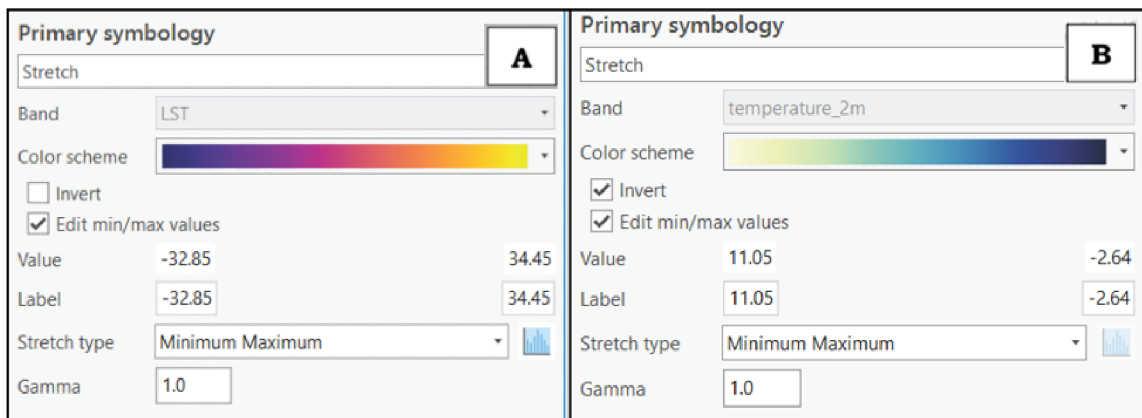


Figure 48 A) Symbology applied for the LST Summer Median Composites. B) Symbology applied for the Air Temperature Summer Median Composites.

Finally, as for the glacier area composites, the processed LST (Figure 49A) and air temperature (Figure 49B) composites were then exported locally as TIFF files, with the “Export Raster” tool and the “Force RGB” and “Use Rendered” options checked, using the LZW compression type as well.

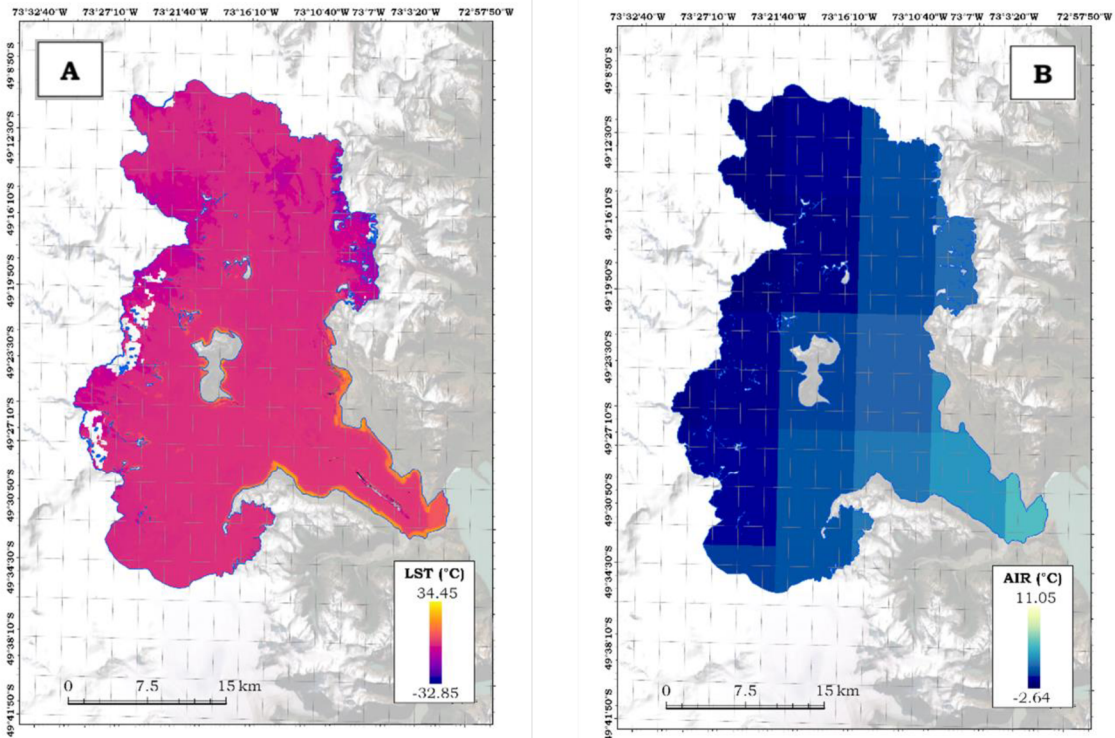


Figure 49 A) Processed 2022/23 LST Summer Median Composite for Viedma Glacier. Projection: WGS 1984 UTM Zone 18S, Scale: 1:250,000. B) Processed 2022/23 Air Temperature Summer Median Composite for Viedma Glacier. Projection: WGS 1984 UTM Zone 18S, Scale: 1:250,000.

6.1.2 Time-Series Charts

After exporting the 249 time-series charts from the GEE Web application (Figure 50), a linear regression was fitted to each, using Microsoft Excel, to estimate the rate of change for the glacier area, LST, and air temperature. From this linear regression, the mean regression value, R^2 , RMSD, and RRMSD were derived. Specifically, RMSD was calculated for the LST and air temperature linear regressions (Figure 51B & Figure 51C), while RRMSD was estimated for the glacier area linear regressions (Figure 51A). The purpose of these statistical measures was to assess the accuracy of the linear regression, enabling users to determine whether the estimated rate changes were significant.

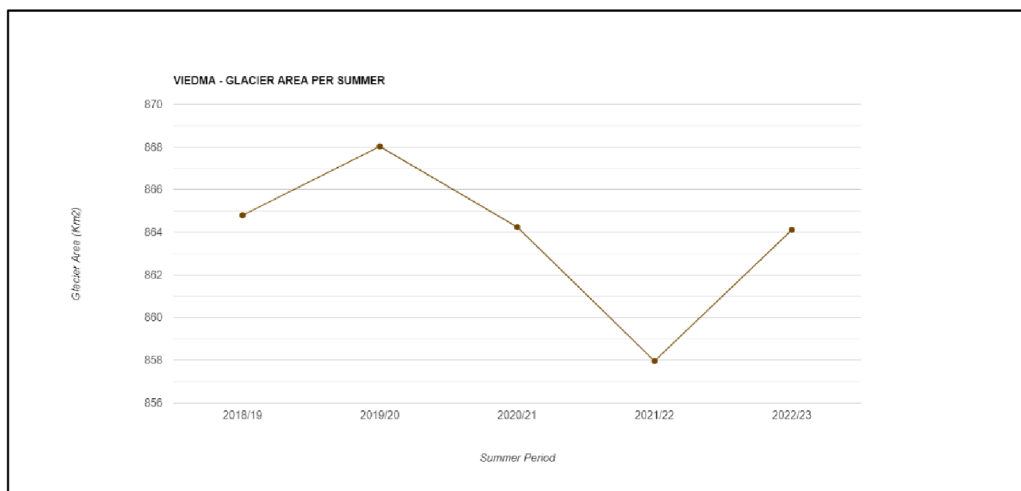


Figure 50 Original Glacier Area time-series chart generated in GEE web application.

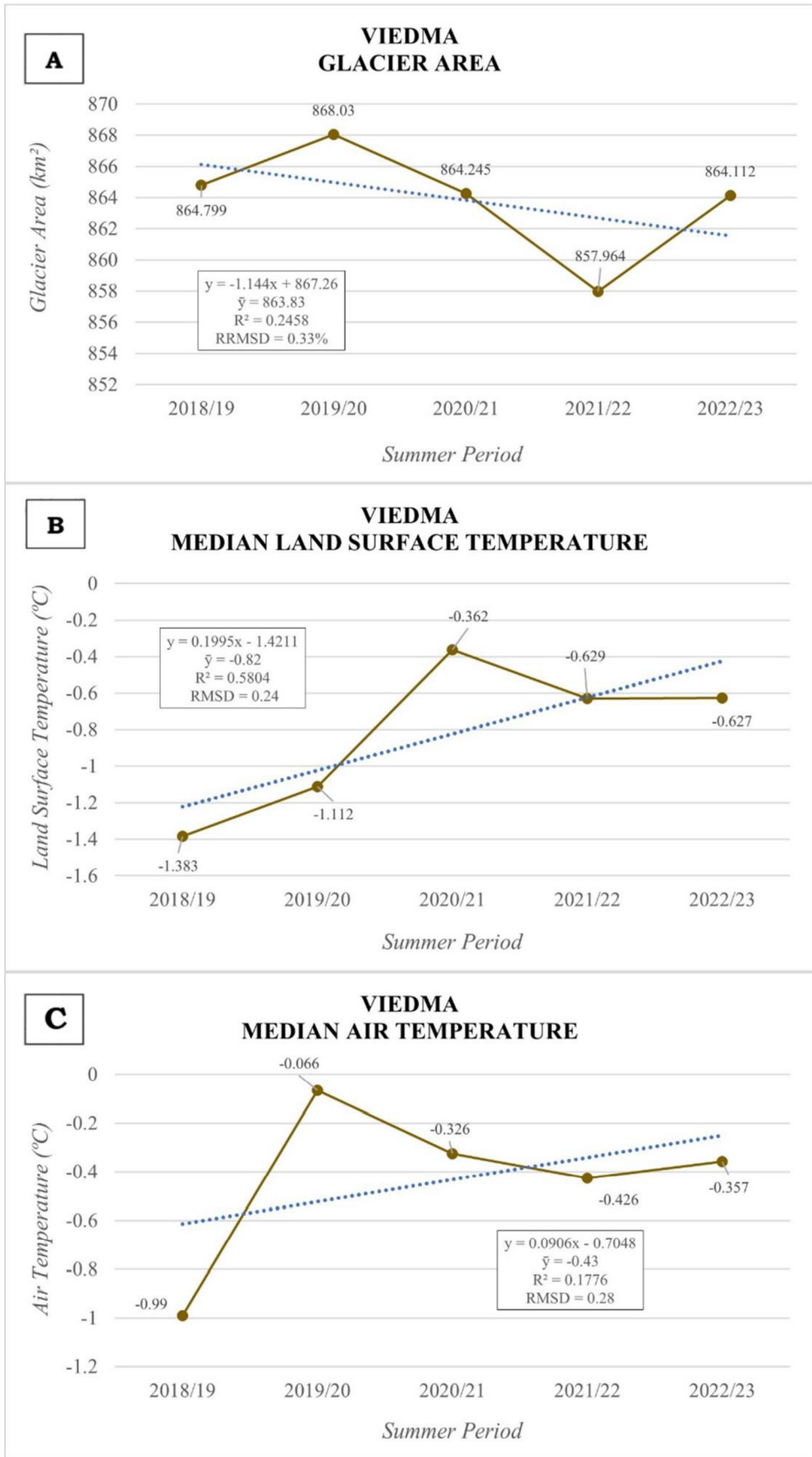


Figure 51 A) Processed glacier area time-series chart for Viedma glacier. B) Processed LST time-series chart for Viedma glacier. C) Processed air temperature time-series chart for Viedma glacier.

6.2 Cloud Hosting

In the case of the **summer median composites**, once they were exported locally as TIFF files, they were individually uploaded to Cesium Ion (Figure 52), where they were automatically tiled, projected to WGS84 Web Mercator (Auxiliary Sphere), and given a unique identifier, latter used to retrieve specific images in the 3D CesiumJS application.

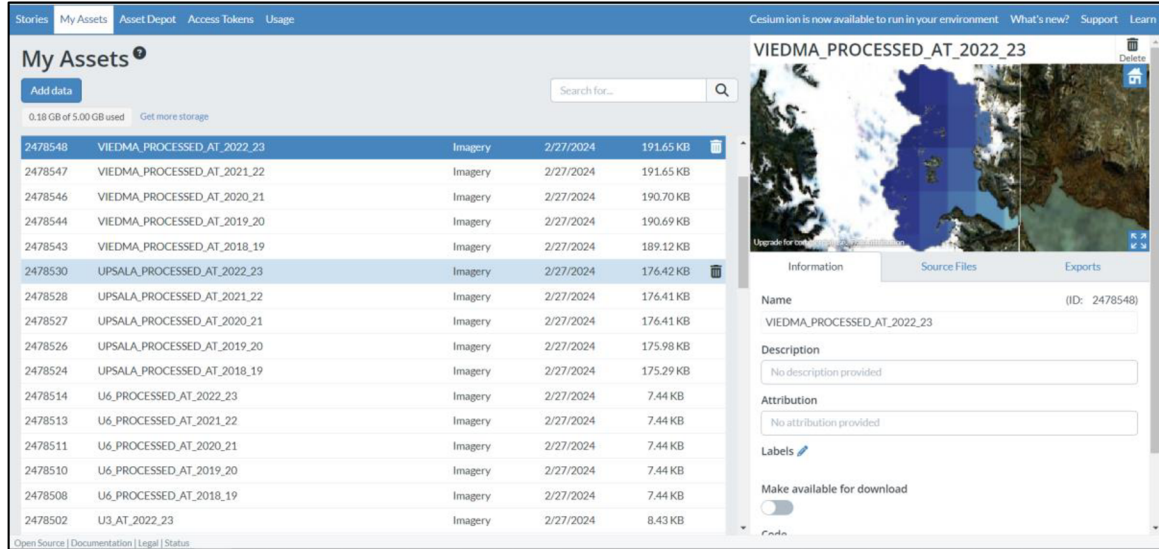


Figure 52 Preliminary view of the imagery uploaded and hosted in Cesium Ion.

Regarding the **processed time-series charts**, they were exported from Microsoft Excel as Portable Network Graphic (PNG) files and then uploaded to GitHub: https://github.com/felipecamachoh/PatagonianGlaciers/tree/main/Charts_Processed.

6.3 CesiumJS Implementation

With the required summer median composites and time-series charts available in the respective cloud hosting platforms, using Visual Studio Code, CesiumJS library, HTML, and CSS, the 3D CesiumJS application was developed. The workflow (Figure 53) initially consisted of instantiating a new cesium viewer, with the Cesium World Terrain as the terrain provider and Bing Maps Aerial Imagery as the basemap. Posteriorly, the RGI 7.0 NPI and SPI GeoJSON was preloaded, along with each of the summer median composites and time-series charts. For dynamically retrieving these summer median composites, four buttons were designed to allow the selection of glacier, composite type, and summer period of interest, filtering the summer median composite to be displayed. Furthermore, to enable the comparison side to side of the summer median composites, a swipe functionality was implemented, as well as a sidebar to interactively display the time-series charts for the selected glaciers, with additional information on the change rate. Finally, the application was complemented by creating widgets such as a legend panel, distance scale, introduction screen, display controls, and more. The application source code is hosted in GitHub and can be accessed at: <https://github.com/felipecamachoh/PatagonianGlaciers/blob/main/3DMonitoringApp.html>.

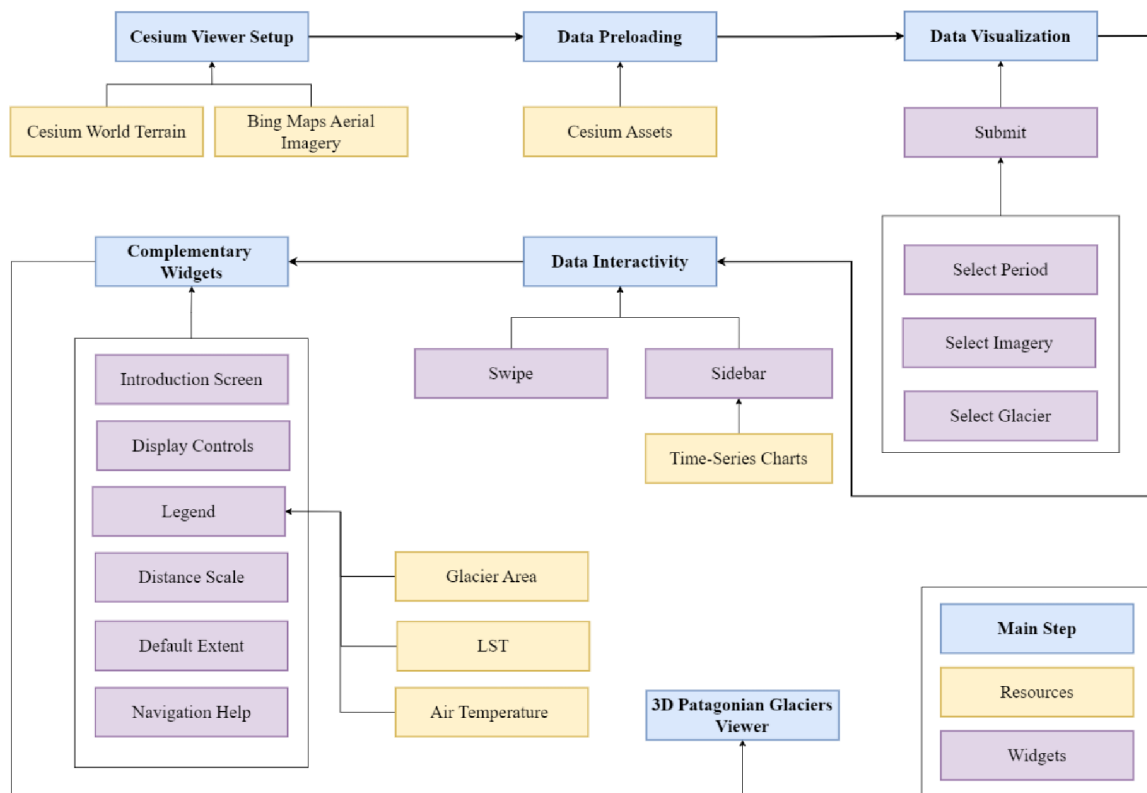


Figure 53 3D CesiumJS Web Application development steps.

6.3.1 Cesium Viewer Setup

The first step when working with the CesiumJS library is to create a new instance of the Cesium Viewer class and define its initial properties. Specifically, in this CesiumJS implementation, a new viewer was created (Figure 54), with the Cesium World Terrain as the terrain provider and disabling properties such as animation, timeline, and base layer picker. These properties were not enabled to reduce unnecessary complexity and streamline user interaction with the application. Additionally, after creating the viewer, the Bing Maps Aerial Imagery was added as the default basemap (Figure 55).

```
const viewer = new Cesium.Viewer('cesiumContainer', {
  terrain: Cesium.Terrain.fromWorldTerrain(),
  animation: false,
  timeline: false,
  baseLayerPicker: false,
  imageryProvider: false,
  scene3DOnly: true,
  shadows: false,
  geocoder: false,
  allowTextureFilterAnisotropic : false,
});
```

Figure 54 Cesium Code – Instantiation of the new Cesium Viewer.

```
const layer = viewer.imageryLayers.addImageryProvider(
  await Cesium.IonImageryProvider.fromAssetId(2)
);
```

Figure 55 Cesium Code – Definition of the Bing Maps Aerial Imagery (Asset 2) as default basemap.

6.3.2 Data Preloading

In this step, the GeoJSON containing the outlines of the NPI and SPI glaciers, along with the summer median composites and the time-series charts, were preloaded. Regarding the **GeoJSON**, the `loadGeoJson()` function (Figure 56) was created to load the corresponding Cesium Ion asset and add it to the Cesium viewer, with the 'clampToGround' property set to true. This property ensured the GeoJSON was properly aligned with the terrain's surface (Figure 57).

```
async function loadGeoJson() {  
  const resource = await Cesium.IonResource.fromAssetId(2452161);  
  geoJsonDataSource = await Cesium.GeoJsonDataSource.load(resource, {  
    clampToGround: true,  
    fill: new Cesium.Color(30/255, 33/255, 70/255, 0.5),  
  });  
}
```

Figure 56 Cesium Code – Loading of GeoJSON asset corresponding to the NPI and SPI glacier outlines.



Figure 57. Visualization of NPI and SPI glaciers clamped to the ground with CesiumJS.

In the case of the **summer median composites**, an object was created within a function with a set of keys based on combinations of glacier name, year, and type of imagery (Figure 58). Each key was then associated with the corresponding Cesium Ion asset ID. This function and the object facilitated the management and display of multiple assets, allowing the imagery to be added on demand according to user selection.

```
function getAssetId(name, year, imageryType) {
  const assetMapping = {
    'VIEDMA-2018 - 2019-Glacier Area': 2472233,
    'VIEDMA-2018 - 2019-Land Surface Temperature': 2474731,
    'VIEDMA-2018 - 2019-Air Temperature': 2478543,
  };
  return assetMapping[`${name}-${year}-${imageryType}`];
}
```

Figure 58. Cesium Code – Simplified version of the `getAssetId()` function and object keys and values.

Finally, for the **time-series charts**, the `preloadImages()` function was created and implemented (Figure 59) to initiate the loading process for each image immediately after the web application starts.

```
function preloadImages(imageUrls) {
  imageUrls.forEach(url => {
    const img = new Image();
    img.src = url;
  });
}
```

Figure 59 Cesium Code – Function for loading the time-series charts PNG images in advance.

6.3.3 Data Visualization

As mentioned in the previous section (6.3.2), the summer median composites visualization is based on the user selections for glacier, summer period, and imagery type parameters. To collect and store this information, four buttons were created:

- Select Glacier: used for selecting any of the 83 Patagonian glaciers
- Select Summer Period: allows selecting between six different summer periods
- Select Imagery Type: enable selecting which type of summer composite to be added, including: “GLACIER AREA”, “LAND SURFACE TEMPERATURE”, and “AIR TEMPERATURE”
- Add Imagery: used to retrieve the specific asset ID with the `getAssetId()` function and add it to the Cesium viewer.

Once the parameters are correct and the “Add Imagery” button is clicked, it was configured that the glacier area summer composites will be added with a transparency of 0.5, while the temperature summer composites will use a transparency of 0.8. These transparency values were selected to permit the visualization of the underlying Bing Imagery when adding the glacier area composites but reduce its visibility when adding the temperature composites.

6.3.4 Data Interactivity

A fundamental part of the 3D CesiumJS web application is the possibility of comparing different imagery side by side. To achieve this, **swipe** functionality was implemented through the creation of a divisor and a handle, using HTML and CSS, and the usage of the `scene.splitPosition()` and `SplitDirection()` methods. The `scene.splitPosition()` method allowed the splitting of the viewer into two parts, while with the `SplitDirection()`

method, it was possible to define the side on which the summer composites would be added. In addition to the swipe functionality, checkboxes were created to dynamically enable or disable the visualization of the imagery on any of the split sides (Figure 60).

```
if (checkbox1.checked && checkbox2.checked) {
    layer.splitDirection = Cesium.SplitDirection.NONE;
} else if (checkbox1.checked) {
    layer.splitDirection = Cesium.SplitDirection.LEFT;
} else if (checkbox2.checked) {
    layer.splitDirection = Cesium.SplitDirection.RIGHT;
} else {
    layer.splitDirection = Cesium.SplitDirection.NONE;
}
```

Figure 60 Cesium Code – Split direction based on the checkbox status.

Another interactive feature is the **sidebar**, which is enabled by the InfoBox class in Cesium. To populate it dynamically based on the glacier selection, predefined descriptions for each glacier were designed. These include information such as the time-series charts for the glacier area, LST, and air temperature, as well as the change rates and area loss relative to the RGI 7.0.

6.3.5 Complementary Widgets

With the main functionalities already covered, the 3D Cesium JS Web application was completed through the creation of new widgets or assignment of custom functionalities for the existing ones.

For example, a series of **introductory screens** (or splash screens) were created using different HTML tags to display information on how to use the application. In detail, on four introductory screens, informative text, links, images, and interactive buttons were displayed.

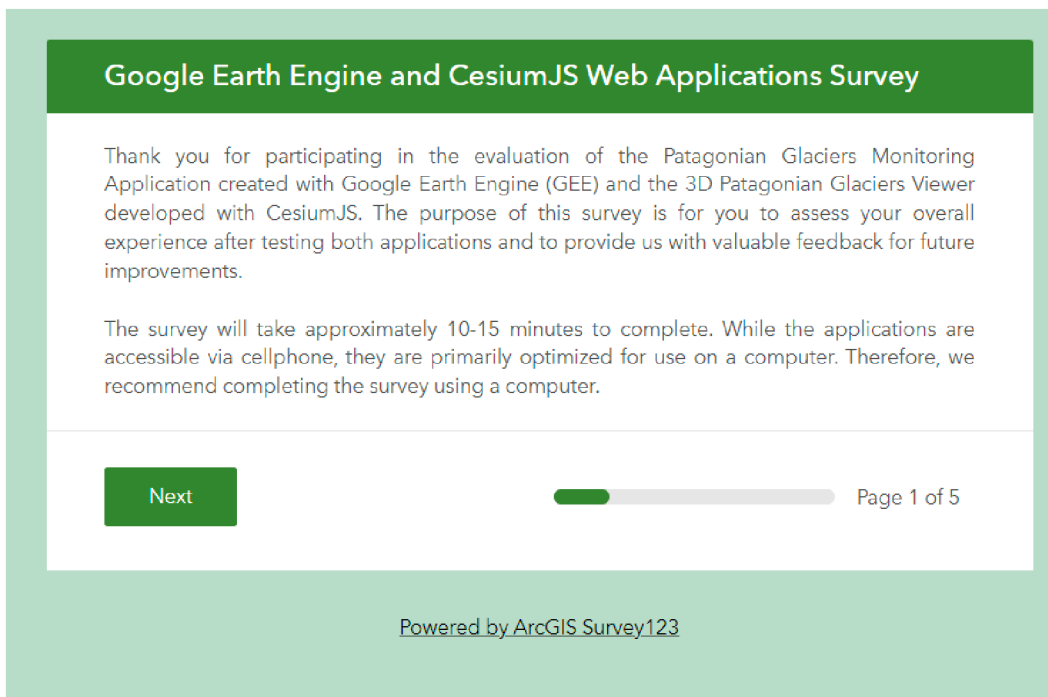
Another widget is the **display controls** panel, designed to store the layer visibility controls, including the checkboxes for turning on or off the layers and a slider for modifying the transparency.

For the **legend**, a div container with three rows and one column was used to store and show the corresponding symbology for the different types of imagery added. Moreover, a button was designed to allow the panel to be closed and opened.

The last widget implemented was the **distance scale**, which uses kilometer units. Additionally, the functionalities of the existing **default extent** button and **navigation help** button were modified to zoom to the Patagonian region and display the introductory screens, respectively, when activated.

7 USERS EVALUATION

The last step of the methodology presented in this study is the evaluation of the web applications by the end-users. For this purpose, a form was created using ArcGIS Survey123 (Figure 61) with questions regarding the scientific background of the contestants, their experience with the GEE and 3D CesiumJS web applications, and their personal perspectives concerning the usage and impact of ready-to-use applications. Once the form design was finished, it was shared through LinkedIn. The survey was not focused on assigning specific tasks but on assessing the overall user experience by reproducing the steps outlined in the tutorials. The online survey is available at: <https://survey123.arcgis.com/share/f81642724caf45bc8053c291a1d440a5>



Google Earth Engine and CesiumJS Web Applications Survey

Thank you for participating in the evaluation of the Patagonian Glaciers Monitoring Application created with Google Earth Engine (GEE) and the 3D Patagonian Glaciers Viewer developed with CesiumJS. The purpose of this survey is for you to assess your overall experience after testing both applications and to provide us with valuable feedback for future improvements.

The survey will take approximately 10-15 minutes to complete. While the applications are accessible via cellphone, they are primarily optimized for use on a computer. Therefore, we recommend completing the survey using a computer.

Next Page 1 of 5

Powered by ArcGIS Survey123

Figure 61 Initial screen of the ArcGIS Survey 123 form.

User Profile Section

This section was the initial part of the form, where respondents were asked about their age range and their level of familiarity with terms such as Glaciology, Remote Sensing, Time-Series Analysis, GEE, and CesiumJS. The options available for indicating familiarity were “Not at all familiar”, “Slightly Familiar”, “Moderately Familiar”, “Very Familiar”, and “Extremely Familiar”.

GEE Web Application Section

To evaluate the user experience with the GEE web application, a link to a video tutorial was provided in this form section, available at <https://www.youtube.com/watch?v=oGDtU-05zLg>. Then, users were asked to replicate the steps and rate the interface considering the attractiveness, intuitiveness, and user-friendliness, and performance based on their experience by choosing from “Very poor”, “Poor”, “Fair”, “Good”, and “Excellent” options. Moreover, they were asked, if applicable, to report any experienced bug.

3D CesiumJS Web Application Section

Similarly to the GEE Web Application section, the users were requested to rate the interface and performance of the 3D CesiumJS Web application after following a video tutorial, available at <https://www.youtube.com/watch?v=m7tQ8Tt5EJk>. Additionally, they were asked if the 3D perspective facilitated understanding the glacier area and temperature changes.

Overall Experience Section

In the last section of the form, users were asked to select the application that made the visualization of glacier areas and temperature changes more attractive. They were also asked about their level of agreement regarding the role of ready-to-use applications in providing useful scientific information and promoting scientific interest among the general population (Figure 62). The available options for the level of agreement were “Strongly disagree”, “Disagree”, “Neutral”, “Agree”, and “Strongly agree”.

Google Earth Engine and CesiumJS Web Applications Survey

Overall Experience

In which application was the visualization of glacier areas and temperature changes more attractive?

PATAGONIAN GLACIERS MONITORING APPLICATION (Google Earth Engine)

3D Patagonian Glaciers Viewer (CesiumJS)

Do you agree with the idea that ready-to-use applications like the ones tested provide useful information and tools for both scientific and non-scientific communities?

Strongly disagree Disagree Neutral Agree Strongly agree

Do you agree with the idea that ready-to-use applications like the ones tested can increase general population interest in Earth dynamics, such as changes in glacier areas and temperatures?

Strongly disagree Disagree Neutral Agree Strongly agree

Figure 62 GEE and CesiumJS Web Applications survey - Overall experience section.

8 RESULTS

This chapter presents the results of the study, including the outputs from the time-series analysis, the GEE and 3D CesiumJS web applications, and the findings from the ArcGIS Survey123 form.

8.1 Time-Series Analysis Outputs

With the time-series analysis performed within the GEE cloud platform described in Chapter 4, 1245 summer median composites and 249 time-series charts, equivalent to the 83 analyzed glaciers, were generated through the GEE web application GUI. This data can be accessed through the application itself and the “PatagonianGlacier” GitHub repository, which includes the pre-processed and processed datasets for the summer median composites and time-series charts. The repository is available online at <https://github.com/felipecamachoh/PatagonianGlaciers>.

With the processed time-series charts, fitted a linear regression and having calculated R^2 , RMSD, and RRMSD, as described in subchapter 6.1.2, it was compared the rate of change in glacier area, LST, and air temperature across all studied glaciers, identifying those with the most significant changes. Additionally, with the RGI 7.0 glacier area values, the year of measurement, and the glacier area for the summer period of 2022/23, the total area loss between this period of time was estimated as a complementary output. The complete consolidated tables can be accessed in the Appendix section or at https://github.com/felipecamachoh/PatagonianGlaciers/tree/main/RateChanges_Tables.

Specifically, for glacier area changes (Table 3), PIO XI, Tempano, and Bernardo glaciers showed the highest rates of area increase since summer 2018/19, at 1.95, 1.90, and 0.89 square kilometers per summer, respectively. Conversely, HPS 38, O’Higgins, and Viedma experienced the most significant losses, with rates of -0.95, -1.09, and -1.14 square kilometers per summer, respectively.

Table 3 Glaciers with the most significant glacier area rate of change.

GLACIER	RGI 7.0 AREA (Km ²)	YEAR	2022-2023 AREA (Km ²)	GAIN/LOSE (Km ²)	RATE OF CHANGE Km ² /summer	R ²	RRMSD
PIO XI	1233.08	2001	1223.32	-9.76	1.95	0.1734	0.49%
TEMPANO	433.91	2001	410.92	-22.99	1.90	0.0805	2.19%
BERNARDO	565.14	2001	551.52	-13.62	0.89	0.063	0.89%
HPS38	69.81	2001	61.082	-8.73	-0.95	0.6415	1.63%
O’HIGGINS	780.49	2001	767.112	-13.38	-1.09	0.5549	0.18%
VIEDMA	896.36	2001	864.112	-32.25	-1.14	0.2458	0.33%

Moreover, regarding the glacier area loss (Table 4) from the RGI 7.0 year of measurement to the summer of 2022/23. Upsala, Viedma, and Colonia were the glaciers that lost more area, with area losses of -37.14, -32.25, and -23.22 square kilometers. On the other hand, HPS27, HPS33, and Calvo glaciers lost less glacier area, showing a loss of -0.13, -0.1, and -0.07 square kilometers.

Table 4 Glaciers with the highest and lowest glacier area loss.

GLACIER	RGI 7.0 AREA (Km ²)	YEAR	2022-2023 AREA (Km ²)	AREA LOSE (Km ²)	RATE OF CHANGE Km ² /summer	R ²	RRMSD
UPSALA	778.97	2005	741.83	-37.14	-0.28	0.0037	0.89%
VIEDMA	896.36	2001	864.112	-32.25	-1.14	0.2458	0.33%
COLONIA	282.07	2001	258.854	-23.22	-0.73	0.7385	0.24%
HPS27	31.84	2001	31.71	-0.13	-0.02	0.0526	0.44%
HPS33	19.12	2001	19.023	-0.1	-0.03	0.6085	0.17%
CALVO	99.06	2001	98.99	-0.07	0.39	0.6405	0.42%

Regarding the LST (Table 5), it was determined that HPS28, HPS22, and Ameghino glaciers showed the highest summer temperature increases, with 1.71, 1.42, and 0.85 degrees Celsius, respectively. Conversely, Snowy, Balmaceda, and HPS41 exhibited the largest summer temperature decreases, with -1.39, -1.69, and -1.83 degrees Celsius.

Table 5 Glaciers with the most significant LST rate of change.

GLACIER	RATE OF CHANGE °C/summer	R ²	RMSD
HPS28	1.71	0.7157	1.52
HPS22	1.42	0.5177	1.93
AMEGHINO	0.85	0.79	0.62
SNOWY	-1.39	0.4526	2.17
BALMACEDA	-1.69	0.8336	1.07
HPS41	-1.83	0.9275	0.72

Finally, for the air temperature time series (Table 6), it was evidenced that the glaciers experiencing the highest increase in air temperature per summer were HPS30, Cachet, and Pared Sur, with increases of 0.24, 0.21, and 0.21 degrees Celsius, respectively. On the other hand, Snowy, HPS38, and HPS39 exhibited the greatest decreases, with reductions of -0.01, -0.04, and -0.08 degrees Celsius per summer.

Table 6 Glaciers with the most significant air temperature rate of change.

GLACIER	RATE OF CHANGE °C/summer	R ²	RMSD
HPS30	0.24	0.4033	0.41
CACHET	0.21	0.4871	0.31
PARED SUR	0.21	0.2773	0.47
SNOWY	-0.01	0.0013	0.34
HPS38	-0.04	0.0382	0.3
HPS39	-0.08	0.0916	0.34

8.2 Patagonian Glaciers Monitoring Application (GEE App)

After designing the GUI for the GEE code implementation, using widgets such as panels, buttons, and charts, as described in section 5, the “**Patagonian Glaciers Monitoring Application**” GEE web application was launched and publicly shared. It is accessible online at <https://felipecamachoh.users.earthengine.app/view/patagonian-glaciers-monitoring>. The layout for the web application (Figure 63) consists of three panels. The Main panel provides the user with general information, interactive buttons, and selectors for running the time series analysis, and creating the summer median composites and time-series charts. The Map panel provides an interactive map element for visualizing the Patagonian glaciers and the remote sensing outputs. Lastly, the time series chart panel displays the time series charts.

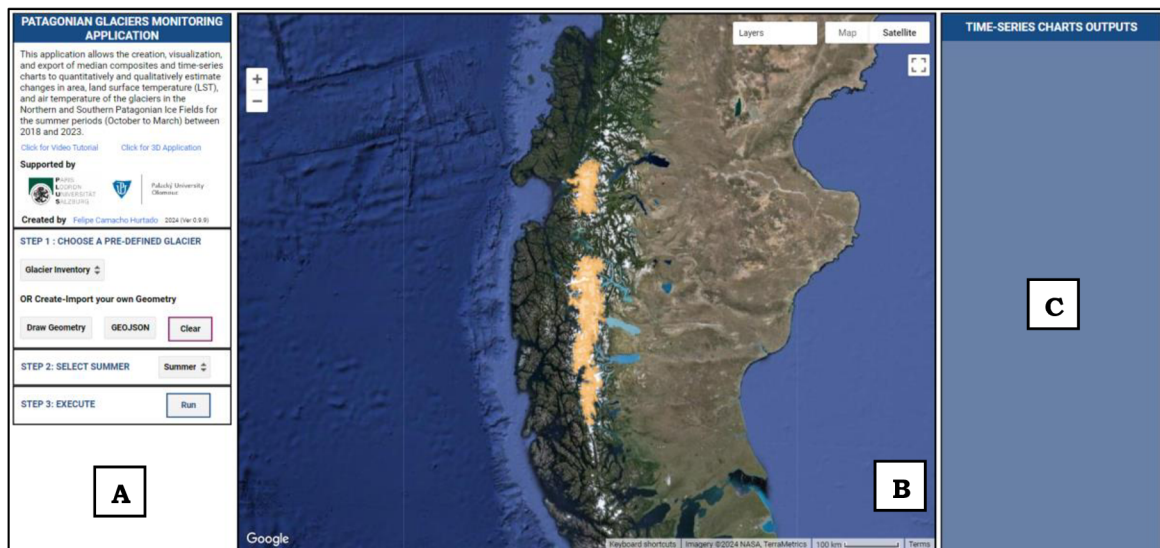


Figure 63 Patagonian Glaciers Monitoring Application – Layout distribution including Main panel (A), Map panel (B), and Time Series Chart panel (C).

In the Main panel, a series of labels guide the user through each step required to interact with the application. The step-by-step process is presented in Figure 64.

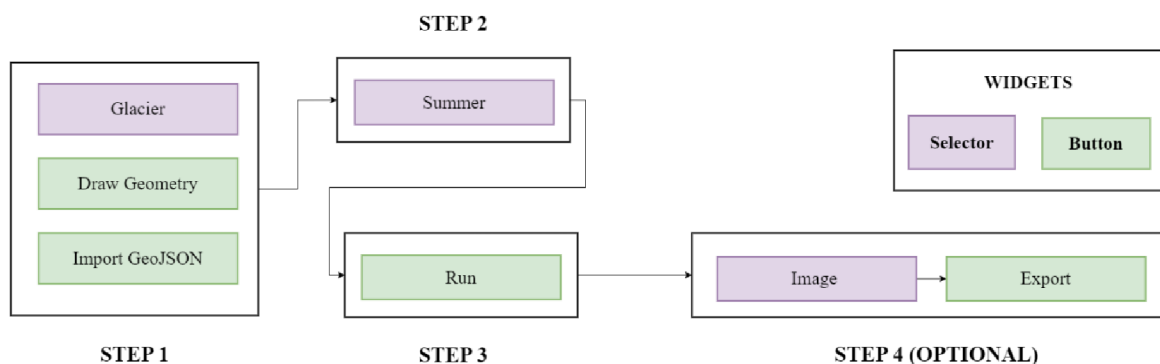


Figure 64 Operational Flowchart for Patagonian Glaciers Monitoring Application.

It first involves defining the glacier geometry that will be used to generate the time-series outputs. This could be a predefined glacier or a custom geometry. Specifically, the user can draw a rectangular geometry or import a GeoJSON geometry, such as this: https://github.com/felipecamachoh/PatagonianGlaciers/blob/main/GeoJSON_Import_Example.txt. The second step is to select the summer period of interest from 2018/19 to

2022/23. Upon setting these parameters, the third step is to execute or run the time-series analysis. At this step, GEE performs the code implementation described in Chapter 4 in the background. Once complete, the Run button will turn green, and in the Map panel, the corresponding imagery and legend will be displayed, along with the time-series charts in the Time Series Chart panel. The optional fourth step involves selecting any displayed imagery for download and clicking the Export button. If successful, the button will turn green and generate a URL, which, when clicked, starts the image bands' download process. Figure 65 presents an example of the final layout with the time-series analysis products added after completing the step-by-step.

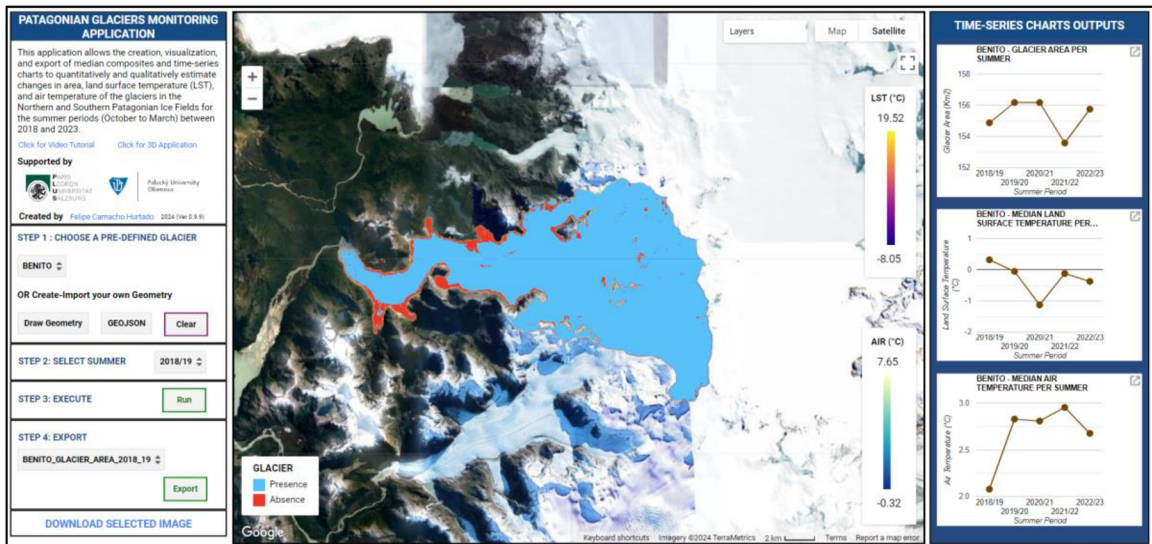


Figure 65 Patagonian Glaciers Monitoring Application – Layout distribution after completing the operational step-by-step.

Regarding the imagery added in the Map panel, it will correspond to the glacier area delimitation (Figure 66A), the median LST (Figure 66B) and air temperature composites (Figure 67A), and a true color image (Figure 67B) for a visual inspection and comparison with the glacier area delimitation composite.

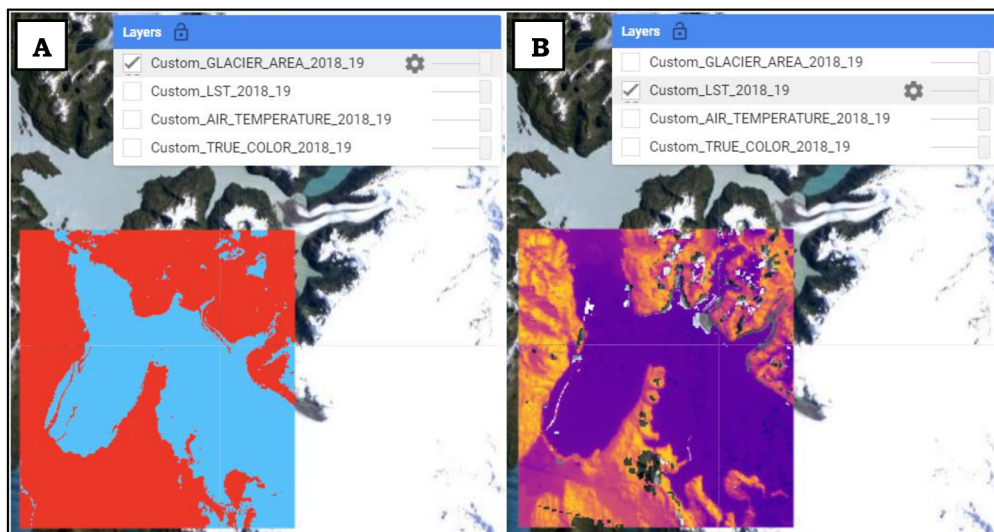


Figure 66 Patagonian Glaciers Monitoring Application – Example of imagery outputs for a custom geometry. A) Glacier Area Delineation. B) LST Median Composite.

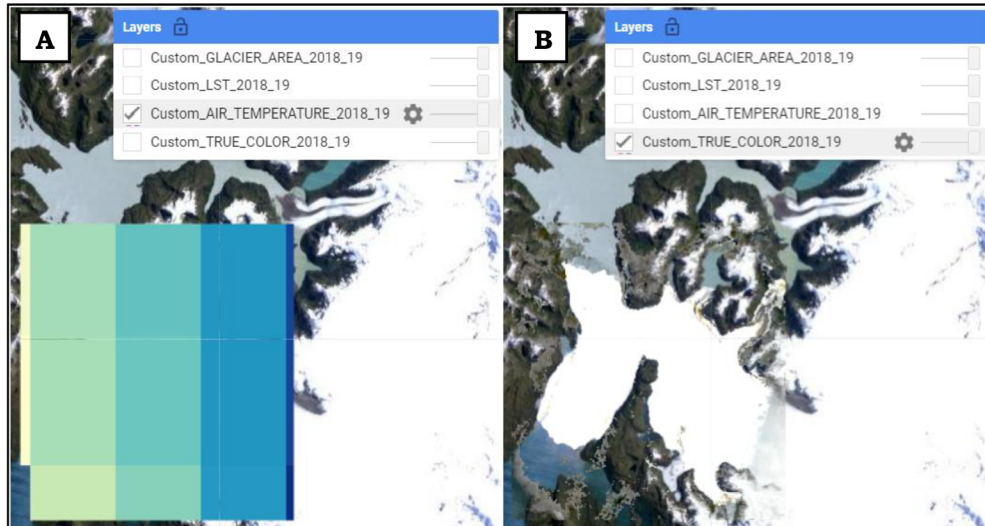


Figure 67 Patagonian Glaciers Monitoring Application – Example of imagery outputs for a custom geometry. A) Air Temperature Median Composite. B) True Color Composite.

The resulting **Patagonian Glaciers Monitoring Application** GEE web application allows users to create, visualize, and export remote sensing and time-series products for 83 Patagonian glaciers and custom geometries. This is done with a user-friendly GUI that guides the user through the required step-by-step process to generate and export the glacier area delineations, temperature median composites, and time-series charts for the different summers of interest.

8.3 3D Patagonian Glaciers Viewer (CesiumJS App)

The result of the CesiumJS web application development methodology, explained in Chapter 6, is the “**3D Patagonian Glaciers Viewer**” web application (Figure 68), available at <https://felipecamachoh.github.io/PatagonianGlaciers/3DMonitoringApp.html>. This application allows the user to visualize and compare the remote sensing outputs from the GEE web application fully in 3D and to access the time-series charts and rate of change for the glacier area, LST, and air temperature variables.

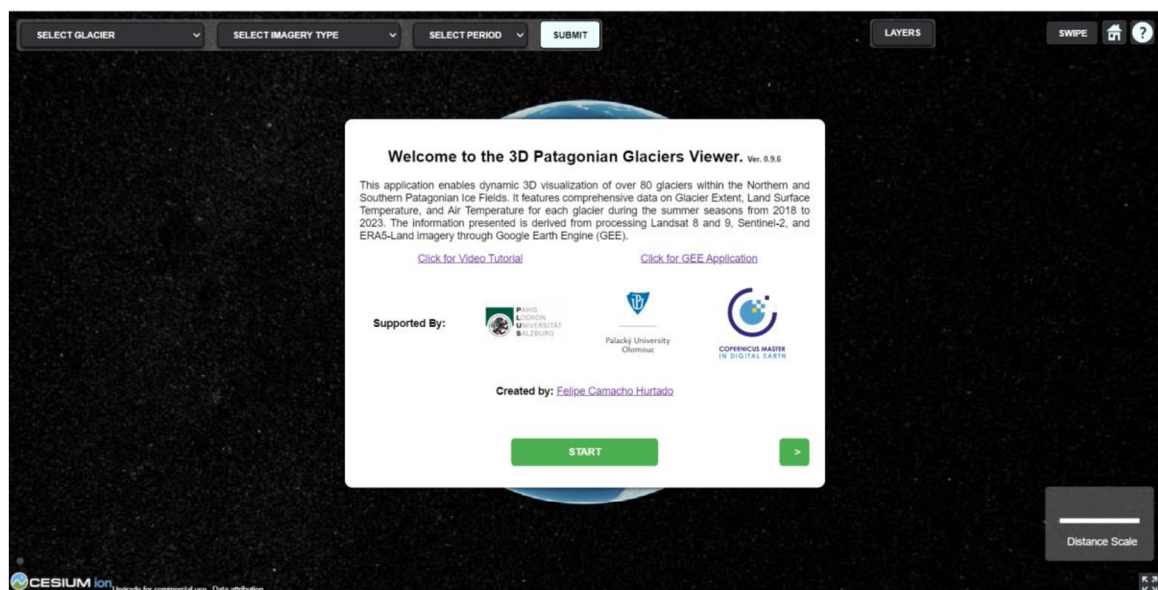


Figure 68 3D Patagonian Glaciers Viewer – Initial Screen.

The application first presents the user with a series of interactive panels that describe its purpose, capabilities, and methods of interaction. Once the users have familiarized themselves with it, they must follow a few simple steps (Figure 69) to visualize and compare the summer median composites.

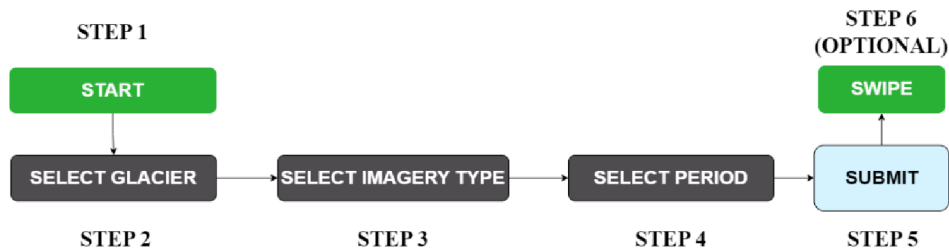


Figure 69 Operational Flowchart for 3D Patagonian Glaciers Viewer.

The first step is to click the “START” button, which will zoom the web map to the Patagonian NPI and SPI regions. Then, similar to the GEE web application, users will need to select the glacier, imagery type, and summer period of interest via the buttons in the upper left corner of the layout. Once the parameters are correctly set, by clicking the “SUBMIT” button, the corresponding imagery will be requested and added to the map. Finally, users can utilize the “SWIPE” button in the upper right corner to enable the swipe functionality and compare any of the imagery side-by-side using the divisor.

Specifically, after the user selects any of the 83 available glaciers, the application will highlight it, zoom into it, and display a sidebar (Figure 70) with the resulting time-series charts and related rate of change, as detailed in subsection 8.1. Each chart can be clicked to open in a new browser tab. Additionally, the sidebar can be closed and reopened by clicking the highlighted glacier.

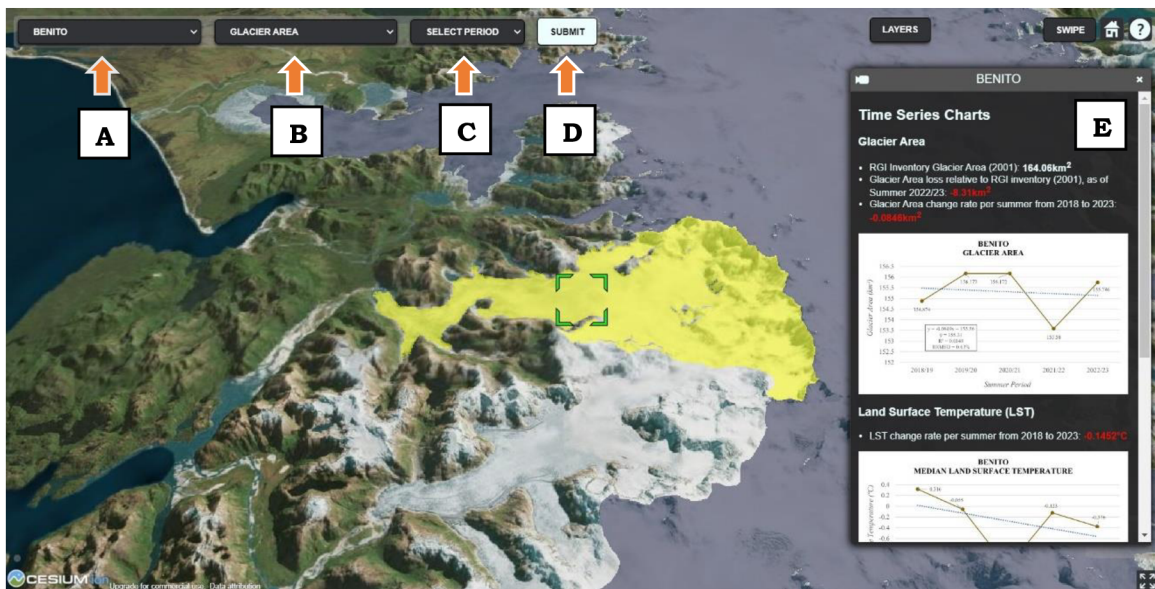


Figure 70 3D Patagonian Glaciers Viewer – Benito glacier selection. Features and buttons: Select Glacier (A), Select Imagery Type (B), Select Summer Period (C), Submit (D), and Sidebar (E).

Regarding the “SUBMIT” button functionality, it not only requests and adds the corresponding imagery based on the selected parameters but also retrieves its legend (Figure 71). For this purpose, a panel in the lower left part will dynamically display the legend for the type of imagery requested. If required, this panel can be closed or reopened by clicking the show/hide legend button.

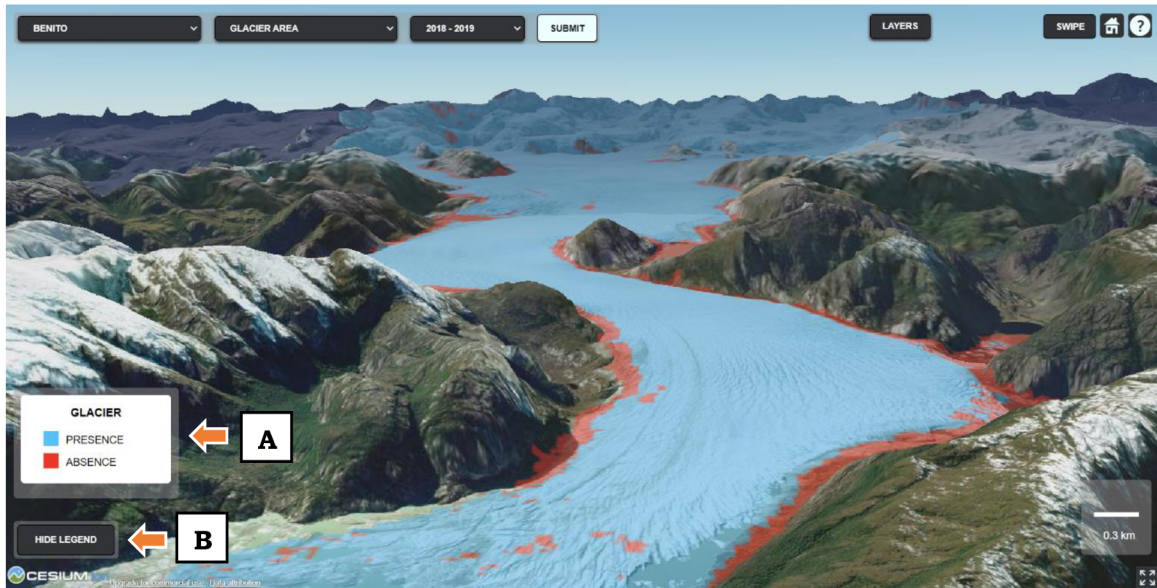


Figure 71 Patagonian Glaciers Viewer – Benito glacier area summer median composite for the 2018 – 2019 summer period. Features and buttons: Legend Panel (A) and hide-show Legend button (B).

As mentioned, the main capability of this application is the possibility to use the swipe to compare the imagery. In detail, once the user clicks on the 'SWIPE' button, it activates a divisor that can be dragged to compare the images on each side. The user can modify the layer's visibility and transparency using the display control panels in the upper right corner, which include checkboxes and sliders to visualize only the layers intended for comparison on each side. The described elements can be visualized in Figure 72.

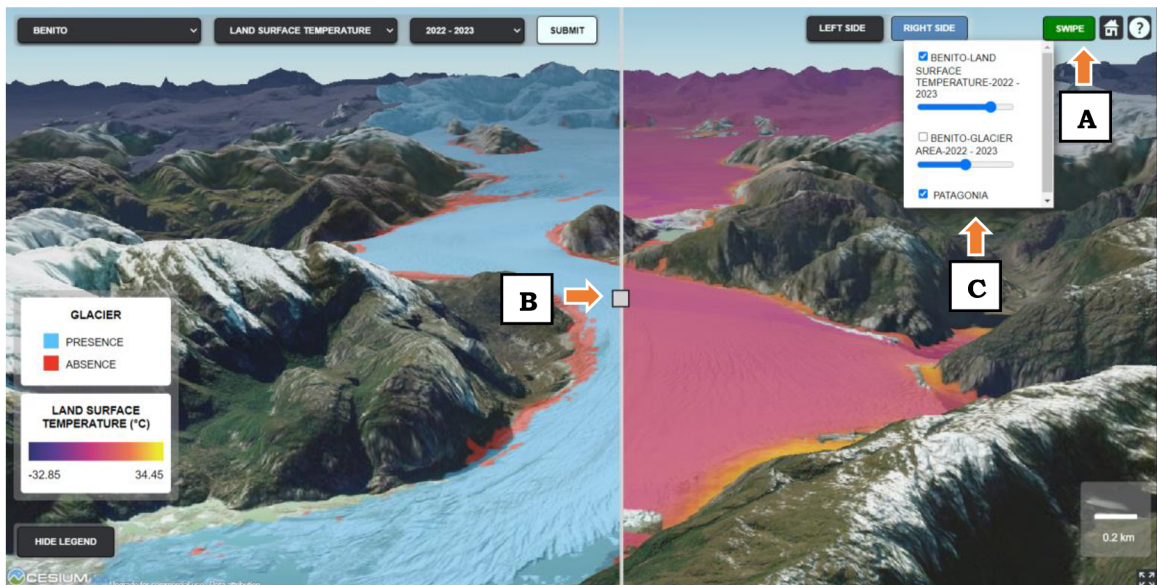


Figure 72 Patagonian Glaciers Viewer – Visualization of Benito glacier area (left side) and LST (right side) for the 2022-2023 summer period using the swipe feature. Features and Buttons: Enable Swipe (A), Swipe Divisor (B), and Display controls for the right panel (C).

Finally, the application provides a distance scale in kilometer units and the default Cesium home and navigation instructions buttons as complementary features (Figure 73). These buttons allow users to return the map view to the NPI and SPI quickly, reopen the instructive panels, and view the application controls.

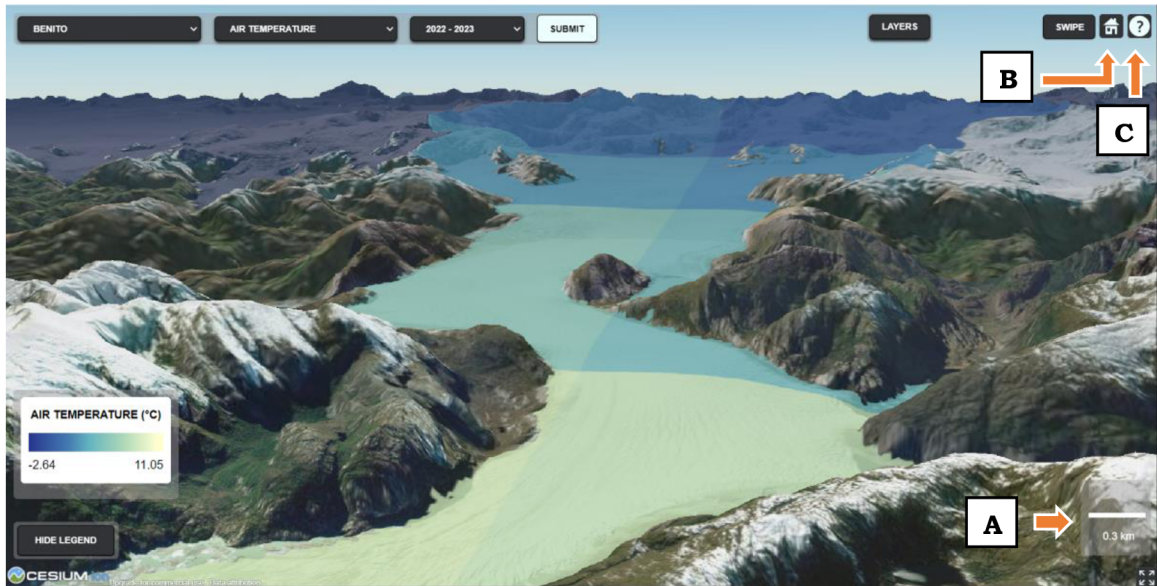


Figure 73 Patagonian Glaciers Viewer – Visualization of Benito air temperature composite for the 2022-2023 summer period. Features and Buttons: Distance Scale (A), View Home (B), and Navigation Instructions C).

8.4 Survey Review

As detailed in Section 7, a Survey123 form was created to evaluate the user experience with the GEE and CesiumJS web applications. In total, 12 anonymous responses were received, with 11 participants aged between 25 and 34 and one aged over 45.

Regarding the users' familiarity with the main topics introduced in this study, it was found that most were very familiar with Remote Sensing, Time-Series Analysis, and Google Earth Engine. Specifically, more than 50% reported being very familiar with Remote Sensing (Figure 74A) over 80% with Time-Series Analysis (Figure 74B), and 50% with Google Earth Engine (Figure 74C).

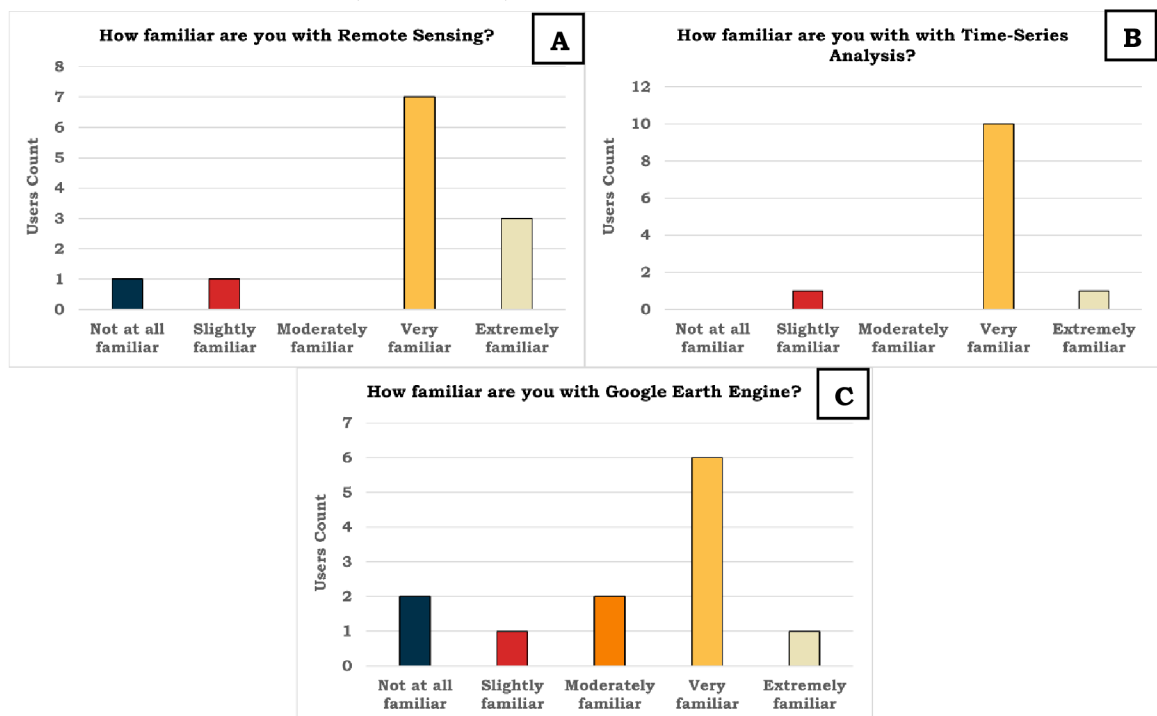


Figure 74 Users familiarity with: A) Remote Sensing. B) Time-Series Analysis. C) GEE.

In contrast, over 50% of the users were not at all familiar with Glaciology (Figure 75A) and 75% with CesiumJS (Figure 75B).

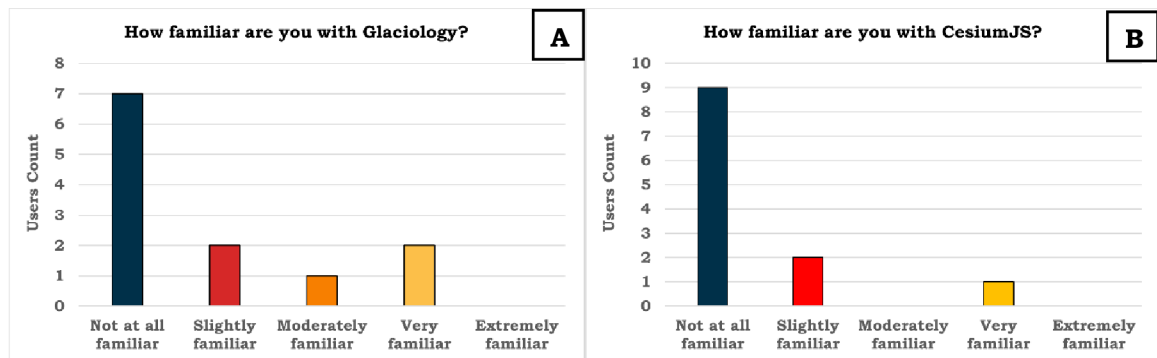


Figure 75 Users familiarity with: A) Glaciology. B) CesiumJS.

With respect to users' experience with the “**Patagonian Glacier Monitoring Application**” in terms of interface attractiveness, intuitiveness, and general performance, it was found that most of the users were highly satisfied with the interface, as seven rated it as excellent, and five as good (Figure 76A). However, for performance, although most rated it as good or excellent, two users rated it as fair (Figure 76B).



Figure 76 Patagonian Glaciers Monitoring Application. A) Interface Rating. B) Performance Rating.

Additionally, only two of the total participants reported experiencing bugs. The comments included the impossibility of generating the glacier area composite for Amalia Glacier in the 2020/21 summer period and a slow performance when generating the time-series charts. However, after testing these behaviors, it was not possible to replicate the issues.

Concerning the user's experience with the “**3D Patagonian Glaciers Viewer**” Cesium JS application, the ratings for the user interface and performance were better than those of the “Patagonian Glaciers Monitoring Application”. The participants rated the interface and performance as either good or excellent, with the interface receiving excellent responses from 75% of users (Figure 77A) and performance garnering more than 50% excellent ratings (Figure 77B). Moreover, compared with the GEE web application that received two bug reports, none of the participants evidenced unexpected behaviors in the 3D CesiumJS web application. Finally, all the contestants agreed that the 3D perspective provided by the “3D Patagonian Glaciers Viewer” application facilitated the understanding of glacier area and temperature changes in the Patagonian glaciers (Figure 77C).

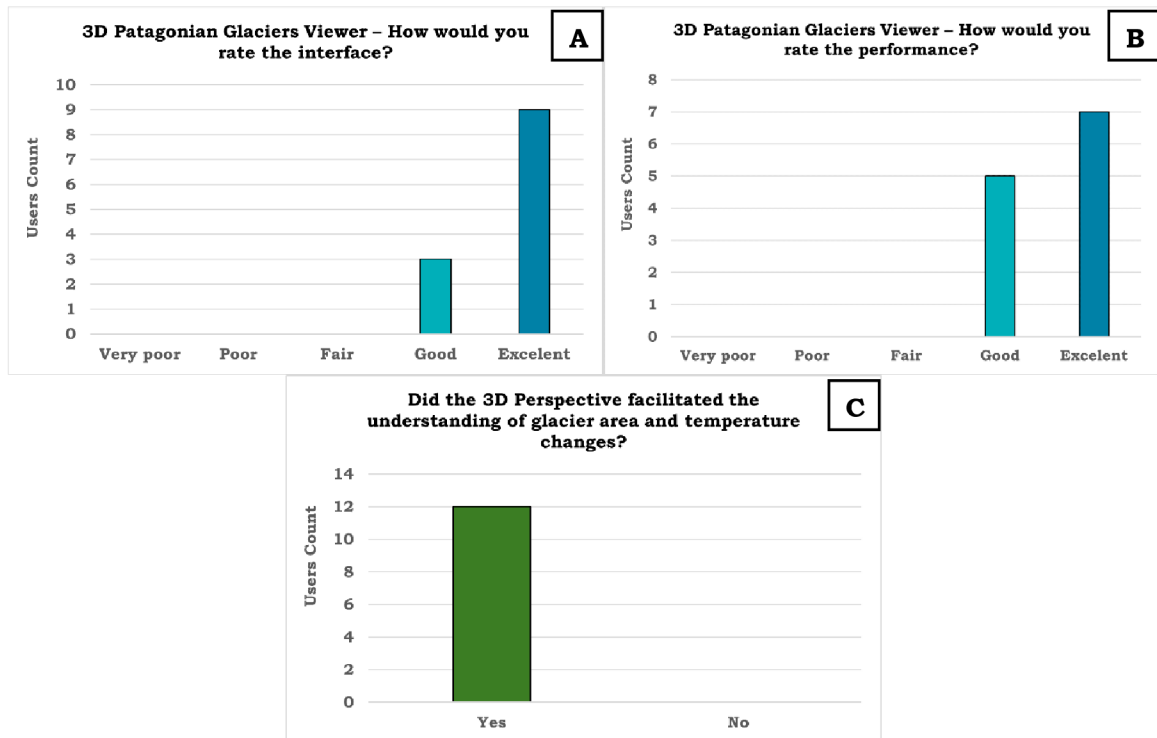


Figure 77 3D Patagonian Glaciers Viewer. A) Interface Rating. B) Performance Rating. C) Positive Influence of 3D perspective for understanding glacier changes.

Finally, from the last section of the survey, where users were asked which application they preferred for visualizing glacier area and temperature changes, as well as their level of agreement regarding the importance of ready-to-use applications as tools for scientific dissemination, it was observed that over 90% of the users tested preferred the “3D Patagonian Glaciers Viewer” CesiumJS web application over the “Patagonian Glaciers Monitoring Application” GEE web application (Figure 78).

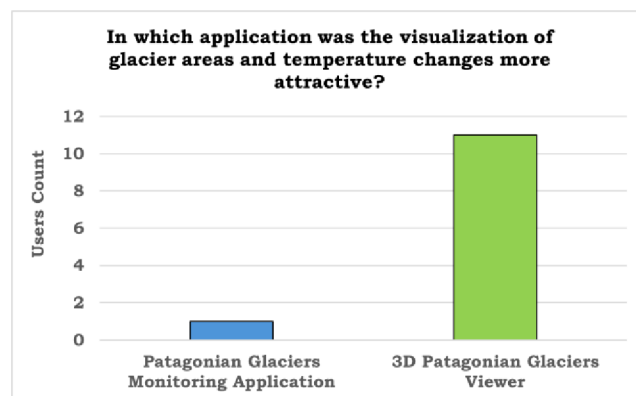


Figure 78 Preferred web application for visualizing the glacier area and temperature changes.

Furthermore, 75% of participants strongly agreed that ready-to-use applications like the ones tested provide useful tools and information for both scientific and non-scientific communities (Figure 79A) and can increase the general population's interest in Earth's dynamics, such as glacier area and temperature changes (Figure 79B).

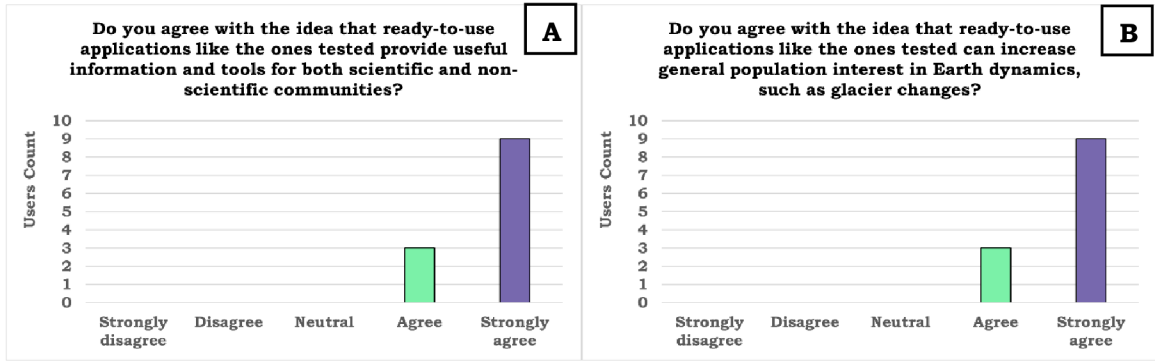


Figure 79 A) User Agreement on the Utility of Ready-to-Use Applications for Scientific and Non-Scientific Communities. B) User Agreement on the Potential of Ready-to-Use Applications to Engage the General Public in Earth Dynamics

9 DISCUSSION

This chapter will present and discuss the potential of cloud computing platforms, specifically GEE, for environmental research using EO data and the limitations of the time-series analysis methodology. Moreover, it will discuss the main challenges, advantages, and limitations of the GEE and CesiumJS web applications and the contribution of this study to the knowledge of glacier dynamics in the Patagonian Region.

Potential of GEE for Environmental Research

Over the past few decades, EO data and remote sensing techniques have been widely used for various topics, including water management, disaster risk assessment, land use mapping, and climate monitoring. The traditional approach involved searching for, finding, and downloading the data locally, which required significant storage space. Moreover, once the data was downloaded, only a few images could be processed simultaneously due to the high computational demands, leading end-users to spend hundreds of hours analyzing a limited amount of data. To overcome these limitations, cloud computing platforms, such as GEE, have started to be used as they provide high processing power and the possibility of accessing EO data in the cloud without requiring downloading any data locally.

In this study, GEE proved to be a crucial cloud computing platform for environmental research and time-series analysis, as it allowed the collection and integration of hundreds of satellite images from different satellite missions, such as Sentinel and Landsat, into processing workflows involving the creation of median composites and calculations of remote sensing indices such as NDSI and NDWI. These same processing operations can be done in ArcGIS, ENVI, and PCI Geomatic software. However, with a few lines of code in GEE, it was possible to rapidly retrieve the mentioned imagery, perform the indices and median operations, and visualize the results. Even though users are becoming more familiar with this cloud computing platform, as evidenced in the survey results, its full potential has not been uncovered due to the required JS coding skills, which are seen as an impediment for non-coding users. Nevertheless, plenty of official information and tutorials can guide the user in the initial approach to GEE, and even more, with trending AI platforms such as ChatGPT, users can get customized support to be introduced to GEE and take advantage of its capabilities.

In synthesis, GEE is currently one of the most important cloud computing platforms for EO studies, leading the development of time-series analyses that were impossible before. It has opened the possibility of taking 20, 30, or more years of satellite data into consideration for scientific analysis, which will be important for identifying trends and addressing upcoming environmental challenges, such as climate change, water scarcity, and glacier retreats.

Limitations and Error Sources of the Time-Series Analysis Methodology

The methodology used for the Time Series Analysis within GEE, utilizing Sentinel 2, Landsat 8 and 9, and ERA5 Land imagery, has a strong theoretical background. It was designed based on existing, well-proven methodologies implemented to identify glacier area and temperature changes, considering the widely used NDSI and NDWI as main classifiers of glacier and non-glacier pixels. Given that the referenced studies primarily utilized Landsat imagery, this study aimed to take advantage of the higher pixel resolution of Sentinel and available Landsat imagery by working in conjunction with data from both

satellite missions. This approach, which has been previously validated, increased data availability for the summer periods of interest. However, it might have introduced overestimations and underestimations of the obtained values due to differences in spectral resolution and sensor calibrations. Moreover, even though the clouds were masked, as usual in remote sensing data and studies, glacier area and temperature values may have been influenced by remnant cloud and shadow pixels. Furthermore, the misclassification of snow or water pixels by the applied thresholds for the NDSI and NDWI could also have influenced the results.

From the time-series analysis, the main contribution was estimating glacier area and temperature changes and generating median composites and time-series charts. However, due to time limitations, the lack of ground stations and in-situ data, the extensive number of glaciers studied, and a project focus on visualization over analysis of results, a comprehensive accuracy assessment was not conducted for the obtained values, except for the time-series charts. As a result, even though the findings indicate a significant retreat of glacier areas and show the changes in LST and air temperature, these values cannot be considered accurate without further validation, which limits their usage and discussion in current glaciology research. Regarding the accuracy assessment for the rate of change, it was evident that the values obtained for some glaciers are not representative, as they exhibit low R^2 and high RMSD or RRMSD.

Despite these limitations, the methodology implemented provides valuable insights into the current and recent changes in glacier areas and temperatures and ready-to-use products that can be incorporated into further research after validation.

Insights and Challenges of the GEE Web Application

When developing the “Patagonian Glaciers Monitoring Application” within GEE, the goal was not only to design a tool capable of creating, visualizing, and exporting summer median composites and time-series charts for the Patagonian glaciers but also to make it attractive, user-friendly, and as simple as possible. This was motivated by the fact that most of the available GEE web applications lack an attractive and modern design and are unnecessarily complex, expecting the user to perform a series of steps without guidance. As a result, significant resources were dedicated to creating the best GUI, including testing different layouts and familiarizing with widgets and CSS concepts. This represented a major challenge, as there was no perfect solution for the layout design but rather trial and error, which resulted in constant layout modifications to adapt new capabilities or enhance user interactivity. The amount of effort can be evidenced not only in the GEE web application itself but also in the results from the survey, where more than 50% of the users rated the interface as excellent.

Compared with code implementations without a GUI, the main advantage of this application is that the user does not need to be familiar with JS, as all functionalities are performed interactively using buttons or selectors. In this way, the barriers between scientific and non-scientific communities are removed, as all users, regardless of their expertise, can interact with the application and gain insights into the status of Patagonian glaciers. Another advantage is that the code implementation is publicly available, meaning anyone can customize it by adding new widgets and image collections, modifying the NDSI or NDWI thresholds, or changing the AOI. In summary, the application has great potential to provide time-series outputs for glacier analysis but can be modified to address land cover changes, flood mapping, or additional topics where time-series can be generated.

Regarding the current limitations of the application, the download of the summer median composites is restricted due to GEE's design to a maximum of 32 MB or an extent of 400 km² using a 10 m pixel size. This limitation specifically affects the download process through the GUI when accessing the application via the public link and not through the code editor, which, in that case, allows the imagery to be downloaded to the user's Google Drive account without size restrictions. Moreover, as it is a cloud-hosted application, it requires an internet connection to be used, and its performance will depend on the user's internet speed. However, regardless of the connection, the application proved to perform well, as evidenced by the survey.

Achievements and Challenges of 3D Web Development with CesiumJS

The objective of providing a 3D visualization for the Patagonian glaciers was to attract the casual public and introduce them to the ongoing glacier changes by generating a visual impact through an interactive high-resolution experience. Moreover, for the scientific community, the goal was to allow the comparison of glacier areas and temperature changes over time, and provide visual information on the height of each glacier, which is important as it influences area retreat and temperature changes. Having the objectives defined, selecting the 3D visualization methods was not straightforward; different software, platforms, and JS libraries were considered for creating a 3D visualization, including ArcGIS Online, Blender, and ThreeJS. Indeed, CesiumJS was not an option, mainly due to unfamiliarity with it, supported by the survey results, in which it was observed that 75% of the users were not familiar at all with this JS library.

CesiumJS and Cesium Ion proved to be outstanding tools for storing and visualizing 3D data on the web. With them, the “3D Patagonian Glaciers Viewer” application was developed, providing an interactive 3D visualization with high-resolution terrain of the glacier area and temperature data for the NPI and SPI glaciers. As with the GEE application, considerable resources were dedicated to creating an attractive user interface and ensuring good performance. Since the imagery was compressed before being uploaded to Cesium Ion, the application can run at more than 30 FPS.

The main challenge of working with CesiumJS was the steep learning curve, as it required becoming familiar with the viewer and entity concepts. Moreover, the inability to modify the symbology of the imagery after it was uploaded required adjusting the imagery processing steps. Nevertheless, the official documentation and available sandcastles provided enough information and coding examples to develop the application. It must be mentioned that the code implementation was constantly debugged using ChatGPT 4.

Contribution to glaciological knowledge and future research

This study contributed to glaciological knowledge by generating time-series outputs, estimating glacier areas and temperature changes for the NPI and SPI glaciers, and promoting interest in glaciers for the general population. It is expected that the developed web applications, specifically the 3D CesiumJS, will grab the attention of multiple users, encouraging them to continue studying these natural features. Furthermore, the open-source nature of the applications and the possibility of adding new functionalities and datasets over the existing ones will incentivize the improvement of such tools. In future research, the main goal will be to assess the accuracy of the time-series results and extend the usability of the applications for more glacier regions worldwide.

10 CONCLUSION

Glaciers are considered among the most important natural features as they provide ecosystem services such as water provision, flood mitigation, and biodiversity conservation. Moreover, as complex ecosystems, they are accurate indicators of climate variability. Glaciers worldwide have shown significant area retreats and temperature increases in the last few years, which has motivated research on ongoing glacier dynamics. Despite the increase in glaciology research, glacierized regions such as the Patagonian Andes are still poorly known due to harsh access conditions and disinterest from international scientific communities. In particular, the Patagonian Andes is a critical region, as it is the largest glacierized area in South America, with over 20000 km², distributed mainly between the NPI and SPI. In this context, EO data and techniques, including satellite imagery, cloud computing platforms, and 3D visualization methods, have great potential to overcome the lack of studies and promote interest in these natural ecosystems for both scientific and non-scientific communities.

Motivated by the mentioned context, this diploma thesis focused on developing a GEE web application that allows the creation, visualization, and export of remote-sensing and time series products for the Patagonian region. Moreover, using this application, the goal was to conduct a time-series analysis of glacier area, LST, and air temperature changes for the NPI and SPI glaciers between the 2018 and 2023 summer periods, using Landsat 8-9, Sentinel-2, and ERA5-Land Imagery. Furthermore, the thesis aimed to develop a 3D web application to visualize, interact, and compare the remote sensing and time-series products obtained from the GEE web application. Lastly, it evaluated the user experience with both web applications.

The resulting GEE web application proved to serve its purpose, as it allows users to generate time-series outputs and median summer composites for 83 Patagonian glaciers through an attractive and user-friendly GUI. From this application, 1245 summer composites and 249 time-series charts were generated to evaluate the rate of change of glacier area, LST, and air temperature for the mentioned glaciers, evidencing a significant glacier area retreat and temperature increases overall while also providing detailed information for each glacier independently.

Regarding the 3D web application developed using CesiumJS, it provides a fully 3D interactive and high-resolution experience where users can use the swipe and sidebar widgets to visualize, compare, and assess the ongoing Patagonian glacier changes. Moreover, it demonstrated the potential and advantages of a 3D perspective over the classic 2D web approach to generate impact and grab the general population's attention in scientific discussions.

In conclusion, the time-series methodology and web applications proposed and developed in this study are a major step toward improving the glaciology knowledge of the Patagonian region. They evidenced the hidden potential of GEE and 3D visualizations for scientific dissemination and the importance of GUI design when creating attractive web experiences. Furthermore, as the source code for both GEE and CesiumJS web applications is publicly available, the users will be able to extend their functionalities by introducing new data, adding widgets, or changing the AOI. It is expected that with the outputs generated from this study, scientific and non-scientific communities will gain awareness of the importance of the glaciers and their ongoing changes. The next steps will be to validate the accuracy of the time-series outputs and to continue updating the application considering the upcoming summer periods.

REFERENCES AND INFORMATION SOURCES

- Ali, A., Dunlop, P., Coleman, S., Kerr, D., McNabb, R. W., & Noormets, R. (2023). Glacier area changes in Novaya Zemlya from 1986–89 to 2019–21 using object-based image analysis in Google Earth Engine. *Journal of Glaciology*, 69(277), 1305-1316. <https://doi.org/10.1017/jog.2023.18>
- Amani, M., Ghorbanian, A., Ahmadi, S. A., Kakooei, M., Moghimi, A., Mirmazloumi, S. M., ... & Brisco, B. (2020). Google earth engine cloud computing platform for remote sensing big data applications: A comprehensive review. *IEEE Journal of Selected Topics in Applied Earth Observations and Remote Sensing*, 13, 5326-5350. <https://doi.org/10.1109/JSTARS.2020.3021052>
- Aniya, M., Sato, H., Naruse, R., Skvarca, P., & Casassa, G. (1997). Recent Glacier Variations in the Southern Patagonia Icefield, South America. *Arctic and Alpine Research*, 29(1), 1–12. <https://doi.org/10.2307/1551831>
- Arif, H., Mehmood, S. A., & Ahmad, H. H. (2021). Appraisal of Spatiotemporal Variations in Snow Cover Dynamics using Geospatial Techniques: A paradigm from Gilgit-Baltistan, Pakistan. <https://doi.org/10.33411/IJIST/2020020408>
- Bates, J. S. (2020). Oblique UAS Imagery and Point Cloud Processing for 3D Rock Glacier Monitoring, Available online: <https://run.unl.pt/bitstream/10362/94396/1/TGEO0234.pdf>
- Bazilova, V., & Kääh, A. (2022). Mapping area changes of glacial lakes using stacks of optical satellite images. *Remote Sensing*, 14(23), 5973. <https://doi.org/10.3390/rs14235973>
- Beltramone, G., Scavuzzo, M., German, A., & Ferral, A. (2020). Wet snow detection in Patagonian Andes with Sentinel-1 SAR temporal series analysis in GEE. In 2020 IEEE Congreso Bienal de Argentina (ARGENCON) (pp. 1-8). IEEE. <https://doi.org/10.1109/ARGENCON49523.2020.9505487>
- Blaschke, T. (2010). Object based image analysis for remote sensing. *ISPRS journal of photogrammetry and remote sensing*, 65(1), 2-16. <https://doi.org/10.1016/j.isprsjprs.2009.06.004>
- Bravo Lechuga, C. A. (2020). Response of the Patagonian Glaciers to Present and Future Atmospheric Changes (Doctoral dissertation, University of Leeds).
- Carrasco-Escaff, T., Rojas, M., Garreaud, R. D., Bozkurt, D., & Schaefer, M. (2023). Climatic control of the surface mass balance of the Patagonian Icefields. *The Cryosphere*, 17(3), 1127-1149. <https://doi.org/10.5194/tc-17-1127-2023>
- Cesium. (n.d). Bing Maps Aerial Imagery. Retrieved March 26, 2024, from <https://cesium.com/platform/cesium-ion/content/bing-maps-imagery/>

- Cesium. (n.d). Cesium World Terrain. Retrieved March 26, 2024, from <https://cesium.com/platform/cesium-ion/content/cesium-world-terrain/>
- Cho, J., Kim, C., Lim, K. J., Kim, J., Ji, B., & Yeon, J. (2023). Web-based agricultural infrastructure digital twin system integrated with GIS and BIM concepts. *Computers and Electronics in Agriculture*, 215, 108441. <https://doi.org/10.1016/j.compag.2023.108441>
- Cogley, J. G., Arendt, A. A., Bauder, A., Braithwaite, R. J., Hock, R., Jansson, P., Kaser, G., Moller, M., Nicholson, L., Rasmussen, L. A., & Zemp, M. (2010). Glossary of glacier mass balance and related terms. (IHP-VII Technical Documents in Hydrology). International Hydrological Programme. Available online: https://pure.manchester.ac.uk/ws/portalfiles/portal/53855620/Glossary_of_glacier_mass_balance.pdf
- Cook, K. H., Yang, X., Carter, C. M., & Belcher, B. N. (2003). A modeling system for studying climate controls on mountain glaciers with application to the Patagonian Icefields. *Climatic Change*, 56, 339-367. <https://doi.org/10.1023/A:1021772504938>
- Copé de los Mozos, R. (2014). Cálculo del retroceso glaciar en Isla Livingston y de su línea de costa para actualización de cartografía. Available online: <https://docta.ucm.es/entities/publication/0528b7f9-c031-455b-9b91-6d116c409f40>
- Coronato, F. R. (2020). Geographical singularities of the Patagonian climate. *Lizards of Patagonia: Diversity, Systematics, Biogeography and Biology of the Reptiles at the End of the World*, 43-58. https://doi.org/10.1007/978-3-030-42752-8_3
- Davies, B., Bendle, J., Glasser, N., García, J. L., & Kaplan, M. (2023). Glaciation and climate change in the Andean Cordillera. *Frontiers in Earth Science*, 11, 1129795. <https://doi.org/10.3389/feart.2023.1129795>
- De Vries, M. V. W., Romero, M., Penprase, S. B., Ng, G. H. C., & Wickert, A. D. (2023). Increasing rate of 21st century volume loss of the Patagonian Icefields measured from proglacial river discharge. *Journal of Glaciology*, 69(277), 1187-1202. <https://doi.org/10.1017/jog.2023.9>
- Despotovic, M., Nedic, V., Despotovic, D., & Cvetanovic, S. (2016). Evaluation of empirical models for predicting monthly mean horizontal diffuse solar radiation. *Renewable and Sustainable Energy Reviews*, 56, 246-260. <https://doi.org/10.1016/j.rser.2015.11.058>
- Di Tullio, M., Nocchi, F., Camplani, A., Emanuelli, N., Nascetti, A., & Crespi, M. (2018). Copernicus big data and google earth engine for glacier surface velocity field

monitoring: Feasibility demonstration on san rafael and san quintin glaciers. The International Archives of the Photogrammetry, Remote Sensing and Spatial Information Sciences, 42, 289-294. <https://doi.org/10.5194/isprs-archives-XLII-3-289-2018>

Dozier, J. (1989). Spectral signature of alpine snow cover from the Landsat Thematic Mapper. *Remote sensing of environment*, 28, 9-22. [https://doi.org/10.1016/0034-4257\(89\)90101-6](https://doi.org/10.1016/0034-4257(89)90101-6)

ECMWF. (n.d). ERA5-Land. Retrieved March 26, 2024, from <https://www.ecmwf.int/en/era5-land>

Ermida, S. L., Soares, P., Mantas, V., Göttsche, F. M., & Trigo, I. F. (2020). Google earth engine open-source code for land surface temperature estimation from the landsat series. *Remote Sensing*, 12(9), 1471. <https://doi.org/10.3390/rs12091471>

European Space Agency. (n.d.). Sentinel-2 operations. Retrieved March 26, 2024, from https://www.esa.int/Enabling_Support/Operations/Sentinel-2_operations

Farkas, G. (2017). Applicability of open-source web mapping libraries for building massive Web GIS clients. *Journal of Geographical Systems*, 19(3), 273-295. <https://doi.org/10.1007/s10109-017-0248-z>

Florath, J., Keller, S., Staub, G., & Weinmann, M. (2021). Optical remote sensing for glacier monitoring with respect to different snow and ice types: A case study for the Southern Patagonian Icefield. In 2021 11th Workshop on Hyperspectral Imaging and Signal Processing: Evolution in Remote Sensing (WHISPERS) (pp. 1-5). IEEE. <https://doi.org/10.1109/WHISPERS52202.2021.9484055>

Flückiger, F. T. (2022). The influence of a diverging color scheme on the representation of rock glacier dynamics in 3D animations (Master's thesis, University of Zurich). Available online: https://www.zora.uzh.ch/id/eprint/235279/1/Thesis_Flueckiger.pdf

Gede, M. (2018). Using Cesium for 3D Thematic Visualisations on the Web. <https://doi.org/10.5194/ica-proc-1-45-2018>

Genzano, N., Pergola, N., & Marchese, F. (2020). A Google Earth Engine tool to investigate, map and monitor volcanic thermal anomalies at global scale by means of mid-high spatial resolution satellite data. *Remote Sensing*, 12(19), 3232. <https://doi.org/10.3390/rs12193232>

- Google. (n.d). ERA5-Land Monthly Aggregated - ECMWF Climate Reanalysis. Retrieved March 26, 2024, from https://developers.google.com/earth-engine/datasets/catalog/ECMWF_ERA5_LAND_MONTHLY_AGGR#bands
- Google. (n.d). Scale. Retrieved April 4, 2024, from <https://developers.google.com/earth-engine/guides/scale>.
- Hajek, P., Jedlička, K., & Čada, V. (2016). Principles of cartographic design for 3d maps–focused on urban areas. In Proceedings, 6th International Conference on Cartography and GIS (pp. 297-307). Sofia, Bulgaria: Bulgarian Cartographic Association. Available online: https://www.researchgate.net/profile/Temenoujka-Bandrova/publication/309772611_6th_International_Conference_on_Cartography_and_GIS/links/5d13644a299bf1547c7f9906/6th-International-Conference-on-Cartography-and-GIS.pdf#page=297
- Hájek, P., Jedlička, K., & Čada, V. (2018). Proposal of experiments for evaluation of cartographic principles on virtual 3D maps of urban areas. In Proceedings of the 7th international conference on cartography and GIS (pp. 481-489). Bulgarian Cartographic Association. Available online: [https://iccgis2018.cartography-gis.com/7ICCGIS_Proceedings/7_ICCGIS_2018%20\(54\).pdf](https://iccgis2018.cartography-gis.com/7ICCGIS_Proceedings/7_ICCGIS_2018%20(54).pdf)
- Hall, D. K., Riggs, G. A., & Salomonson, V. V. (1995). Development of methods for mapping global snow cover using moderate resolution imaging spectroradiometer data. *Remote sensing of Environment*, 54(2), 127-140. [https://doi.org/10.1016/0034-4257\(95\)00137-P](https://doi.org/10.1016/0034-4257(95)00137-P)
- He, B., Mo, W. X., Hu, J. X., Yang, G., Lu, G. J., & Liu, Y. Q. (2016). Development of power grid Web3D GIS based on Cesium. In 2016 IEEE PES Asia-Pacific Power and Energy Engineering Conference (APPEEC) (pp. 2465-2469). IEEE. <https://doi.org/10.1109/APPEEC.2016.7779930>
- Huang, L., Li, Z., Zhou, J. M., & Zhang, P. (2021). An automatic method for clean glacier and nonseasonal snow area change estimation in High Mountain Asia from 1990 to 2018. *Remote Sensing of Environment*, 258, 112376. <https://doi.org/10.1016/j.rse.2021.112376>
- Jedlička, K., & Hájek, P. (2020). Does 3D GIS provide a different insight than 2D?. In 8th International Conference on Cartography and GIS, Nessebar, Bulgaria. Available online: [https://iccgis2020.cartography-gis.com/8ICCGIS-Vol1/8ICCGIS_Proceedings_Vol1_\(69\).pdf](https://iccgis2020.cartography-gis.com/8ICCGIS-Vol1/8ICCGIS_Proceedings_Vol1_(69).pdf)
- Kääb, A. (2011). Natural hazards associated with glaciers and permafrost. Singh VP Singh P and Haritashya UK eds. *Encyclopedia of earth sciences series*. Dordrecht: Springer Netherlands, 763-775. https://doi.org/10.1007/978-90-481-2642-2_368

- Kang, X., Li, J., & Fan, X. (2018). Spatial-temporal visualization and analysis of earth data under Cesium Digital Earth Engine. In Proceedings of the 2018 2nd International Conference on Big Data and Internet of Things (pp. 29-32). <https://doi.org/10.1145/3289430.3289447>
- Karunasingha, D. S. K. (2022). Root mean square error or mean absolute error? Use their ratio as well. *Information Sciences*, 585, 609-629. <https://doi.org/10.1016/j.ins.2021.11.036>
- Keshri, A. K., Shukla, A., & Gupta, R. P. (2009). ASTER ratio indices for supraglacial terrain mapping. *International Journal of Remote Sensing*, 30(2), 519-524. <https://doi.org/10.1080/01431160802385459>
- Kumar, L., & Mutanga, O. (2018). Google Earth Engine applications since inception: Usage, trends, and potential. *Remote sensing*, 10(10), 1509. <https://doi.org/10.3390/rs10101509>
- La Guardia, M., Koeva, M., D'ippolito, F., & Karam, S. (2022). 3D Data integration for web based open source WebGL interactive visualisation. In 17th 3D GeoInfo Conference (pp. 89-94). <https://doi.org/10.5194/isprs-archives-XLVIII-4-W4-2022-89-2022>
- Leskens, J.G., Kehl, C., Tutenel, T. et al. An interactive simulation and visualization tool for flood analysis usable for practitioners. *Mitig Adapt Strateg Glob Change* 22, 307–324 (2017). <https://doi.org/10.1007/s11027-015-9651-2>
- Li, X., Wang, N., & Wu, Y. (2022). Automated Glacier Snow Line Altitude Calculation Method Using Landsat Series Images in the Google Earth Engine Platform. *Remote Sensing*, 14(10), 2377. <https://doi.org/10.3390/rs14102377>
- Lindsay, E., Frauenfelder, R., R  ther, D., Nava, L., Rubensdotter, L., Strout, J., & Nordal, S. (2022). Multi-temporal satellite image composites in google earth engine for improved landslide visibility: A case study of a glacial landscape. *Remote Sensing*, 14(10), 2301. <https://doi.org/10.3390/rs14102301>
- Liu, X., Hu, G., Chen, Y., Li, X., Xu, X., Li, S., ... & Wang, S. (2018). High-resolution multi-temporal mapping of global urban land using Landsat images based on the Google Earth Engine Platform. *Remote sensing of environment*, 209, 227-239. <https://doi.org/10.1016/j.rse.2018.02.055>
- Manquehual-Cheuque, F., & Somos-Valenzuela, M. (2021). Climate change refugia for glaciers in Patagonia. *Anthropocene*, 33, 100277. <https://doi.org/10.1016/j.ancene.2020.100277>
- Maussion, F., Hock, R., Paul, F., Raup, B., Rastner, P., Zemp, M, Andreassen, L., Barr, I., Bolch, T., Kochtitzky, W., McNabb, R. & Tielidze, L. (2023) The Randolph Glacier Inventory version 7.0 User guide v1.0. <https://doi.org/10.5281/zenodo.8362857>.

- McDonnell, M., Rupper, S., & Forster, R. (2022). Quantifying geodetic mass balance of the northern and Southern Patagonian Icefields since 1976. *Frontiers in Earth Science*, 10, 813574. <https://doi.org/10.3389/feart.2022.813574>
- McFEETERS, S. K. (1996). The use of the Normalized Difference Water Index (NDWI) in the delineation of open water features. *International Journal of Remote Sensing*, 17(7), 1425–1432. <https://doi.org/10.1080/01431169608948714>
- Meier, W. J. H., Griesinger, J., Hochreuther, P., & Braun, M. H. (2018). An updated multi-temporal glacier inventory for the Patagonian Andes with changes between the Little Ice Age and 2016. *Frontiers in Earth Science*, 6, 62. <https://doi.org/10.3389/feart.2018.00062>
- Mete, M. O., Guler, D., & Yomralioglu, T. (2018). Development of 3D web GIS application with open source library. *Selçuk Üniversitesi Mühendislik, Bilim Ve Teknoloji Dergisi*, 6, 818-824. <https://doi.org/10.15317/Scitech.2018.171>
- Minowa, M., Schaefer, M., Sugiyama, S., Sakakibara, D., & Skvarca, P. (2021). Frontal ablation and mass loss of the Patagonian icefields. *Earth and Planetary Science Letters*, 561, 116811. <https://doi.org/10.1016/j.epsl.2021.116811>
- Morelli, T. L., Daly, C., Dobrowski, S. Z., Dulen, D. M., Ebersole, J. L., Jackson, S. T., ... & Beissinger, S. R. (2016). Managing climate change refugia for climate adaptation. *PloS one*, 11(8), e0159909. <https://doi.org/10.1371/journal.pone.0159909>
- NASA. (n.d). Landsat 8. Retrieved March 26, 2024, from <https://landsat.gsfc.nasa.gov/satellites/landsat-8/>
- Parisi, T. (2012). WebGL: up and running. " O'Reilly Media, Inc.". Available online: <https://www.oreilly.com/library/view/webgl-up-and/9781449326487/>
- Paul, F., Kääb, A., Maisch, M., Kellenberger, T., & Haeberli, W. (2002). The new remote-sensing-derived Swiss glacier inventory: I. Methods. *Annals of Glaciology*, 34, 355-361. <https://doi.org/10.3189/172756402781817941>
- Pellicciotti, F., Ragetti, S., Carenzo, M., & McPhee, J. (2014). Changes of glaciers in the Andes of Chile and priorities for future work. *Science of the Total Environment*, 493, 1197-1210. <https://doi.org/10.1016/j.scitotenv.2013.10.055>
- Pelto, M. S., & Riedel, J. (2001). Spatial and temporal variations in annual balance of North Cascade glaciers, Washington 1984–2000. *Hydrological Processes*, 15(18), 3461-3472. <https://doi.org/10.1002/hyp.1042>

- Potnis, A., & Durbha, S. S. (2016). Exploring Visualization of Geospatial Ontologies using Cesium. In VOILA@ ISWC (pp. 143-150). Available online: <https://www.diva-portal.org/smash/get/diva2:1033953/FULLTEXT02#page=151>
- Qu, G., He, J., & Wang, J. (2023). Village Web 3D Visualization System Based on Cesium. In International Conference on Spatial Data and Intelligence (pp. 89-100). Cham: Springer Nature Switzerland. https://doi.org/10.1007/978-3-031-32910-4_6
- Rignot, E. & Rivera, Andrés & Casassa, Gino. (2003). Contribution of the Patagonia Icefields of South America to Global Sea Level Rise. *Science (New York, N.Y.)*. 302. 434-7. <https://doi.org/10.1126/science.1087393>
- Rivera, A., & Casassa, G. (2004). Ice elevation, areal, and frontal changes of glaciers from National Park Torres del Paine, Southern Patagonia Icefield. *Arctic, Antarctic, and Alpine Research*, 36(4), 379-389. [https://doi.org/10.1657/1523-0430\(2004\)036\[0379:IEAAFC\]2.0.CO;2](https://doi.org/10.1657/1523-0430(2004)036[0379:IEAAFC]2.0.CO;2)
- Rivera, A., Bown, F., Wendt, A., & Bravo, C. (2012). Recent glacier changes in Southern Chile and in the Antarctic Peninsula. In *Anales del Instituto de la Patagonia*. Universidad de Magallanes. Available online: <https://www.scielo.cl/pdf/ainpat/v40n1/art03.pdf>
- Rivera, A., Aravena, J.C., Urra, A., Reid, B. (2023). Chilean Patagonian Glaciers and Environmental Change. In: Castilla, J.C., Armesto Zamudio, J.J., Martínez-Harms, M.J., Tecklin, D. (eds) *Conservation in Chilean Patagonia*. Integrated Science, vol 19. Springer, Cham. https://doi.org/10.1007/978-3-031-39408-9_15
- Sáez, N., Staub, G., & Abarca-del-Río, R. (2019). Monitoring Glacier Retreat in the Chilean Southern Patagonian Ice Field. In *IGARSS 2019-2019 IEEE International Geoscience and Remote Sensing Symposium* (pp. 4169-4171). IEEE. <https://doi.org/10.1109/IGARSS.2019.8899295>
- Sagredo, E. A., & Lowell, T. V. (2012). Climatology of Andean glaciers: A framework to understand glacier response to climate change. *Global and Planetary Change*, 86, 101-109. <https://doi.org/10.1016/j.gloplacha.2012.02.010>
- Schanche, A. (2020). Geospatial Laboratory Visualization: Geospatial Laboratory Visualization. Available online: <https://uu.diva-portal.org/smash/get/diva2:1395224/FULLTEXT01.pdf>
- Scheip, C. M., & Wegmann, K. W. (2021). HazMapper: a global open-source natural hazard mapping application in Google Earth Engine. *Natural Hazards and Earth System Sciences*, 21(5), 1495-1511. <https://doi.org/10.5194/nhess-21-1495-2021>

- Scianna, A., & La Guardia, M. (2018). Globe based 3D GIS solutions for virtual heritage. *The International Archives of the Photogrammetry, Remote Sensing and Spatial Information Sciences*, 42, 171-177. <https://doi.org/10.5194/isprs-archives-XLII-4-W10-171-2018>
- Shivam, P., & Narayan, P. (2023, October). 3D Visualization of Terrain Surface for Enhanced Spatial Mapping and Analysis. In *IFIP International Internet of Things Conference* (pp. 49-63). Cham: Springer Nature Switzerland. https://doi.org/10.1007/978-3-031-45882-8_4
- Shugar, D. H., Burr, A., Haritashya, U. K., Kargel, J. S., Watson, C. S., Kennedy, M. C., ... & Strattman, K. (2020). Rapid worldwide growth of glacial lakes since 1990. *Nature Climate Change*, 10(10), 939-945. <https://doi.org/10.1038/s41558-020-0855-4>
- Smith, W. D., Dunning, S. A., Brough, S., Ross, N., & Telling, J. (2020). GERALDINE (Google Earth Engine supRaglAcial Debris INput dEtector): a new tool for identifying and monitoring supraglacial landslide inputs. *Earth Surface Dynamics*, 8(4), 1053-1065. <https://doi.org/10.5194/esurf-8-1053-2020>
- Sun, X., Cao, B., Pan, B., Li, K., Zhao, X., & Guan, W. (2022). Identification of hazardous glacial lakes in the Yarlung Zangbo River Basin based on lakes changes determined using Google Earth Engine. *Frontiers in Earth Science*, 10, 825482. <https://doi.org/10.3389/feart.2022.825482>
- Tamiminia, H., Salehi, B., Mahdianpari, M., Quackenbush, L., Adeli, S., & Brisco, B. (2020). Google Earth Engine for geo-big data applications: A meta-analysis and systematic review. *ISPRS journal of photogrammetry and remote sensing*, 164, 152-170. <https://doi.org/10.1016/j.isprsjprs.2020.04.001>
- Truffer, M., & Motyka, R. J. (2016). Where glaciers meet water: Subaqueous melt and its relevance to glaciers in various settings. *Reviews of Geophysics*, 54(1), 220-239. <https://doi.org/10.1002/2015RG000494>
- Turpo Cayo, E. Y., Borja, M. O., Espinoza-Villar, R., Moreno, N., Camargo, R., Almeida, C., ... & Souza Jr, C. M. (2022). Mapping three decades of changes in the tropical Andean glaciers using landsat data processed in the Earth engine. *Remote Sensing*, 14(9), 1974. <https://doi.org/10.3390/rs14091974>
- USGS. (n.d). Landsat 9. Retrieved March 26, 2024, from <https://www.usgs.gov/landsat-missions/landsat-9>
- Van Ackere, S., Glas, H., Beullens, J., Deruyter, G., De Wulf, A., & De Maeyer, P. (2016). Development of a 3D dynamic flood WEB GIS visualisation tool. *Flood Risk Management and Response*, 106. <https://doi.org/10.2495/SAFE-V6-N3-560-569>

- Wang, S., Li, W., & Wang, F. (2017, June). Web-scale multidimensional visualization of big spatial data to support earth sciences—A case study with visualizing climate simulation data. In *Informatics* (Vol. 4, No. 3, p. 17). MDPI.
<https://doi.org/10.3390/informatics4030017>
- Windnagel, A., Hock, R., Maussion, F., Paul, F., Rastner, P., Raup, B., & Zemp, M. (2023). Which glaciers are the largest in the world?. *Journal of glaciology*, 69(274), 301-310. <https://doi.org/10.1017/jog.2022.61>
- Xu, F., Li, Z., Zhang, S., Huang, N., Quan, Z., Zhang, W., ... & Prishchepov, A. V. (2020). Mapping winter wheat with combinations of temporally aggregated Sentinel-2 and Landsat-8 data in Shandong Province, China. *Remote Sensing*, 12(12), 2065. <https://doi.org/10.3390/rs12122065>
- Yu, Aijie & Shi, HL & Wang, Yifan & Yang, Jin & Gao, Chunchun & Lu, Yang. (2023). A Bibliometric and Visualized Analysis of Remote Sensing Methods for Glacier Mass Balance Research. *Remote Sensing*. 15. 1425.
<https://doi.org/10.3390/rs15051425>
- Zemp, M., Huss, M., Thibert, E., Eckert, N., McNabb, R., Huber, J., ... & Cogley, J. G. (2019). Global glacier mass changes and their contributions to sea-level rise from 1961 to 2016. *Nature*, 568(7752), 382-386.
<https://doi.org/10.1038/s41586-019-1071-0>
- Zhang, C., Di, L., Yang, Z., Lin, L., & Hao, P. (2020). AgKit4EE: A toolkit for agricultural land use modeling of the conterminous United States based on Google Earth Engine. *Environmental Modelling & Software*, 129, 104694.
<https://doi.org/10.1016/j.envsoft.2020.104694>
- Zhang, J., Jia, L., Menenti, M., Zhou, J., & Ren, S. (2021). Glacier area and snow cover changes in the range system surrounding tarim from 2000 to 2020 using google earth engine. *Remote Sensing*, 13(24), 5117.
<https://doi.org/10.3390/rs13245117>
- Zhang, Q., Hu, D., & Lin, Q. (2021). Design of High-precision Island WebGIS Based on Cesium. In *Proceedings of the 5th International Conference on Computer Science and Application Engineering* (pp. 1-7).
<https://doi.org/10.1145/3487075.3487146>

ATTACHMENTS

Free attachments

Attachment 1 Poster

Attachment 2 Website

APPENDIX

Appendix A: Consolidated table with the glacier area changes for all studied glaciers.

Appendix B: Consolidated table of LST rate changes for all studied glaciers.

Appendix C: Consolidated table of air temperature rate changes for all studied glaciers.

Appendix A: Consolidated table with the glacier area changes for all studied glaciers.

GLACIER	RGI 7.0 AREA (Km ²)	YEAR	2022-2023 AREA (Km ²)	AREA LOSE (Km ²)	RATE OF CHANGE Km ² /summer	\bar{y}	R ²	RRMSD	ICEFIELD	HEIGHT (MEDIAN) m
AGASSIZ-BOLADOS	50.76	2005	50.1	-0.66	-0.0447	50.17	0.6893	0.08%	SPI	1723.07
AMALIA	162.29	2001	159.05	-3.24	0.3125	158.3	0.0705	1.01%	SPI	1314.58
AMEGHINO	67.74	2001	63.25	-4.49	-0.2683	63.4	0.1184	1.63%	SPI	1063.92
ANTE-CUMBRE BERTRAND SUR	12	2005	11.43	-0.57	-0.0344	11.29	0.0276	2.56%	SPI	1501.83
ARCO	20.48	2001	19.14	-1.34	-0.116	19.31	0.7788	0.45%	NPI	1475.21
ASIA	115.66	2001	114.86	-0.8	-0.0438	114.32	0.0078	0.61%	SPI	1133.64
BALMACEDA	59.4	2001	56.52	-2.88	-0.2778	57.1	0.2334	1.25%	SPI	898.8
BAYO	12.92	2000	6.93	-5.99	-0.1151	7.26	0.4	2.75%	NPI	697.44
BENITO	164.06	2001	155.75	-8.31	-0.0849	155.31	0.0148	0.63%	NPI	916.15
BERNARDO	565.14	2001	551.52	-13.62	0.8909	547.35	0.063	0.89%	SPI	1483.15
BRAVO	98.12	2001	93.16	-4.96	-0.2417	93.58	0.5464	0.33%	NPI	1663.99
CACHET	37.62	2001	36.42	-1.2	-0.0648	36.55	0.7506	0.15%	NPI	1513.41
CAGLIERO (SUR)	11.48	2005	10.98	-0.5	-0.0112	10.93	0.0746	0.51%	SPI	1930.81
CALVO	99.06	2001	98.99	-0.07	0.3884	98.41	0.6405	0.42%	SPI	1812.72
CERRO DE MAYO NORTE	21.83	2005	21.464	-0.366	-0.026	21.48	0.3841	0.22%	SPI	1491.27
CHICO	311.79	2001	303.442	-8.348	0.2443	301.34	0.0303	0.65%	SPI	1518.74
COLONIA	282.07	2001	258.854	-23.216	-0.7292	260	0.7385	0.24%	NPI	1483.84
EUROPA	433.7	2001	433.399	-0.301	-0.0332	433.33	0.1318	0.03%	SPI	1461.55
EXPLORADORES	83.53	2000	69.071	-14.459	0.2632	68.59	0.2263	1%	NPI	1683.56
FIERO	36.89	2000	32.118	-4.772	0.0072	32.27	0.0003	1.71%	NPI	1692.06
FRAENKEL	30.67	2001	28.713	-1.957	0.0276	28.62	0.0656	0.52%	NPI	1292.74
FRIAS Y GRANDE	47.42	2005	42.9	-4.52	-0.4194	44.18	0.4566	1.44%	SPI	1000.48
GREY	228.48	2001	223.304	-5.176	-0.4762	224.6	0.6518	0.22%	SPI	1279.64
GUALAS	116.47	2000	106.183	-10.287	-0.2484	106.65	0.2818	0.53%	NPI	1183.24

GUILARDI	138.21	2001	135.931	-2.279	-0.1844	136.1	0.3879	0.24%	SPI	1035.37
HPN1	155.14	2001	141.494	-13.646	-0.6869	141.41	0.1372	1.72%	NPI	812.45
HPN4	62.5	2001	58.718	-3.782	-0.2096	59.44	0.3278	0.71%	NPI	1265.39
HPS10	55.59	2001	53.844	-1.746	-0.1379	54.09	0.5173	0.35%	SPI	1342.5
HPS12	168	2001	156.028	-11.972	-0.6889	155.45	0.1142	1.75%	SPI	1459.29
HPS13	219.37	2001	219.131	-0.239	-0.0222	218.91	0.0248	0.09%	SPI	1775.61
HPS17	60.01	2001	59.762	-0.248	-0.0523	59.64	0.114	0.35%	SPI	1351.12
HPS18	37.49	2001	37.079	-0.411	-0.0429	37.08	0.2357	0.29%	SPI	1472.4
HPS19	172.6	2001	172.457	-0.143	-0.0088	172.42	0.0197	0.06%	SPI	1569.21
HPS20	12.78	2001	12.376	-0.404	-0.028	12.36	0.282	0.51%	SPI	1180.22
HPS22	21.38	2001	21.15	-0.23	-0.021	21.13	0.2517	0.24%	SPI	1133.94
HPS24	41.3	2001	39.009	-2.291	-0.2569	38.96	0.2911	1.45%	SPI	972.84
HPS25	11.36	2001	11.045	-0.315	-0.0466	11.08	0.5251	0.57%	SPI	973.92
HPS27	31.84	2001	31.71	-0.13	-0.0233	31.62	0.0526	0.44%	SPI	1677.11
HPS28	60.11	2001	56.422	-3.688	-0.175	56.58	0.5076	0.43%	SPI	1614.03
HPS29	82.05	2001	81.913	-0.137	-0.0107	81.83	0.0303	0.11%	SPI	1539.27
HPS30	19.68	2001	19.193	-0.487	-0.08	19.18	0.3757	0.76%	SPI	1113.5
HPS31	155.33	2001	154.789	-0.541	0.0072	154.6	0.002	0.15%	SPI	1469.65
HPS33	19.12	2001	19.023	-0.097	-0.0279	19.04	0.6085	0.17%	SPI	1157.93
HPS34	153.78	2001	153.511	-0.269	-0.0535	153.45	0.2486	0.09%	SPI	1644.35
HPS35	27.29	2001	26.879	-0.411	-0.0391	26.91	0.2635	0.34%	SPI	949.93
HPS38	69.81	2001	61.082	-8.728	-0.9506	61.78	0.6415	1.63%	SPI	970
HPS39	49.85	2001	44.505	-5.345	-0.3934	44.33	0.3089	1.88%	SPI	858.13
HPS41	68.13	2001	64.873	-3.257	-0.433	65.43	0.5198	0.90%	SPI	1221.71
HPS9	51.07	2001	47.848	-3.222	-0.0702	48.48	0.0264	1.24%	SPI	1541.63
JORGE MONTT	463.42	2001	440.224	-23.196	-0.4271	434.34	0.0091	1.45%	SPI	1366.44
LEONES	63.42	2000	59.628	-3.792	-0.2293	60.11	0.3597	0.72%	NPI	1742.72
LUCIA	160.33	2001	151.584	-8.746	-0.2852	151.72	0.1702	0.59%	SPI	1392.03

MARCONI	16.67	2005	14.108	-2.562	-0.1846	14.29	0.5831	1.54%	SPI	1353.24
MELLIZO SUR	36.85	2001	36.14	-0.71	-0.0514	36.26	0.2223	0.38%	SPI	2038.55
NEF	131.3	2001	118.432	-12.868	-0.2668	118.77	0.3594	0.42%	NPI	1452.22
OFHIDRO	76.51	2001	74.408	-2.102	0.274	73.29	0.186	1.11%	SPI	1196.12
O'HIGGINS	780.49	2001	767.112	-13.378	-1.0898	767.61	0.5549	0.18%	SPI	1402.56
ONELLI	41.8	2005	37.615	-4.185	-0.2701	37.94	0.6011	0.82%	SPI	1519.71
ORIENTAL	70.22	2001	67.838	-2.382	-0.1179	67.94	0.3117	0.37%	SPI	1630.3
PARED NORTE	77.13	2001	66.519	-10.611	-0.339	67.03	0.3624	0.95%	NPI	1033.29
PARED SUR	31.52	2001	21.837	-9.683	-0.451	22.11	0.4343	3.30%	NPI	848.38
PASCUA	78.6	2001	73.202	-5.398	-0.353	73.2	0.2381	1.22%	SPI	1059.34
PENGUIN	457.98	2001	457.728	-0.252	-0.0006	457.62	0.00008	0.02%	SPI	1714.16
PINGO	59.54	2001	58.977	-0.563	-0.0495	59.08	0.2326	0.22%	SPI	1300.88
PIO XI	1233.08	2001	1223.32	-9.76	1.9495	1220.65	0.1734	0.49%	SPI	1294.38
PISCIS	12.18	2001	11.122	-1.058	-0.075	11.21	0.77	0.51%	NPI	1208.23
REICHER	66.79	2000	60.505	-6.285	0.0289	60.36	0.0015	1.72%	NPI	1482.35
SAN QUINTIN	815.29	2001	802.856	-12.434	-0.5552	803.98	0.5851	0.08%	NPI	1300.28
SAN RAFAEL	684.55	2000	676.397	-8.153	-0.1774	676.46	0.0908	0.12%	NPI	1327.67
SNOWY	18.22	2001	16.984	-1.236	0.006	16.84	0.0003	3.15%	SPI	975.33
SOLER	49.28	2001	44.482	-4.798	0.033	44.34	0.0437	0.49%	NPI	1732.78
STEFFEN	547.59	2001	527.533	-20.057	-0.7419	527.23	0.157	0.46%	NPI	1249.04
STRINDBERG	16.33	2001	14.874	-1.456	-0.0411	14.96	0.4693	0.41%	NPI	1113.52
TEMPANO	433.91	2001	410.92	-22.99	1.8988	413.43	0.0805	2.19%	SPI	1239.65
TORRE ADELA GRANDE	24.22	2005	19.82	-4.4	-0.0715	19.81	0.2541	0.87%	SPI	1490.36
TUNEL	17	2005	15.911	-1.089	-0.0438	15.91	0.4579	0.42%	SPI	1518.59
TYNDALL	319.6	2001	309.5	-10.1	-0.7631	311.14	0.3918	0.43%	SPI	1018.81
U2	15.02	2001	13.874	-1.146	-0.0649	13.92	0.3941	0.82%	NPI	1408.82
U3	17.6	2001	16.957	-0.643	-0.0733	17.03	0.5721	0.53%	NPI	1419.29
U-4	11.89	2001	9.725	-2.165	-0.3323	10.16	0.8865	1.66%	NPI	1408.97
U6	13.32	2000	10.476	-2.844	-0.0251	10.55	0.0544	1.40%	NPI	1433.71
UPSALA	778.97	2005	741.83	-37.14	-0.2795	733.74	0.0037	0.89%	SPI	1299.46
VIEDMA	896.36	2001	864.112	-32.248	-1.144	863.83	0.2458	0.33%	SPI	1323.83

Appendix B: Consolidated table of LST rate changes for all studied glaciers.

GLACIER	RATE OF CHANGE °C/summer	\bar{y}	R²	RMSD
AGASSIZ-BOLADOS	0.7562	-1.45	0.8038	0.53
AMALIA	0.3174	-1.59	0.1763	0.97
AMEGHINO	0.8491	-0.62	0.79	0.62
ANTE-CUMBRE BERTRAND SUR	0.684	-0.36	0.6629	0.69
ARCO	-0.0357	-0.41	0.0236	0.33
ASIA	0.3244	-0.91	0.7957	0.23
BALMACEDA	-1.6938	-0.99	0.8336	1.07
BAYO	0.7417	0.61	0.4653	1.12
BENTO	-0.1452	-0.27	0.1817	0.44
BERNARDO	0.6754	-1.4	0.6466	0.71
BRAVO	0.227	-1.22	0.2792	0.52
CACHET	-0.2268	-0.53	0.1883	0.67
CAGLIERO (SUR)	0.2997	-1.1	0.1486	1.01
CALVO	-1.0306	-3.53	0.75	0.83
CERRO DE MAYO NORTE	0.6876	-1.24	0.5078	0.96
CHICO	0.051	-0.89	0.0306	0.41
COLONIA	-0.0753	-0.22	0.1015	0.32
EUROPA	0.0619	-1.55	0.0497	0.38
EXPLORADORES	0.5231	-0.8	0.2235	1.38
FIERO	-0.2304	-0.81	0.0568	1.33
FRAENKEL	-0.3266	-1.54	0.1751	1
FRIAS Y GRANDE	-0.1115	0.14	0.0863	0.51
GREY	-0.6684	-1.74	0.3673	1.24
GUALAS	-0.4421	-0.05	0.7491	0.36
GUILARDI	0.7559	-1.2	0.4818	1.11
HPN1	-0.1603	0.06	0.283	0.36
HPN4	0.1077	-0.41	0.0392	0.75
HPS10	0.1823	-0.49	0.2273	0.48
HPS12	0.1753	-0.77	0.1924	0.51
HPS13	-0.4295	-2.59	0.3298	0.87
HPS17	0.0261	-0.46	0.0025	0.74
HPS18	0.1266	-1.51	0.0517	0.77
HPS19	-0.0506	-1.52	0.0106	0.69
HPS20	0.1005	-0.24	0.0561	0.58
HPS22	1.4173	-2.26	0.5177	1.93
HPS24	0.4633	-0.62	0.4287	0.76
HPS25	0.2739	-0.49	0.3251	0.56
HPS27	0.8247	-1.76	0.8874	0.42
HPS28	1.7073	-2.86	0.7157	1.52
HPS29	0.6365	-2.17	0.567	0.79
HPS30	0.5008	-0.81	0.7747	0.38

HPS31	0.1124	-1.77	0.0426	0.745
HPS33	0.7317	-0.9	0.0426	1.07
HPS34	0.469	-2.22	0.7441	0.39
HPS35	0.2874	-0.49	0.3622	0.54
HPS38	0.2318	-0.79	0.3622	0.86
HPS39	-0.7203	0.11	0.6048	0.82
HPS41	-1.8255	-1.36	0.9275	0.72
HPS9	-0.0987	-1.52	0.0174	1.05
JORGE MONTT	0.1213	-0.53	0.2677	0.28
LEONES	-0.3691	-0.9	0.3712	0.68
LUCIA	0.0022	-0.53	0.0003	0.2
MARCONI	-0.4999	-0.25	0.2276	1.3
MELLIZO SUR	0.0824	-2.29	0.0096	1.18
NEF	-0.2738	-0.48	0.2649	0.65
OFHIDRO	0.4474	-0.88	0.4923	0.64
O'HIGGINS	0.0261	-1.02	0.0051	0.51
ONELLI	0.6273	-1.27	0.6204	0.69
ORIENTAL	0.126	-0.33	0.2925	0.28
PARED NORTE	0.1029	0.1	0.2062	0.29
PARED SUR	0.1467	0.4	0.4143	0.25
PASCUA	0.1801	0.05	0.5433	0.23
PENGUIN	-0.2843	-2.38	0.225	0.75
PINGO	-0.1744	-1.73	0.0242	1.56
PIO XI	-0.2508	-0.97	0.143	0.87
PISCIS	0.2195	0.36	0.4224	0.36
REICHER	-0.6086	-0.62	0.7289	0.45
SAN QUINTIN	-0.3328	-0.55	0.4222	0.55
SAN RAFAEL	-0.0744	-0.23	0.069	0.39
SNOWY	-1.39	-0.51	0.4526	2.17
SOLER	-0.1629	-1.39	0.0557	0.95
STEFFEN	-0.1761	-0.21	0.2298	0.46
STRINDBERG	-0.3406	-0.77	0.225	0.89
TEMPANO	-0.0305	-1.03	0.0029	0.81
TORRE ADELA GRANDE	0.2179	-0.07	0.0813	1.04
TUNEL	0.2621	-0.3	0.2322	0.67
TYNDALL	-0.299	-1.02	0.0851	1.39
U2	0.6058	-0.87	0.3942	1.06
U3	0.3328	-0.74	0.3385	0.66
U-4	0.2251	-0.18	0.4593	0.35
U6	0.1235	-0.43	0.0239	1.12
UPSALA	0.2258	-0.77	0.4771	0.33
VIEDMA	0.1995	-0.82	0.5804	0.24

Appendix C: Consolidated table of air temperature rate changes for all studied glaciers.

GLACIER	RATE OF CHANGE °C/Summer	y	R²	RMSD
AGASSIZ-BOLADOS	0.0269	-1.57	0.025	0.24
AMALIA	0.0481	1.8	0.0488	0.3
AMEGHINO	0.1699	0.83	0.4164	0.28
ANTE-CUMBRE BERTRAND SUR	0.0178	-2.08	0.0168	0.19
ARCO	0.1369	2.71	0.2411	0.34
ASIA	0.0348	3.69	0.0239	0.32
BALMACEDA	-0.0088	4.72	0.0013	0.34
BAYO	0.128	1.59	0.327	0.26
BENITO	0.1319	2.67	0.3677	0.25
BERNARDO	0.1435	0.52	0.378	0.26
BRAVO	0.1064	0.02	0.2787	0.24
CACHET	0.2115	1.01	0.4871	0.31
CAGLIERO (SUR)	0.0739	1.69	0.107	0.3
CALVO	0.0719	-0.018	0.0765	0.35
CERRO DE MAYO NORTE	0.1276	1.33	0.3872	0.23
CHICO	0.1472	-0.58	0.3654	0.27
COLONIA	0.1467	1.73	0.3239	0.3
EUROPA	0.0551	0.88	0.085	0.26
EXPLORADORES	0.0827	1.91	0.1755	0.25
FIERO	0.128	1.59	0.327	0.26
FRAENKEL	0.1652	3.48	0.3085	0.35
FRIAS Y GRANDE	0.0728	1.77	0.0769	0.36
GREY	0.0904	0.52	0.1172	0.35
GUALAS	0.138	2.6	0.3833	0.25
GUILARDI	0.0926	3.2	0.2112	0.25
HPN1	0.1702	5.63	0.2971	0.37
HPN4	0.1707	5.75	0.1815	0.51
HPS10	0.0364	2.25	0.056	0.21
HPS12	0.0691	0.98	0.1601	0.22
HPS13	0.0882	-0.75	0.2047	0.25
HPS17	0.0417	1.48	0.0384	0.3
HPS18	0.0539	1.42	0.069	0.28
HPS19	0.0355	-1.11	0.04	0.25
HPS20	0.0555	2.76	0.0625	0.3
HPS22	0.0713	2.99	0.167	0.23
HPS24	0.1405	3.88	0.325	0.29
HPS25	0.0786	3	0.1612	0.25
HPS27	0.0549	2.62	0.0951	0.24
HPS28	0.1897	2.37	0.4415	0.3
HPS29	0.182	1.85	0.3425	0.36
HPS30	0.2397	4.71	0.4033	0.41
HPS31	0.0952	1.49	0.1564	0.31

HPS33	0.0639	0.5	0.0677	0.34
HPS34	0.0639	0.5	0.0677	0.34
HPS35	0.0827	3.1	0.1426	0.29
HPS38	-0.0424	3.44	0.0382	0.3
HPS39	-0.0752	4.37	0.0916	0.34
HPS41	0.0122	3.94	0.0032	0.31
HPS9	0.0334	2.19	0.0576	0.19
JORGE MONTT	0.1221	0.59	0.2894	0.27
LEONES	0.1509	1.76	0.4047	0.26
LUCIA	0.112	0.17	0.2902	0.25
MARCONI	0.0871	0.063	0.1679	0.27
MELLIZO SUR	0.1555	0.63	0.4613	0.24
NEF	0.1652	2.09	0.4022	0.29
OFHIDRO	0.0886	2.68	0.1389	0.31
O'HIGGINS	0.0457	-0.18	0.0793	0.22
ONELLI	0.0418	-0.77	0.0641	0.23
ORIENTAL	0.1555	0.63	0.4613	0.24
PARED NORTE	0.1347	3.67	0.1825	0.4
PARED SUR	0.2078	4.71	0.2773	0.47
PASCUA	0.1279	0.25	0.3645	0.24
PENGUIN	0.0204	-1.06	0.0138	0.23
PINGO	0.0714	1.55	0.0976	0.31
PIO XI	0.0571	0.93	0.1154	0.22
PISCIS	0.1731	4.6055	0.2182	0.46
REICHER	0.117	1.59	0.3445	0.23
SAN QUINTIN	0.1783	2.17	0.4506	0.28
SAN RAFAEL	0.1645	2.26	0.4425	0.26
SNOWY	-0.0088	4.72	0.0013	0.34
SOLER	0.1401	2.09	0.3336	0.28
STEFFEN	0.1262	3.17	0.2878	0.28
STRINDBERG	0.1652	3.48	0.3085	0.35
TEMPANO	0.0635	1.8	0.1564	0.21
TORRE ADELA GRANDE	0.0654	2.49	0.0793	0.32
TUNEL	0.0654	2.49	0.0793	0.32
TYNDALL	0.0407	2.3	0.0467	0.26
U2	0.1707	5.75	0.1815	0.51
U3	0.1731	5.13	0.2182	0.46
U-4	0.1347	3.67	0.1825	0.4
U6	0.128	1.59	0.327	0.26
UPSALA	0.1075	-0.2	0.2811	0.24
VIEDMA	0.0906	-0.43	0.1776	0.28